Nanoparticle Mediated Heating for Non-invasive Thermal Therapies

A thesis submitted to the University of London for partial fulfilment of the requirements for the degree of Doctor of Philosophy

By
Hui-Jiuan Chen

Supervisors: Prof. Dongsheng Wen
Prof. Gleb Sukhorukov

School of Engineering and Materials Science
Queen Mary University of London
June 2013

Declaration

I confirm and declare that the dissertation "Nanoparticle mediated heating for non-invasive thermal therapy" is my own work and all the sources I have utilized have been indicated by completed references.

Signature:

Acknowledgements

I would like to thank my supervisor, Prof. Dongsheng Wen, for not only supervising the project but also his professional commitments. His patience, professional help and stimulating suggestions help me in all the time of this project.

Special thanks to my cooperation partners Dr. Xiaoming Liu and Prof. Xiaodong Chen. School of Electronic Engineering and Computer Science, Queen Mary University of London. Dr. Xiaoming Liu was involved in the experiments of DC voltages induced effects in Chapter 3-6 and the heating effect of EM field at 2.45 GHz and 13.56 MHz as well as the dielectric measurement in Chapter 4. He has made efforts and contributions in the 13.56 MHz equipment setup and simulation analysis.

Many thanks to my second supervisor Prof. Gleb Sukhorukov, Dr. Anton Pavlov and Ms. Qiangyin Yi provide their knowledge and technology in microcapsule fabrication and B50 cell uptake, biocompatibility of GNPs in this project. Mr. Cenghao Chen provides a lot of assistance in Fruit flies uptake, biocompatibility of GNPs in this project.

Many thanks to Dr. Zofia Luklinska in the Nano vision center for her patience and time to help me identify nanoparticles and teach me what are TEM and SEM and how do they work.

Many thanks to Prof. William Gillin and Mr. Huanqing Ye from *School of Physics, QMUL* for providing me laser equipment and professional knowledge. Also, thanks to

Dr. Stuart J. Corr and Prof. Steven A. Curley from *MD Anderson Cancer Centre, USA* for providingthe Kanzius RF system and measurement assistance.

I am greatly appreciative to my family for supporting and encouraging me to study. Without them my effort would have been worth nothing. Many thanks to my love, Mr. Zhe Li, for his encourage, personal support and great patience at all times.

Abstract

Nanomaterials have unique physics and chemistry properties compared with their bulk counterparts and have been widely studied in different fields ranging from energy to biomedicines. This thesis investigates controlled synthesis of gold nanomaterials, the heating and interactions of gold nanomaterials with external electromagnetic and ultrasonic fields, and their potential applications in non-invasive heat-related biomedicines.

Gold nanomaterials have been synthesised by the citrate reduction method with the aid of ultrasonification. Through ultrasonification, the size of obtained spherical GNPs can be controlled between 10nm and 15nm, and the prepared nanoplates can be controlled between 50 nm to 150 nm. Purification process has been performed through membrane dialysis, in order to obtain pure nanoparticles for investigating the heating behavior of nanoparticle dispersions under EM/ultrasound field and elucidating the impurity effect. Moreover, the purified gold nanoparticles have been characterized by various means, such as FTIR, atomic absorption spectrometer, zetasizer, SEM, TEM and UV-Vis absorption for the purpose of fully understand the properties of gold nanoparticle in terms of purity, concentration, size, morphology and optical properties.

The bulk heating effects of low-concentration GNPs have been investigated by using ultrasonic field, electromagnetic (EM) field, and laser irradiation. The results have shown that significant bulk temperature increase can be achieved for the low-concentration gold nanoparticle dispersions under ultrasonic field, the EM field at 200 kHz and 400 kHz, and laser irradiation. Comparatively, the purified GNPs did not show significant heating effect under the EM fields of 13.56 MHz and 2.45 GHz.

Different mechanisms are thereby discussed to explain the heating effects. While some can be explained by established theories, such as the ultrasonic and laser heating, it is still unclear about the heating effect under low frequency EM field. A few possible reasons could be attributed to the changes of the dielectric properties and the electrophoresis effect.

In addition, GNP incorporated microcapsules have been fabricated through the layer-by-layer technology, and laser treatments of the microcapsules embedded with different shapes of gold particles have been studied. The results have shown that matching between the laser wavelength and the absorption band of gold nanoparticles, which can be shifted by controlling the morphology of nanoparticles, is a prerequisite to achieve the maximum heating effect to deform the microcapsules and hence to present the microcapsules for biomedical uses.

In vitro (B50 cell) and *in vivo* (fruit fly) studies of the biocompatibilities of our synthesised GNPs have been exanimated. The results demonstrated that the GNPs have high biocompatibility for B50 cells and fruit flies. GNPs assisted laser treatment of B50 cells has shown faster thermal damage to the cells in contrast to the cells without addition of GNPs.

Keywords: nanomaterial, gold nanoparticle, capsules, hyperthermia, ablation, electromagnetic, ultraosound, surface Plasmon resonance, biocompatibility

Table of Contents

Abbreviations

CW	Continuous wave
CLSM	Confocal laser scanning microscopy
DC	Direct current
DI-water	De-ionised water
DNA	Deoxyribonucleic acid
EM waves	Electromagnetic waves
FTIR	Fourier Transform Infrared
GNPs	Gold nanoparticles
IR	Infrared
LBL	Layer by layer
MRI	Magnetic resonant imaging
PEG	Polyethylene glycol
PTT	Photothermal therapy
RF	Radio frequency
SAR	Specific absorption rate
SPR	Surface plasmon resonance
SEM	Scanning electron microscopy
SWCNs	Single-walled carbon nanotubes
TEM	Transmission electron microscopy
UV	Ultra-violet
VNA	Vector Network Analyser

Symbols and Units

M	Magnetisation	A/m
H	Magnetic field strength	A/m
μ	Absolute permeability	H/m
μ_r	Relative permeability	
μ_0	Permeability of free space	H/m
P	Electric polarisation	C/m^2
E	Electric field strength	V/m
ε	Absolute permittivity	F/m
ε_r	Relative permittivity	
ε_0	Permittivity of free space	F/m
I	Current	A
$\sigma(\omega)$	Frequency dependent effective conductivity	S/m
σ_0	DC conductivity (Ionic conductivity)	S/m
C_w	Specific heat capacitor of water	J/K/kg
T	Temperature	˚C
t	Time	s
Z	Impedance	Ω
ρ	Mass density	kg/m^3
λ	Wavelength	m
f	Frequency	Hz
SAR	Specific absorption rate	W/kg

Chapter 1 Background

Nanotechnology can be defined as the application of science and technology manufactured on the manipulation of matter on a molecular and atomic scale that broadly contains physics, chemistry, biological and material science. In biomedical field, it offers a distinctive approach and extensive technology against cancer throughout diagnosis, prediction, prevention, personalized treatment and new medicine to overcome the problems caused by traditional cancer therapies (Daniel and Astruc, 2004).

Nanomedical tools have been investigated to improve microsurgery instruments that are more basically miniaturized surgery devices to be performed under remote control. Nanomedical tools are different from microsurgery devices in two primary respects which are being self-directing tools that are able to operate within the body without any remote control by human and holding high biocompatibility in the long term, thus allowing their semipermanent residence *in vivo* (Haberzettl, 2002). Furthermore, there is a vitally important innovation in traditional pharmaceuticals. Nanopharmaceuticals are great evolution in pharmaceutical industry; they take advantage of nanochemistry to replace the gap between medical and surgical techniques to healing. Nowadays, drugs utilize physiological pathways to distribute chemicals to related tissues; at the same time as surgery straightly deal with organs and bodily parts that necessitate to be repaired. Actually, the premature stages of nanodrug evolution just use the increased reactivity and solubility of nanoparticles to enable speed up infusion of drugs in vivo, at present most researches in nanodrugs are focus on self-controlled drug dispensation which is nanosized formulations allow to be adapted for dispensation within the body because the size of nanosized drug is small enough to pass physiological barriers to deliver the drug into the targets. By changing the surface structure of the nanoparticle

could make the drug delivery more efficacious because this is able to inhibit macrophage detection or control particle self-aggregation (Emerich and Thanos, 2006).

Biomaterials and Tissue engineering can design nanostructure medical implants and scaffolds which improve biocompatibility and adhesion (Shi et al., 2010). Further researches for developing nanodiagnostic instruments are already in animal test stage which the prospect of permanently inserting nanosized apparatus into animals that do not activate the immune response. Nanodiagnostic instruments are going to enable continuous monitoring of the health conditions and will offer early detection of pathological conditions as well as could be used for preventing spread of contagious illnesses (Narducci, 2007). These nanodiagnostic tools could offer clinicians with a more complete quick test of blood chemistries, hormones, and growth factors in normal and diseases conditions, but may also permit them to trace the efficiency of putative therapeutics (Koehne et al., 2004).

Nanomaterials have been highlighted as promising candidates to improve medical imaging to make a quicker, less or non-invasive and accurate method to diagnose cancer diseases and help surgeons locate tumors. Magnetic nanoparticles such as Fe_3O_4 nanoparticles have been utilized as contrast enhancement agents in magnetic resonance imaging (MRI) to detect tumours (Jun et al., 2005). Carbon nanotubes are also used as contrast agents for microwave detection and treatment of breast cancer (Mashal et al., 2010). Biofunctional magnetic nanoparticles are applied in MRI as contrast agents. MRI exhibits that the conjugated nanoparticles can effectively target cancer cells *in vitro* and *in vivo*, suggesting that they potentially can be used as contrast agents for magnetic resonance imaging of pancreas cancer (Huang et al., 2009).

Hyperthermia including laser, ultrasound, microwave, radiofrequency ablation is currently used in clinical practice to treat solid tumours by delivering thermal energy. It is flexible, low cost and minimal invasive treatment compared with surgery. However, the drawbacks of thermal therapies are skin burn, thermal damage of adjacent healthy tissue and limited therapic area. Recent research in nanomaterials has provided a potential non-invasive way for hyperthermia to eliminate exist limitation of current hyperthermia. Functioned nanoparticles targeted specific site allows non-invasive treatment more efficient and faster because nanoparticles are able to enhance and convert absorbed energy into heat promptly. For example, Cardinal et al. 2008 and Gannon et al. 2008 have utilized gold nanoparticles as heat receptors to improve current RFA. The concept of this new technique is adding GNPs to human cancer cells and then these cancer cells, which contain GNPs, are exposed to a non-invasive radiofrequency field to produce thermal injury in vitro or in vivo (Cardinal et al., 2008, Gannon et al., 2008).

The hypothesis and the scope

Nanoparticles have been used in hyperthermia in recent years. However, the limitations still exist in these researches and most of the mechanisms remain unclear, and most applications are still in the preliminary or preclinical stage. This project will try to develop a method for controlled synthesis of nanoparticles with different morphology and size, and study the interactions between these nanoparticles with a wide frequency range of electromagnetic/ultrasound field. We expect that different gold nanoparticles will have different heating response under a varying frequency of electromagnetic/ultrasound field, and the heating effect can be optimised to be useful in biomedical applications, such as hyperthermia.

Chapter 2 will review the state-of-art of the GNPs synthesis, and hyperthermia with nanoparticles. Chapter 3 will present the design and synthesis of nanomaterials with tailored shape and size, the improved synthesis method with the assist of ultrasonification, and the unique structure-dependent optical properties. Chapter 4 will introduce the heating experiment of nanomaterials under ultrasound field, and electromagnetic field at 200 kHz, 400 kHz, 13.56 MHz, 2.45 GHz and the visible spectrum. This heating study is to investigate the heating behaviour of GNPs under the electromagnetic and ultrasound field and therefore increase the temperature of the bulk GNP dispersions. Chapter 5 will show *in vitro* and *in vivo* of the biocompatibility, cellular uptake of GNPs and GNP mediated laser treatment *in vitro*. We will study the biocompatibility and cytotoxicity of GNPs with the B50 cells and Drosophila to verify our purified GNPs would not cause any adverse effects to the survival of B50 cells and drosophila. Furthermore, the GNP-mediated photothermal treatment of B50 cells will be studied to understand the effect of GNPs mediated photothermal treatment in vitro.

Chapter 2 State-of-art review

2.1 Synthesis, characterization and purification of GNPs

Currently a wide range of vapor, liquid and mechanical routes are available for synthesizing nanoparticles. Both mechanical route, such as milling and grinding, and vapor-phase route through combustion, pyrolysis, plasmas, laser ablation, laser pyrolysis or chemical vapor deposition are energy intensive. For GNPs, the liquid route synthesis is preferred, which typically involves chemical reactions of a few reagents with one desired product. Subsequent separation and purification can lead to designed products.

The most commonly used method of synthesising GNPs is the chemical reduction of a gold(III) precursor compound in the existence of a capping agent, i.e., a compound to bind the nanoparticle surface restricting its growth within the nanometer range and stabilizing the colloid in the solvent. Control over the shape and size of the GNPs is typically accomplished through the careful selection of the reducing agent, reaction time, temperature, and capping agent. Capping agents with high affinity can be used for GNP formation, such as thiol capping agents. This enables the synthesis of GNPs with good size and dispersion; it is however normally only soluble in organic phase, and requires an extra step of extraction of the nanoparticles into water. Furthermore, swapping for strongly binding capping agents is normally burdensome that makes GNPs less capable for biological applications (Baptista et al., 2008). The citrate reduction and the Brust-Schiffrin method are the common techniques to synthesise GNPs. Using the citrate reduction method can produce large GNPs in the size of 10-150 nm in diameter. The Brust-Schiffrin method is facile to synthesize smaller particles in the range of 1.5 ~ 5.2 nm in diameter.

The most conventionally utilized technique for the synthesis of spherical GNPs for biological application is the citrate reduction method (Frens, 1973). The utilization of citrate as a capping agent is very facile because it is easy to be used for the post-synthesis treatment and can be simply superseded by other capping agents such as thiol capping agents. This allows a suitable functionality to bind the biological substance to be analyzed. The citrate reduction method can control the particle size within the range from 10 nm to 150 nm, and current improvements have enabled better size distribution of the particles (Kimling et al., 2006). In recent years, it has been reported that sodium 3-mercaptopropionate-stabilized GNPs can be produced by adding the citrate salt and an amphiphile surfactant. The size of GNPs can be controlled by changing the stabilizer/gold ratio (Yonezawa and Kunitake, 1999).

The Brust-Schiffrin method for synthesising GNPs is also commonly used on the overall field in recent years. In fact, GNPs can be separated and re-dissolved in normal organic solvents without permanent aggregation or decomposition. This method utilizes thiol ligands that can strongly bind on the gold surface because of the soft characters of both Au and S (Brust et al. 1995), shown in Figure 2-1.

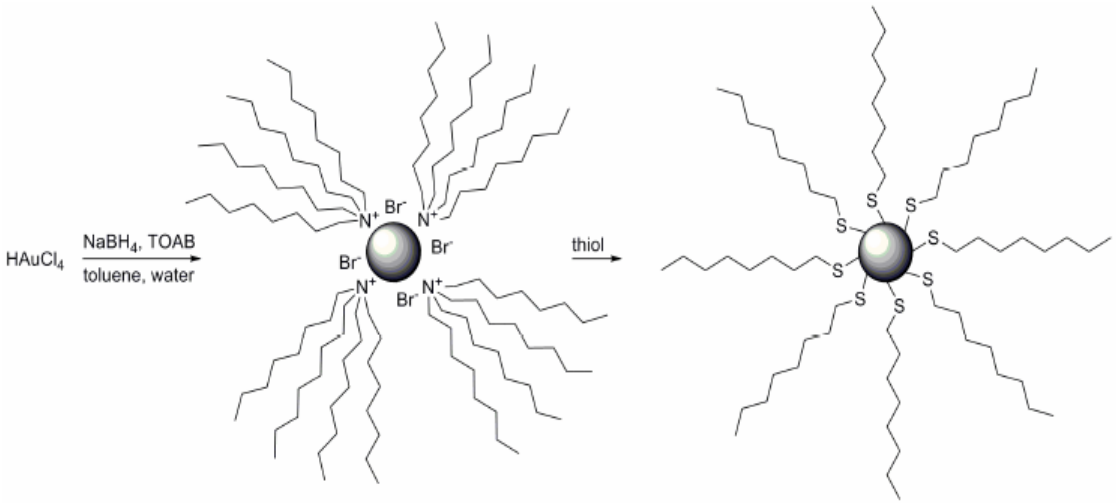

Figure 2-1 Brust method of formation of GNPs with organic shells by reduction of AuIII compounds in the existence of thiols (Daniel et al., 2004)

It has been reported that the Brust-Schiffrin method can produce stable GNPs by adding functional thiols. It has been demonstrated that controlling the ration of thiol: $AuCl_4^-$ in the synthesis can control the size of the GNPs. For example, a 1:6 ratio produces GNPs with an average diameter of 5.2 nm (Daniel et al. 2004).

Moreover, the biosynthesis method has been developed to synthesis GNPs (Song et al., 2009, Ogi et al., 2010). Patungwasa et al. (2007) and Qin et al. (2008) reported that changing pH value of the solutions can affect the morphology of GNPs (Patungwasa and Hodak, 2008, Nam et al., 2009). The sonochemical and microwave assisted synthesis are also commonly used to prepare GNPs (Tsuji et al., 2005, Lee et al., 2010, Naveenraj et al., 2010, Radziuk et al., 2010, Vargas-Hernandez et al., 2010).

For better control of nanoparticle morphology, sonochemical technique especially ultrasound is an effective tool. The technique is based on the acoustic cavitation and rapid collapse of small bubbles in sonicated solutions, which promotes the reaction to

be more homogeneous. A number of metallic based spherical particles with narrow size distribution, i.e. Au, Tl, Pt, Pd, Fe, MnO_2, and CdS, have been successfully produced ultrasonically (Caruso et al., 2002, Li et al., 2006a, Radziuk et al., 2010).

Encouraging results have been obtained in physical and biological experiments by using GNPs produced by the citrate reduction method. However, the impurities of GNP dispersion, which includes residual reactants and non-GNP components, are left in the obtained GNP dispersion. The purification process is very important to separate these impurities before any further tests.

It is difficult to clarify the nanoparticle effect without excluding this impurity effect because non-GNP components can result in the disturbance producing misleading results. For example, one recent study has shown that the rapid temperature increase upon RF radiation on a gold dispersion may be caused by the impurities (Li et al. 2011). It has also been reported that excess sodium citrate remained in GNP dispersions could induce cytotoxicity (Uboldi et al., 2009).

Currently, some common methods have been employed to purify GNP dispersions including dialysis, centrifugation, solvent extraction and chromatography. The most popular methods are dialysis and centrifugation. The solvent extraction and chromatography methods require high cost and long duration, wasting a lot of products during the purification process.

The centrifugation method is an easy and fast process. The speed and duration need to be controlled properly otherwise many products may get lost if the speed is too high or

the duration is too long. For instance, Balasubramanian et al. (2010) have reported that the force of centrifugation higher than 9000g, GNPs were strongly packed and tightly adhered on the wall of the centrifuge tubes. Producing large quantities of nanoparticles is also a challenge for using the centrifugation method (Balasubramanian et al., 2010).

The dialysis method is low cost and convenient to use, requiring only simple devices. The synthesis of colloidal nanoparticles contains the utilization of ionic salts, some of which being used in excess, and purification process of membrane dialysis can be used for removing unreacted salts. It depends on the diffusion of molecules through a permeable membrane because of the difference of concentration between both sides of the membrane. The dissolved substances that are unreacted ions or un-adsorbed organic molecules move from the high concentration site (inside the membrane) to the low concentration site (outside the membrane). A dialysis process scheme is shown in Figure 2-2. The washing medium keeps stirring and regularly changed a fresh one around 10 times up to at least 72 hours and by doing this can regenerate the concentration gradient and accelerate the purification process (Al-Kattan et al., 2011). Dialysis method is low cost, convenience, simple device required. During this process does not or less waste products but it is a long duration (Urata et al., 2009).

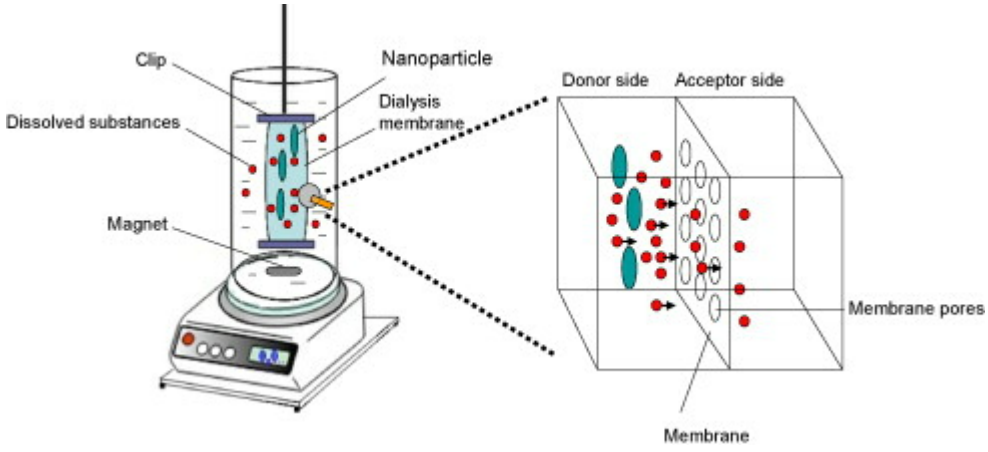

Figure 2-2 scheme of membrane dialysis process, reprinted from (Al-Kattan et al., 2011)

2.2 Cellular uptake and cytotoxicity of GNPs

It is necessary to investigate the doses of GNPs performing the predetermined heating impact without any cytotoxicity. Currently, there is limited information about the short-term and long-term effects of GNPs on the human health, in particular the influences of particle size, shape, and surface function on the uptake, bioavailability and metabolism of the gold nanomaterials. According to Connor's research, 18nm GNPs with citrate and biotin surface modifiers did not present cytotoxicity up to a concentration of 250 μM/L (Connor et al., 2005). Another study has done by Gannon et al. on the cytotoxicity of GNPs in 5 nm, the result revealed that GNPs had no significant influence on Panc-1 or Hep3B cellular proliferation at the concentrations of 1 μM/L, 10 μM/L, and 67 μM/L (Gannon et al., 2008). Currently, gold compounds have been utilized in the medical application, and approved by the Food and Drug Administration (FDA). The FDA has authorized intramuscular gold and oral gold compounds to treat rheumatoid arthritis and has revealed positive curative effect (Rau, 2005). However, it is still not clearly understood that the possible toxicity of GNPs in human body, which demands further research. Moreover, the GNPs themselves may not harm human body but some precursors of nanoparticles and surface modifiers may be harmful. It has been reported that GNPs are neutral and do not induce specific cell responses and the likely side effect are due to the coated chemical groups or surface modifiers (Patra et al., 2007).

In addition, mammalian cells can promptly endocytose GNPs and the kinetics and saturation are related to the size of the GNPs. It has been reported that the size of GNPs in 5 nm would have a high loading ability. It is possible that small size GNPs can escape from the mononuclear phagocytic cells catching and passing through the smallest capillary in the human vasculature (Gannon et al., 2008). It has been shown

that the existence of intracellular GNPs around 13 nm, which resulted in the reduction of actin stress fibers and caused main negative influences on the cell viability (Pernodet et al., 2006). In order to using GNPs in clinical practice, further research about the cytotoxicity of GNPs in different concentrations is in great need. In spite of these unclear factors, GNPs is a good potential candidate to target cancer cells for thermal cancer treatments due to its excellent thermal and electrical properties and great biocompatibility.

2.3 Controlling particle morphology to tuning SPR to NIR region

Generally speaking, photons can overlap with the plasma resonance of the conduction electrons on the surface of metal nanoparticles to generate their collective oscillations that commonly is known as surface plasmon resonance (SPR). Moreover, the optical properties of metal nanoparticles are correspondent to their SPR band (Ghosh and Pal, 2007). By controlling the structure and shape of GNPs, the SPR frequency of GNPs can be adjusted to near infrared (NIR) region where the light penetration depth in tissue is deep. The absorption coefficient of the human tissue is two orders of magnitudes higher in the visible region at 400–600 nm than that in the NIR region at 650–900 nm, shown in Figure 2-3. Because of the minimal absorption by water and hemoglobin at these wavelengths, NIR transmission in human tissues can be achieved at least several centimetres based on the tissue types, (Weissleder, 2001). Due to this reason, many attentions have been paid to NIR-absorbing gold-based nanoparticles.

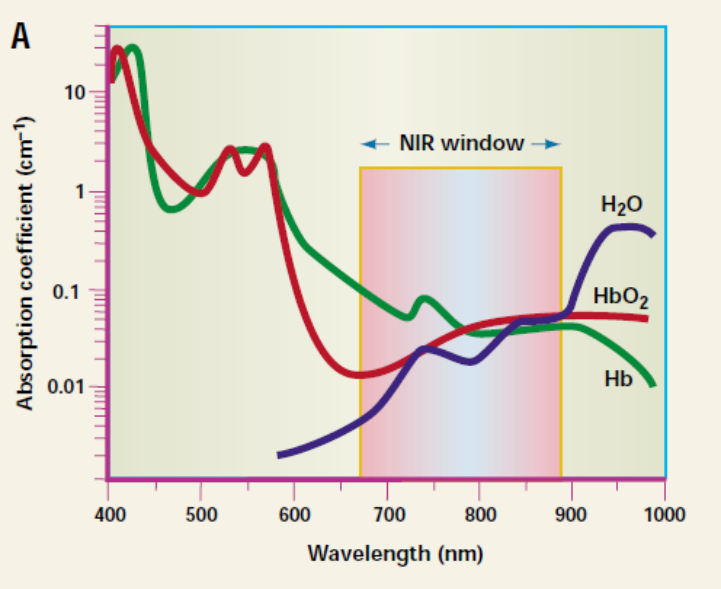

Figure 2-3 The NIR window from 650 nm to 900 nm, minimal light absorption by human tissue, i.e. haemoglobin (<650 nm) and water (>900 nm) (Weissleder, 2001).

Gold nanocages

Gold nanocages have been synthesized through a galvanic replacement reaction developed and first studied by Xia group in 2002. In general, the first step is synthesis of Ag nanocubesas as a template through reducing $AgNO_3$ with ethylene glycol (EG) in the presence of poly (vinyl pyrrolidone) (PVP) at about 150- 160 ℃. Secondly, Galvanic replacement is taken place at these Ag nanocubes by adding $HAuCl_4$ to produce gold nanocages. Owing to the different electrochemical potentials between these Ag and Au, Ag abandon its electrons and liquefy into the solution as ions when gold is being adhered to the outer surface of the cube. The reaction is keeping continuing, more and more Ag from the interior of the cube will be taken away from a small pit in the cubic wall, shaping a hollow Au-Ag alloyed nanobox and by adjusting the amount of $HAuCl_4$ added can control the wall thickness. Au nanocages with a highly porous structure were formed when the Ag was removed by $HAuCl_4$ from the Au-Ag alloy walls in a late stage of the reaction (Sun and Xia, 2004). Proper adjusting

the amount of $HAuCl_4$ provides the control of the wall thickness. For instance, increasing the volume of $HAuCl_4$ produced thinner and porous wall of gold nanocages, shown in Figure 2-4. Altering the wall thickness, the hole size and porosity of gold cages are able to switch the SPR wavelength from the visible to the NIR area.

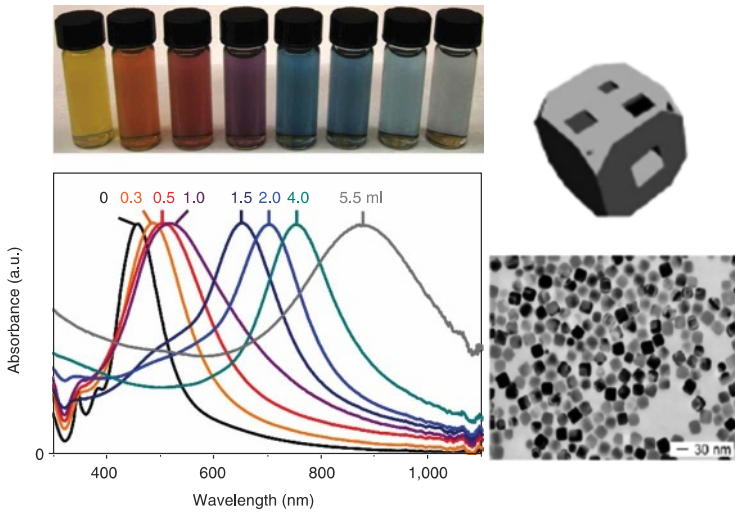

Figure 2-4 left top: solutions of gold nanocages adding different amount of 0.1 mM HAuCl4 solution: 0, 0.3, 0.5, 1.0, 1.5, 2.0, 4.0 and 5.5 ml (left to right), left bottom: The corresponding UV-visible absorbance spectra of gold nanocages. The absorbance peak of the gold nanocages was switched from the visible to near-infaraed area by altering the amount of HAuCl4 solution. Right: TEM image of gold nanocages. Reprinted from(Skrabalak et al., 2007b, Xia et al., 2011)

Gold nanoplates

Different synthesis methods have been employed to produce plate-like nanomaterials (known as nanodisks, nanoprisms or nanotriangles). Examples include photochemical syntheses including visible light (Jin et al., 2003) and thermal syntheses containing microwave- and ultrasound- assisted methods (Tsuji et al., 2003, Wang and Wang, 2007, Li et al., 2006a). No matter which method use to produce nanoplates, the resulting structures have common architectural elements and have similar chemical and physical properties. Generally, the shape of nanoplates can be made flat in triangular, hexagonal,

or circular shapes with large aspect ratios. The gold nanoplates usually display edge lengths in the range of 40 nm to 1 mm and the thickness in the range of 5 nm to 50 nm. The size of nanoplates can be controlled by changing the ratios of metal ion to the reducing agent (Me´traux et al., 2005), the concentrations of surfactant (Sau et al., 2004), and the electromagnetic irradiation wavelength (Jin et al., 2003) as well as the concentration and type of seed particle (Ah et al., 2005; Millstone et al., 2006). It is worth mentioning that SPR of nanoplates can be turned from the visible to NIR regions of the spectrum by controlling the edge length, thickness, and tip morphology of nanoplates. It has been reported that the edge and thin of nanoplates (aspect ratio >10) can induce dipole and quadrupole plasmon resonances, which can be tuned by the frequency and extinction cross section (Shuford et al., 2005). Recently, Pelaz et al showed that SPR band of gold nanoplates can be switched to NIR area by changing the concentration of molar ratio of $HAuCl_4$ and reducing agent to control the size of nanplates, shown in Figure 2-5 (Pelaz et al., 2012).

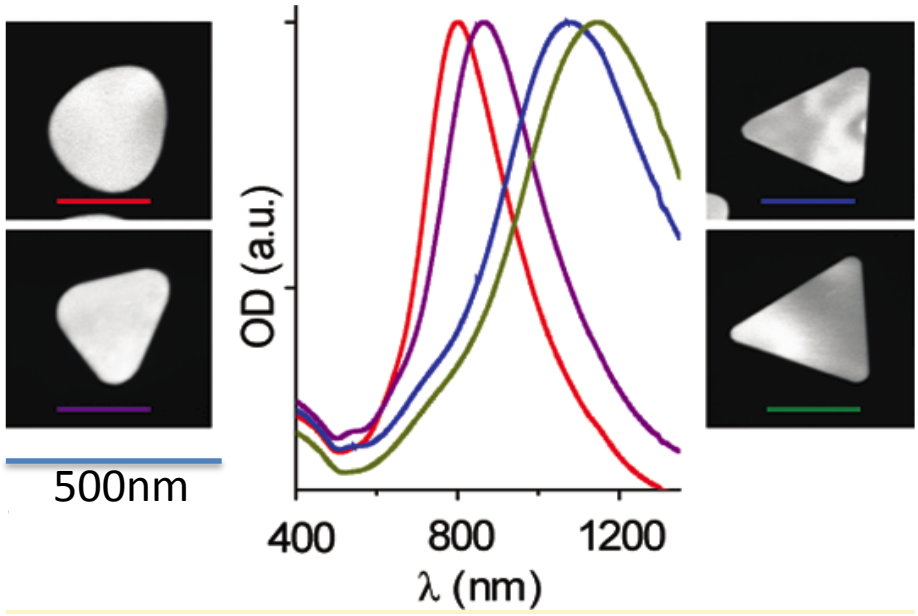

Figure 2-5 the corresponding UV-visible absorbance spectra of different shape and size of nanoplates. Reprinted from (Pelaz et al., 2012).

In recent years, the SPR of nanomaterials have been designed and engineered to apply in the NIR region. These SPR of gold nanomaterials in the NIR area are particularly efficient to convert NIR light into heat, and have been employed successfully in many biomedical applications, i.e. photothermal treatment, drug release and images (Cobley et al., 2010, Yavuz et al., 2009, Rang et al., 2008).

Fe_3O_4 nanoparticles

In recent years, the Fe_3O_4 nanoparticles have attracted many interests in research because of their potential uses for biomedical applications such as magnetic resonance imaging as contrast agents (Hu et al., 2013), magnetic drug targeting and delivery (Su et al., 2012), and hyperthermia (Ghosh et al., 2011).

There are many various ways to prepare Fe3O4 nanoparticles, which include physical methods, wet chemical preparation methods and microbial methods. Physical methods contain electron beam lithography and gas-phase deposition. However, particles produced by these methods cannot control the particle size within the nanoscale range and well-dispersed Fe3O4 nanoparticles also cannot meet the requirement.

Wet chemical preparation methods are able to directly prepare well-dispersed Fe3O4 nanoparticles and the particle size can be well controlled within nanoscale range. Moreover, the desired particle shape and sizes can be produced when reaction temperature, stirring rate, surfactant concentration and solute concentration as well as solution pH are well controlled during the synthesis process. The Massart

coprecipitation method is the common way to obtain Fe_3O_4 nanoparticles (Massart, 1981) and magnetite is produced by alkaline coprecipitation of stoichiometric amounts of ferrous and ferric salts， with maintaining a molar ratio of Fe_2^+: Fe_3^+=1:2. During the whole process, Argon is employed to protect divalent iron salts from oxidation. Moreover, a suitable surfactant can be chosen to functionalize the nanoparticle surface, such as citric acid, sodium oleate and polyethylene glycol.

The use of Fe_3O_4 nanoparticles as heat mediators has been extensively investigated and applied for Hyperthermia. The process involved the delivery of Fe_3O_4 nanoparticles into a targeted tissue and then applying an electromagnetic field of sufficient strength and frequency, allowing heat generation. The heat generation by Fe_3O_4 nanoparticles exposed under the electromagnetic field are due to the Brownian and Ne´el relaxations as well as hysteretic loses (Rosensweig RE, 2002). As the particle size is smaller than about 20 nm which is not more than one single magnetic domain, the Brownian and Ne´el relaxation becomes the sole dominating mechanism. While Hysteretic loses dominate for nanoparticles size between 20 nm and 100 nm (Hergt et al., 2008). It is important to tailor particle size and ensure nanoparticles well disperse to achieve the most effective heating effect the electromagnetic field. For example, Khandhar's group has investigated Fe_3O_4 nanoparticles with controlled particle size and size distribution (16± 30%) and exposed under the electromagnetic field at 373 kHz. The results have shown that optimized Fe_3O_4 nanoparticles and their narrow size distributions have highest specific absorption rate and maximum efficiency in decreasing cell viability (40%) (Khandhar et al., 2011). Ghosh et al., have also investigated Fe_3O_4 nanoparticles with size distribution from 3 nm to 25 nm and exposed to an electromagnetic field at the

frequency of 265 kHz. The results have shown that 35% decrease in viability was observed in human breast cancer cells (MCF7) with Fe_3O_4 nanoparticles after treatment compared to the untreated control, which was further enhanced (65%) under induction heating conditions (Ghosh et al., 2011).

Microcapsules

A microcapsule normally contains a core material wrapped by a single or multi-layered shell. The core material can be the core, internal phase or fill. The size of microcapsules with size from 1 μm to 1000 μm in diameter. Using the layer-by-layer (LbL) assembly technique can fabricate capsules, with well-controlled size and shape, variable wall compositions and changed wall thickness. Microencapsulation technologies produce micron- and nano-sized containers with capability to encapsulate or release substances with the assistance of triggers.

The preparation processes of LbL polymeric capsules are briefly summarized in Figure 2-6 (Bédard et al., 2010). The LbL assembly is usually referred to electrostatic self-assembly, which basically depends on the electrostatic interaction between the neighboring layers. During the preparation procedures, the capsules are fabricated in solution by the self- assembly processes where polymer solution is added sequentially and then followed by the centrifugation to separate the coated colloids from the supernatant. When the desired LbL composition is achieved, the original core can be dissolved to obtain hollow polymeric capsules.

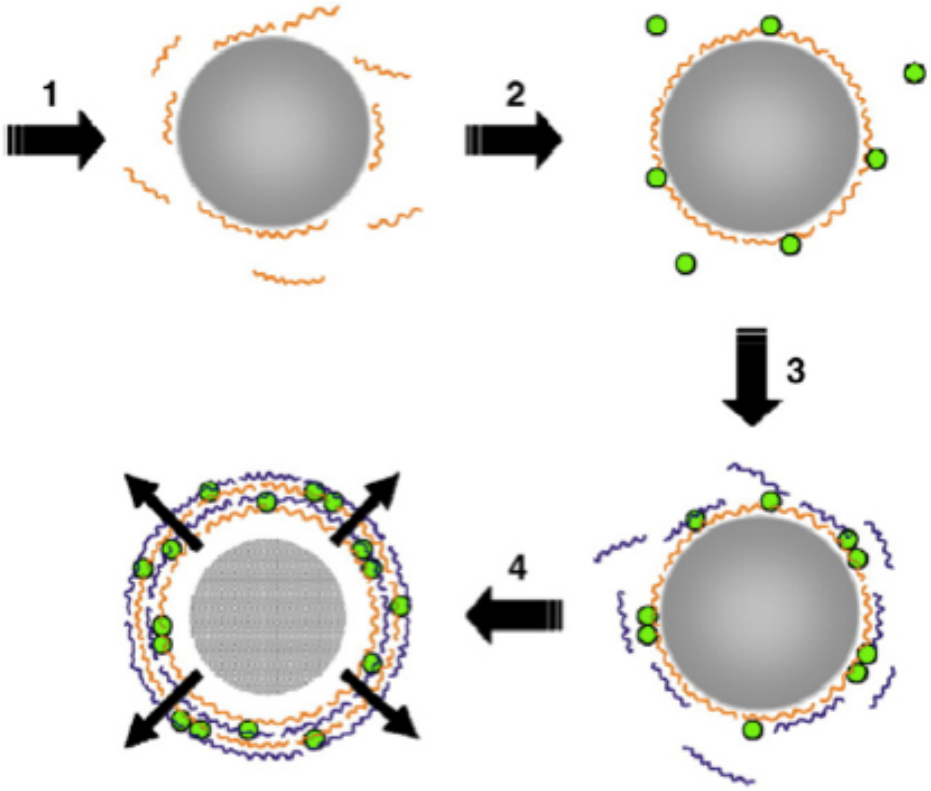

Figure 2-6 Schematic of the layer-by-layer assembly of polymeric microcapsules. Reprinted from (Bédard et al., 2010). The process starts by coating a charged colloid with a polyelectrolyte of opposite charge (1). An oppositely charged molecule (2) or polyelectrolyte (3) can then be used to coat the first layer. These steps may be repeatedto produce multi－layers. The subsequent dissolution of the template (4) produces a hollow polymeric shell.

Because the layers of polyelectrolyte microcapsules are held together mainly by electrostatic forces, charged nanoparticles can be combined into the polyelectrolyte layers. According to the type of combined nanoparticles, the modified capsules are able to response external energy sources, such as electromagnetic irradiation ultrasound, shown in Figure 2-7. For example, laser irradiation at visible or near infrared regime has been used to remotely release the polymer capsules embedded with metal nanoparticles. Capsules embedded with silver or GNPs in their shell could be opened by laser irradiation due to the temperature increase of the metal nanoparticles induced by light

absorption (Guo et al., 2011). Magnetic energy has been utilized to release encapsulated material from capsules incorporated with magnetic nanoparticles, such as Fe_3O_4 nanoparticles. As the capsules with magnetic nanoparticles were exposed under an oscillating magnetic field, heat is produced, which resulted in the damage of the capsule walls, the increase of the wall's permeability, and the release of the encapsulated substances (Hu et al., 2008). Ultrasound has also been used to release the encapsulated material from multilayer microcapsules embedded silver or GNPs in their walls. When the capsules were exposed under ultrasound, the cavitation effect and the collapse of microbubbles from dissolved gases produced a mechanical and/or thermal effect on the capsules. Nanoparticle modified capsules acted more sensitive to ultrasound exposure comparing with plain capsules (Pavlov et al., 2011a). In addition, microwave was also applied to release capsules with GNPs and the results presented burst-like release of microcapsules (del Mercato et al., 2011).

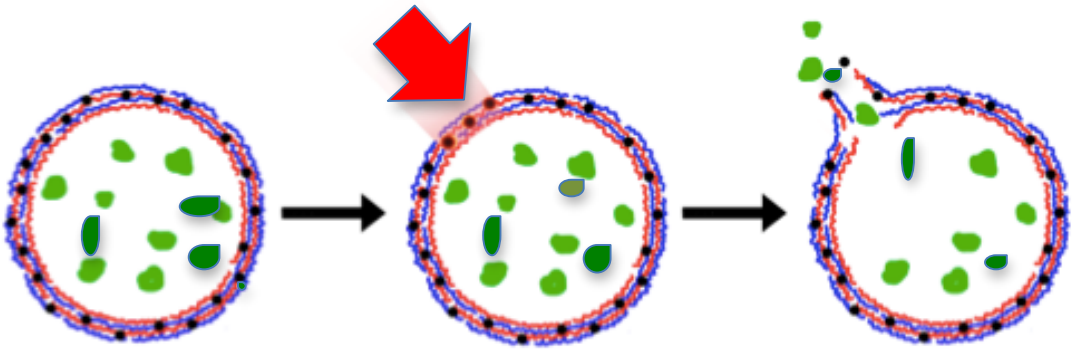

Figure 2-7 Schematic representation of the release of GNP-modified by laser irradiation, reprinted from (Anton Pavlov, 2012).

Many efforts have been investigated in designing new developments on the release of polymeric microcapsules. Also, much focus has been devoted to the investigation of sensitive microcapsules under electromagnetic fields in living cells and tissues (Skirtach et al., 2006, Pavlov et al., 2011b). However, many improvements are still required to

achieve more sensible and rapid release of microcapsule and better permeability control for hyperthermia applications.

2.4 Nanoparticles applied in hyperthermia

Hyperthermia involves the transfer of heat energy into or out of bodily tissues to achieve a therapeutic result (Shenoi et al., 2009). Hyperthermia includes ultrasonic, photothermal therapy, microwave and radiofrequency ablation. Ultrasonic, microwave and radiofrequency ablation are relatively deep penetrating hyperthermia methods where the energy is delivered to deeper site such as liver, kidney and breast. Hyperthermia is flexible, low cost and minimal invasive treatment compare with surgery. However, it has many drawbacks such as skin burn, thermal damage of adjacent healthy tissue and limited therapic area (Ensminger and Stulen, 2010, Manthe et al., 2010).

2.4.1 Microwave Ablation

Microwave ablation is a kind of invasive hyperthermia that diseased tissue is heated by an EM device within the microwave frequency range to damage tumor. Microwave ablation equipment is able to kill tumor directly though a small applicator. Because of its high frequency at 2.45 GHz, its penetration depth is shallower than that of Radiofrequency ablation. Recently, microwave ablation with nanomaterials has been studied to improve conventional microwave ablation. Mashal et al. have investigated that single-walled carbon nanotubes (SWCNs) were combined with breast tissue mimicking material to fabricate jelly-like samples for breast cancer thermal therapy. The electromagnetic microwave device at 3 GHz was utilized to heat breast tissue mimicking material with different concentrations of SWCNs. The result presented that

samples with higher concentration SWCNs were heated up faster and suggested that SWCNs may enhance microwave hyperthermia of breast cancer (Mashal et al., 2010).

This research studied breast tissue mimicking material with SWCNs was used for microwave hyperthermia of breast cancer. The dielectric properties with varying concentrations of SWCNs were evaluated by open-ended coaxial probe at frequency from 0.6 to 20 GHz and results showed that relative permittivity and effective conductivity were increased as the concentration of SWCMs was increased. Also, SWCN samples at higher concentration were heated up faster under EM field at 3.0 GHz. This phenomenon was based on the effective conductivity.

Cook et al. (2010) have investigated the magnetite nanoparticles mediated microwave ablation which used the EM irradiation at 2.45 GHz to heat porcine muscle tissue injected iron-oxide nanoparticles. The result presented that 25˚C increase within 50 seconds in the targeted site and around 17˚C increase was observed in surrounding tissue. According to the results, magnetite nanoparticles enhanced MW energy abortion presented in bulk temperature increase, but the temperature increase of 17˚C was also observed in the tissue without nanoparticles. This would also get thermal damage in this region. (Cook et al., 2010).

Very recently, Ghahremani has reported that microwave hyperthermia efficacy with chemotherapy in the presence and absence of GNPs (Ghahremani et al., 2011). Size effect of GNPs in size 20 nm and 40 nm has been studied in this research and MTT assay was carried out to investigate the effectiveness of therapeutic parameters on cell survival. The effectiveness of microwave hyperthermia with GNPs was presented in the

cell survival after 48 hours. The result showed that the highest concentration at 26.4 mg/ml of 40 nm GNPs showed the most effective because survival rate dropped down to 4.1%. In this study the bulk temperature as the heating response of microwave hyperthermia was not yet reported and did not explain how to separate 2 different sizes of GNPs in 20 nm and 40 nm because the size distribution of their GNPs sample was very wide from 25 nm to 100 nm.

Today microwave ablation plays an important role in both research areas and clinical practice applications, the research into this area involved with nanomaterials would be beneficial not only to understand of nanomaterials but also exploring potential applications.

2.4.2 Ultrasound-induced hyperthermia

Ultrasound has been widely used in our daily life and some of the most notable applications are in medicine for diagnosis and treatment. High Intensity Focused Ultrasound (HIFU) is one of the most common used thermal therapies for deep tumour such as prostate, liver, kidney, and breast. HIFU propagates and focus ultrasonic beams to cause thermal injury in targeted sides. Diagnostic ultrasound is also built in HIFU to local the target place and track the treatment effects. Compare to Radiofrequency Ablation, HIFU is a minimal or no invasive treatment because it is not necessary to insert a probe into the tumour or need an incision. However, the drawbacks of HIFU: 1) the treatment time is too long due to its small focus volume. 2) Temperature increase causes damage in healthy tissue surrounding the targeted sites and changes the speed of sound. 3) Alteration of sound speed distorts images in its diagnostic system thus reduce

treatment effects. 4) HIFU can be used as an invasive treatment. Wound and skin burn are caused in that case.

In order to prevent the drawbacks and side-effects of HIFU as well as enhance treatment effects, some groups have devoted themselves to investigating magnetic nanoparticles as energy absorbing agents applying in HIFU. For example, Smith et al. have studied magnetite nanoparticle agglomerates improving the temperature increase of inertial cavitation induced by HIFU to destroy tumor as well as to release and cellular uptake of drugs (Ho et al., 2011, Smith et al., 2009). Lin et al. have reported pulsed-focused ultrasound sonication with microbubbles was able to improve the vascular permeability of lipid-coated quantum dot nanoparticles in targeted tumors (Lin et al., 2010). Moreover, it is known that GNPs are potentially highly attractive to be applied as an energy-absorbing agent to focus ultrasound sonication for clinical practices.

2.4.3 Near-Infrared photothermal ablation

Laser therapy is a kind of minimal invasive treatment and in this treatment photon energy is converted adequate into heat to destroy cancer. In the last few decades it has been employed to cure cancer and its heating sources containing visible light, infrared and near infrared light are utilized to create adequate temperature increase in a specific target site to kill the cancer cells. The shallow penetration depth of visible light in tissue is a main limiting issue in clinical hyperthermia. Near-infrared laser light is an ideal option for clinical applications owing to the low absorption by human tissue, i.e. water and hemoglobin.

GNPs is able to absorb light strongly and transform photon energy into heat rapidly, so many interest are focused on GNPs as transducer agents for Near-Infrared photothermal treatment. Recently, this GNPs assisted Near-Infrared photothermal treatment has presented popularity and success on the morphology controlled synthesis of some Au-based nanoparticles, including gold nanoshells, gold nanorods and gold nanocages as well as gold nanoprimes, to convert NIR photon energy into heat to damage cancer cells (Pelaz et al., 2012, Dickerson et al., 2008, Loo et al., 2004, Chen et al., 2005). GNPs mediated photothermal therapies were specially designed to drive wavelengths in this NIR window to minimize diminution of the energy causing from unexpected light–tissue interactions, and to avoid adverse and harmful heating on healthy tissue. Hirsch group have reported that gold–silica nanoshells were injected into mice tumour and exposed under continuous wave NIR light at 820 nm to cause a 4–6 mm depth of thermal injury in the targeted site (Hirsch et al., 2003). A research has been done by Xia group and showed that the achievability of gold nanocages for NIR pohtothermal treatment in vitro. Breast cancer cells conjugated with gold nanocages were killed by NIR laser at 1.5–4.7 W/cm^2 and the damaged area was linearly based on the power density. The cell death efficiency rose with rising laser treatment time (Chen et al., 2007). Pelazet et al. have synthesised gold nanoprisms to absorb NIR irradiations and convert the absorbed energy into heat and this generated heat is able to cause thermal injury in targeted site (Pelaz et al., 2012). These quantitative studies are focused on tailoring their gold based-nanomaterials and turning the surface plasmon band of gold materials to the near-infrared region. The overlap of the wavelengths between the nanomaterial and laser can achieve better outcomes of photothermal treatment.

2.4.4 Radiofrequency ablation

Radiofrequency ablation (RFA) is currently used in clinical practice to treat some solid tumors such as liver, kidney and lung tumors, and this technology uses high-frequency alternating current passing through the needle electrodes into tumors meanwhile produces heat to destroy cancer cells under imaging guidance. However, the defects of this technique contain the invasive treatment and the limitation of tumor size as well as thermal injury not only in tumors but also in healthy tissues which surround the needle electrode.

Different from laser-based photothermal therapy, electromagnetic irradiation in RF spectrum can penetrate more deeply, which can reach tens of centimetres in the targeted site of the body. It has been shown that higher specific absorption rate (SAR) is observed by using GNPs under RF field generated by the Kanzius heating system (Gannon et al., 2008, Cardinal et al., 2008, Kruse et al., 2011, Glazer et al., 2010). Recently some effort have been put in non-invasive radiofrequency cancer therapy where functionalized GNPs have been proposed as potential agents for non-invasive treatment and the feasibility has been proven in preliminary studies on non-targeted particles in vitro, and later in vivo (Gannon et al., 2008, Cardinal et al., 2008, Kruse et al., 2011, Glazer et al., 2010).

Gannon et al. (2008) used 5 nm GNPs synthesised by the Brust-Schiffrin method. 1.0 ml GNP specimens at concentrations of 1.1 μM/L, 11.1 μM/L, 33.5 μM/L, and 67 μM/L in DI water were exposed on RF field at powers of 200 W, 400 W, 600 W, and 800 W, respectively. When GNP concentration and RF generator power were increased, the

more significant temperature increase was contributed. The results showed that the temperature increase with heating time is in a non-linear way, shown in Figure 2-8.

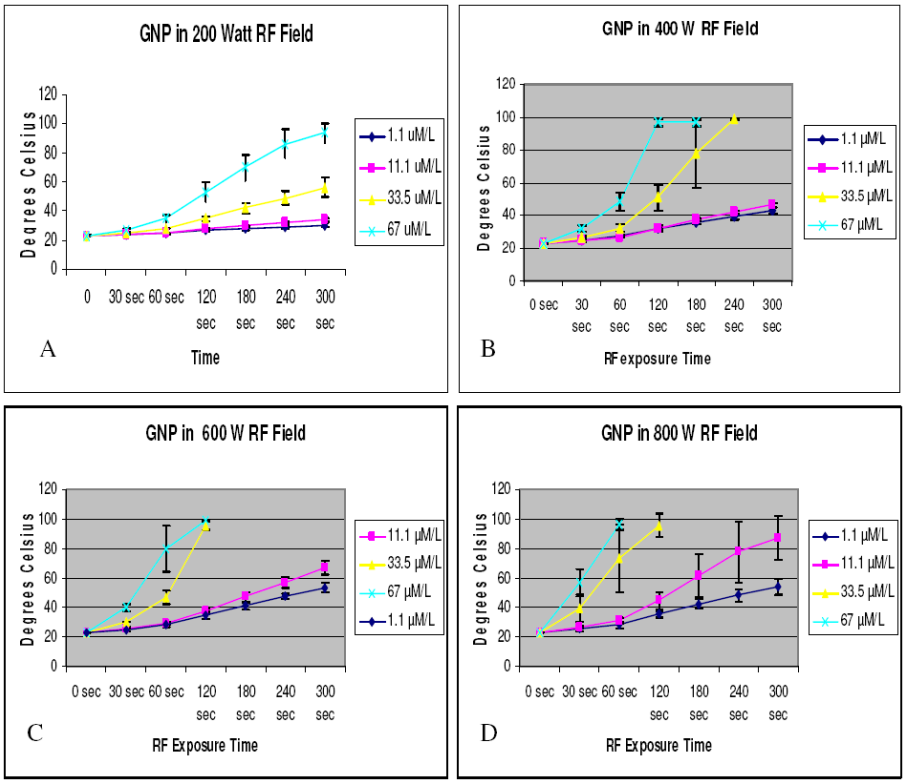

Figure 2-8 The heating effect of GNP dispersions at different concentrations exposed to external RF fields (a) 200 W; (b) 400 W; (c) 600 W; (d) 800 W. Reprinted from Cannon et al., 2008.

MTT assays showed that GNPs had no significant influence on Panc-1 or Hep3B cellular proliferation at any of the concentrations measured. In addition, PI-FACS results demonstrated that GNPs alone at all concentrations created no proof of necrosis in either Hep3B or Panc-1 cells; both cell lines presented normal cell cycle elements. As both Hep3B or Panc-1 cells with 67 µmol/L GNPs were exposed under the RF field, higher rates of cell death than the control samples without GNPs were observed, shown in Table 2-1.

Table 2-1 Cell death rate of Hep-3B and Panc-1 human cancer with 67 μmol/L GNPs after external RF treatment. Reprinted from Cannon et al., 2008.

Cell type and treatment				
RF exposure	Hep-3B control Cell death (%)	Hep-3B GNPs Cell death (%)	Panc-1 control Cell death (%)	Panc-1 GNPs Cell death (%)
5 minutes	75.0±12.2	99.8±3.1	39.8±34.0	96.5±8.4
2 minutes	21±14.1	98.5±0.5	26.4±15.8	98.7±3.7
1 minute	17.6±8.4	99.0±0.2	15.3±9.8	98.5±2.1

In Cardinal's research, GNP suspensions containing 13 nm GNPs were exposed under the 13.56 MHz EM field at 50 W. The results showed that the temperature increased non-linearly with heating time, as shown in Figure 2-9. The heating effects of GNP dispersions are greatly enhanced compared with deionised water along (Cardinal et al., 2008).

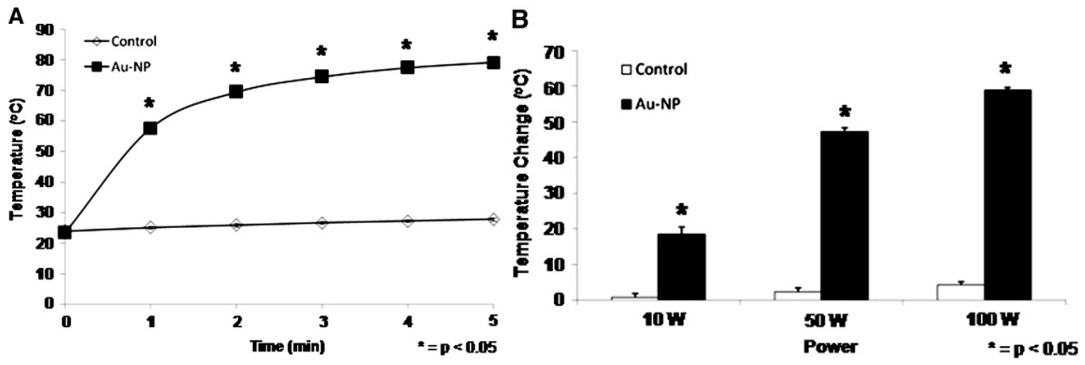

Figure 2-9 GNP solutions were heated selectively and efficiently in RF field. A, Solutions of GNPs or water were exposed to the 13.56 MHz EM field at 50W. B, Solutions of GNPs or water were exposed to the RF field at 10, 50, or 100 W and temperatures were measured after 3 minutes, reprinted from Cardinal et al., 2008.

In vitro trail, HepG2 cells coupled with GNPs presented significant heating effect in cell death after the RF exposure at 35 W for 7 minutes. Cell death was evaluated by LDH

assay, around 80% of cell death was observed in the group with gold nanoparticle treatment after the RF heating for 7 minutes. Additionally, *in vivo* subcutaneous injections of GNPs caused tissue destruction after the RF exposure at 35 W for 2 minutes and temperature increase revealed more significant in the GNP injection site than in same targeted site of control (H_2O-injected) rats. After that, histopathologic assessment of GNP injection site showed loss of tissue architecture, loss of membrane integrity and infiltration of inflammatory cells. Also, *in vivo* GNP injections in a rat hepatoma model leaded to tumor ablation after the RF exposure at 35 W for 2 minutes, the result showed that significant temperature increase in the GNP-injected site was achieved as compared with controls. Histopathologic assessment of tumor modules displayed that widespread tumor cell disaggregation with nuclear hyperchromatism, cytoplasmic retraction, and areas of apoptosis and cell fragmentation. These results suggested that heat generated from GNPs in the microenvironment of the cells was adequate to induce lethal injury in the cells (Cardinal et al., 2008).

Recently Glazer`s group used high heating rate of GNPs (Figure 2-10) under the RF irradiation at 13.56 MHz to study human pancreatic xenograft destruction in *vitro* using immunocom promised mice with human pancreatic carcinoma xenografts (Glazer et al., 2010). In this case internalization and cytotoxicity of functioned GNPs are also tested in *vitro*. The results show that apoptosis increased and viability of cancer cells with antibody-conjugated GNPs was decreased after RF exposure. After treatment no evidence of injury was caused in healthy tissue.

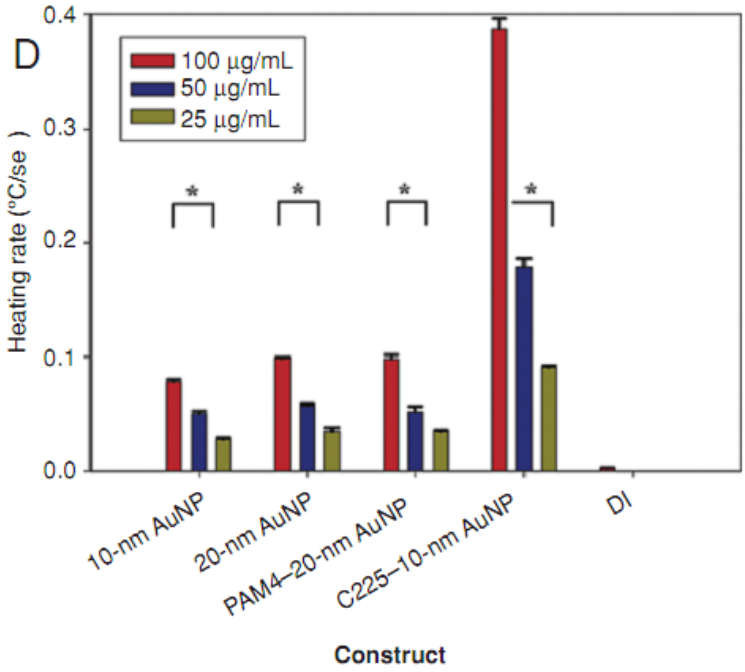

Figure 2-10 heating rate of unconjugated and conjugated GNPs in DI water heat in the RF field in a concentration-dependent manner, reprinting from Glazer et al., 2011

Regarding the nanoparticle mediated RF treatment in animals, there are 2 vital parts to this treatment, and these 2 parts work together to cause cytotoxicity in the targeted site of animals. One is the GNPs and the other one is electromagnetic waves at radio frequency. Spherical GNPs are the common shape used in this therapy and can be coated antibodies to target cancer cells. The antibodies ensure that the GNPs arrive at targeted site into the body and make the minimal damage to healthy cells. For the electromagnetic waves at radio frequency, they are at low frequency and own low tissue-specific absorption rates, thus the penetration of RF electromagnetic waves can achieve deep site of the body. As a result, the radiofrequency waves cause the GNPs in the targeted site to increase significant heat and cause cytotoxicity in the targeted site of animals without doing damage to surrounding healthy tissues.

Some researches have carried out in small animal modules to treat cancer, such as lab rabbits and lab rats. For example, Curley's group has done the investigation about the nanoparticles smaller than 50 nm targeted to the tumour in animals and exposed under the RF electromagnetic field and tumour necrosis after RF field exposure without acute or chronic toxicity to healthy tissues (Glazer ES and Curley SA., 2011). Another example also has be done by Curley's group about the whole body of mouse model was exposed under RF exposure and the bulk temperature of targeting side was increased (Figure 2-11) which was higher than the body surface temperature. The bulk heat transferred from intracellular GNPs (10 nm) to cancer cells to surrounding tissues, which was observed by the IR camera. The result suggested that antibody-GNPs enable to be the agent to induce hyperthermic effect in targeting side under RF exposure and prevent healthy tissue from heat injury. Not only GNPs but also single-walled carbon nanotubes were used in this therapy. SWNT targeted to VX2 tumor in adult New Zealand white rabbits and then exposed under RF field to induce thermal cytotoxicity. The result showed that tumors targeted with SWNTs presented thermal necrosis and nonspecific injury to the surrounding healthy tissue. The animal trail has offered more evidence about the thermal damage in the cancer cells caused by the nanoparticles under RF field to induce cytotoxicity. These evidence reveals on loss of normal tissue architecture, loss of membrane integrity, and infiltration of inflammatory cells after RF treatment.

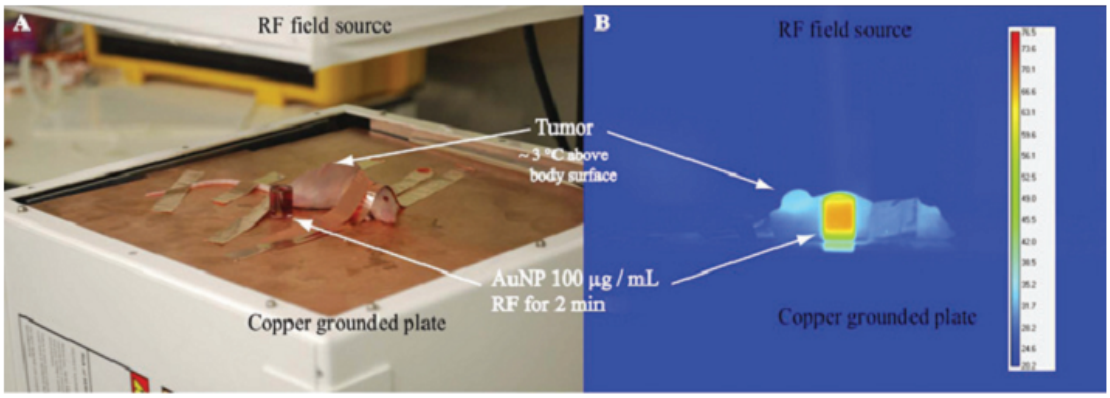

Figure 2-11 (A) mice with pancreatic xenografts in the flank are sedated and grounded to a copper plate with conducting copper tape in order to prevent excess current inducing electrothermal injury. (B) Temperature of the toumor is increased more significantly thanthat of the mouse body due to C C225-mediated AuNP delivery. Reprinting from Glazer et al., 2011

These animal trails show positive results, however, the particle size is a conflicting issue in the use of the RF irradiation and GNPs to cause thermal damage in cancer cells and clearance of the nanoparticles from the body after therapy is complete. Very recently, Sassaroli et al. (2012) and Corr et al. (2012) have reported the GNP heating effect under RF field was dependent on the GNPs size, concentration and surface area (containing the concentration of citrate coating), and the heat production was remarkably reduced as the GNPs are aggregated. The heat production was only observed for GNPs of diameters smaller than 10 nm, which indicated a unique size-dependent heating behavior.

Moreover, regarding the clearance of the nanoparticles from the body after therapy is completed, some groups have reported GNPs persistence in the liver and spleen in mice for up to 6 months with no observed consequences. Sadauskas et al. has found that minimal elimination of 40 nm GNPs from the liver, with around 16.6 μg of GNPs remained after 6 months and 90% of the amount measured after 24 hours (Sadauskas et

al., 2009). This suggested that GNPs might be remained in liver permanently because the GNP level has not return to baseline after GNP administration. Balogh et al. have reported that 46% of the initial dose of 5 nm GNPs was excreted after 5 days. However, for 11 and 22 nm GNPs only about 10% excretion of the initial dose were detected (Balong et al., 2007). This resistance might be related to the particle size as the particle size is too big to be filtered from the kidney. Glazer et al. 2012 reported that the diameter of nanoparticles should be smaller than 5 nm to be excreted by the renal route from the rabbit body. Larger GNPs (25 nm) were found more equally in between the liver, spleen, and tumor tissue in the rabbit body of liver cancer (Glazer et al. 2011).

According to FDA requirements, the drugs should be eliminated via excretion processes or metabolism after being taken by the body. Drug elimination decreases toxicity and avoids drug accumulation. Nanoparticles should be designed to eliminate from the body. Moreover, as the particle size in the majority of the studies are bigger than the renal filtration cutoff, thus it is very important to consider the route of nanoparticle elimination including renal excretion, metabolism and the reticuloendothelial system. Also, long-term studies on gold nanoparticles require further investigation.

According to the Food and Drug Administration (FDA), the criteria of the power of present RFA machine is under 200W in clinical practice. In Cardinal's research, the powers of RF field were between 35W to 100W for heating GNP suspensions and 35W in *vivo* and in *vitro* tests. These volumes of power meeted at a requirement of FDA. By contrast, in Gannon's research the powers of RF were from 200W to 800W for heating GNP suspensions and they did not mention the power of RF in *vivo* test. The power of

RF field used in Glazer`s group is 600W. It can be showed that the volumes of the power were out of FDA standard. It is extremely vital to look at the duration, power of the RF field to prevent from harming healthy tissues. This novel RF therapy is a non-invasive treatment, thus FDA would require another criteria of the power when this treatment is used in clinical practice.

As positive results mentioned above (Gannon et al., 2008, Cardinal et al., 2008, Kruse et al., 2011, Glazer et al., 2010), an electromagnetic wave in radiofrequency (RF) spectrum at 13.56 MHz is used to study non-invasive RFA with GNPs because RF radiation can penetrate deeply into tissue compare with laser irradiation. These positive results were obtained in physical and biological experiments and a wide range of factors related to RF heating effect generated by GNPs mediated Kanzius heating system at 13.56 MHz. During these case, rapidly temperature increase and cell death ratio are the most considered. However, several issues should be considered carefully:

- Is the heating effect generated by GNPs alone?
- What is the heating mechanism of GNP suspension under the EM field?

One recent study conducted by Li's group on gold impurity effect indicated that the rapid temperature increase may cause by the impurities and the absorption of RF energy by GNPs might be negligible (Li et al., 2011). Li's results were still based on commercial GNP dispersions and tested supernatant separated by centrifuging at 13,000 rpm for 15–30 minutes might be insufficiency due to small amount of GNPs residual. Balasubramanian group suggested that 20-nm gold dispersion lose 20% of GNPs after twice round of centrifugation operating at 7000g (13000rpm) for 20 minutes (Balasubramanian et al. 2010). For synthesis GNPs, the liquid route synthesis is

preferred, which typically involves chemical reactions of a few reagents with one desired product. Through a hydrothermal chemical reduction subsequent separation and purification are very important process before any further tests due to impurities of obtained gold dispersion which contain residual reactants and non-GNP components in obtained gold dispersion. In addition, these impurities could damage viability of human cells and cause cytotoxicity in cells (Balasubramanian et al., 2010). It is difficult to clarify the nanoparticle effect without excluding this impurity effect.

2.5 Research motivations and aims

An innovative motivation in the field of nanomaterial science and tumor biology has been come up with for a positive possibility of achieving the long-sought after goal of employing GNPs to target tumor cells for thermal cancer therapy. Moreover, the previous researches stimulate a motivation of this project to look at controlled synthesis of nanomaterials, the heating and interaction of nanomaterials with external electromagnetic and ultrasonic fields, and their potential applications in non-invasive heat-related biomedicines. According to these previous researches, it is known that GNPs are potentially highly attractive to be applied as an agent to focus and dissipate electromagnetic wave because of their good thermal, electrical and optical properties. GNPs can localize and enhanced dissipation of RF energy as well as easy functionalize to target biochemical cell-markers associated with the specific diseases. Moreover, it is shown that physical and chemical behaviors are strongly dependent on the morphology and concentration of GNPs, thus control of size and shape is very vital for changing its properties over a broad range.

At present, numerous efforts are put on fabricating mental nanoparticles by sonochemical methods. However, an ultrasonic irradiation method to synthesize gold nanoplates has not been reported yet. In this project, a novel ultrasonic irradiation method is utilized to synthesize gold nanoplates, GNPs and Fe_3O_4 nanoparticles and to compare with conventional techniques. Furthermore, characterizing different properties of synthesized GNPs and gold nanoplates is a very important stage to look at the thermal property of GNPs and gold nanoplates in colloids in different concentrations.

To improve the effect of ultrasonic medical treatment and minimize its side-effect, a new concept, nanoparticle-mediated focused ultrasonic ablation (NFUA), has been proposed. The new concept relies on nanoparticles to focus on ultrasound energy and increase temperature locally and rapidly or increasing the cavitation effect. Ultrasound with nanomaterials would open a promising window to reach non-invasive ablation for both superficial and deep-seated tumors, whereas traditional methods are limited.

Due to the limitations of present RAF practice, a non-invasive concept is to introduce GNPs to targeting sites and expose them subsequently by a remote electromagnetic field to localise and enhance RF energy to produce required thermal injury. All previous studies in the field, i.e. Gardinal et al., 2008; Gannon et al., 2008; Glazer et al., 2011, have some limitations such as i) limited control of particle size, shape and functionlisation, ii) employing a fixed RF frequencies (13.56MHz) and iii) using commercial GNP dispersions where the impurities may be present, which may cause many artifacts. This work aims to address these limitations by controlled synthesis of GNPs with different morphologies and investing their heating response under different spectrums of electromagnetic fields. In short, it will

i) Synthesise gold nanomaterials and Fe_3O_4 nanoparticles with controlled size and shape.

ii) Investigate the interaction and bulk heating behavior of synthesised nanomaterials with an external heating source including ultrasonication, NIR-laser, EM at 200-400 kHz, 13.56 MHz and 2.45 GHz.

iii) Conduct in-vitro trials of the cellular uptake and biocompatibility of GNPs and GNPs mediated photothermal treatment *in vitro*.

The focus of the work is on the controlled synthesis of GNPs through sonochemical techniques to improve RF's specific absorption rate, and investigation of the interactions between EM field with nanoparticles, as well as related in-vitro studies. The results of in-vitro tests will be preliminary data for clinical trials, which would provide a reference for the selection of nanomaterials (i.e. size, shape, concentrations) for clinical trials and practices.

Chapter 3 Synthesis, purification and characterization of nanomaterials

Preparation of nanoparticles is an important process which contains synthesis, purification and characterisations of particles prior to further measuring and analysing their properties. Nanoparticles with controlled morphology in this study were synthesised by applying ultrasonication method to wet chemical reactions. The morphology of gold nanoparticles can be controlled by varying the reaction parameters, and also by applying DC voltages. Moreover, microcapsules were fabricated by the layer-by-layer technology and various shape of GNPs were applied in these capsules to make them photosensitive.

3.1 Nanomaterial characterisation techniques

The primary size and shape of all gold nanomaterials were identified by a transmission electron microscopy (TEM) and a scanning electron microscope (SEM) equipped with an Energy Dispersive X-ray spectroscope (EDX). In the operation, the TEM was performed with a Jeol JEM-2010 electron microscope at a bias voltage of 200 kV. The SEM was SEM-FEI-Inspect F at 10/20 KV accelerating voltage.

The size of nanoparticles and the size distribution was measured by a Zetasizer Nano-Z (Malvern Instruments Ltd, UK) with minimum 15 runs performed. Each result showed an average of three consequent measurements. The absorption spectrum of gold dispersion was measured by an UV/Vis spectrometer (PerkinElmer, lambda 35).

3.2 Synthesis of gold nanomaterials

Method A

Citrate reduction method as the control group: the citrate reduction (Frens, 1973) was used to produce the GNPs around 20 nm in diameters. 5.0×10^{-5} mole of $HAuCl_4$ in 190 ml of DI water was heated until boiling. Keep heating and stirring by magnetic blender, at the same time 10 ml of 0.5 (wt)% sodium citrate was added into the solution. The solution was kept stirring for the next 30 minutes. During the first 5 minutes, the colour of the solution was changed in the order of light yellow – clear – grey – purple–dark purple – wine-red. The size and shape of citrate reduction GNPs were identified by transmission electron microscopy.

The resulting suspension of citrate reduction GNPs presents a clear red colour, shown in Figure 3-1. The size of the GNPs was approximately 18 nm to 20 nm in diameters and the shape of GNPs is spherical. The concentration of original GNP dispersion was determined as 32 mg/L by atomic absorption technique.

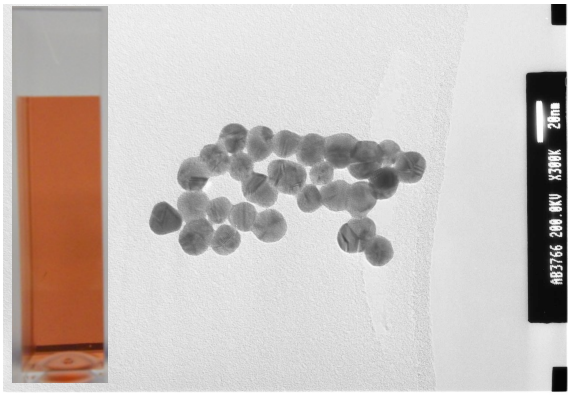

Figure 3-1 TEM image of citrate reduction GNPs

Method B

Citrate reduction with ultrasonic irradiation method: The same chemicals as the previous citrate reduction were used in this method. 5.0×10^{-5} mole of $HAuCl_4$ in 190 ml of DI water is heated until boiling. Keep heating and stirring by a magnetic blender, at the same time 10 ml of a solution of 0.5 (wt)% sodium citrate in DI water was added into the above solution until the colour of the solution changed to wine-red. To examine the influence of controlling factors, the solution with wine-red colour was further divided into 4 groups with different ultrasonic or stirring time:

- the solution was placed in the ultrasonic bath at 100^0C for 30 minutes;
- the solution was placed in the ultrasonic bath at 100^0C for 45 minutes;
- the solution was stirred and heated at 100^0C by magnetic blender for 10 minutes and then placed in the ultrasonic bath at 100^0C for 20 minutes;
- the solution was stirred and heated at 100^0C by magnetic blender for 20 minutes and then placed in the ultrasonic bath at 100^0C for 10 minutes.

Gold dispersions were purified by membrane dialysis method for 4-6 days where the residue reactants and stabilizer were diffused away.

There were five groups in this method: sonication for 0 minutes + stirring for 30 minutes (control group), sonication for 10 minutes + stirring for 20 minutes, sonication for 20 minutes + stirring for 10 minutes, sonication for 30 minutes, and sonication for 45 minutes. The size range is from 16 nm to 20 nm measured by Zetasizer (Figure 3-2). The results showed that increasing ultrasonic time can lead to smaller particles. TEM image (Figure 3-3a) shows that the GNPs sonicated for 10 minutes are bigger than those sonicated for 30 minutes and the shape are not very uniform. The size of the GNPs

sonicated for 20 minutes (Figure 3-3b) are smaller than GNPs only sonicated for 10 minutes but their shape is still not as regular as that sonicated for 30 minutes (Figure 3-3c). The GNPs sonicated for 45 minutes are even smaller and more uniform in shape, but the improvement gets smaller after 30 minutes of sonication.

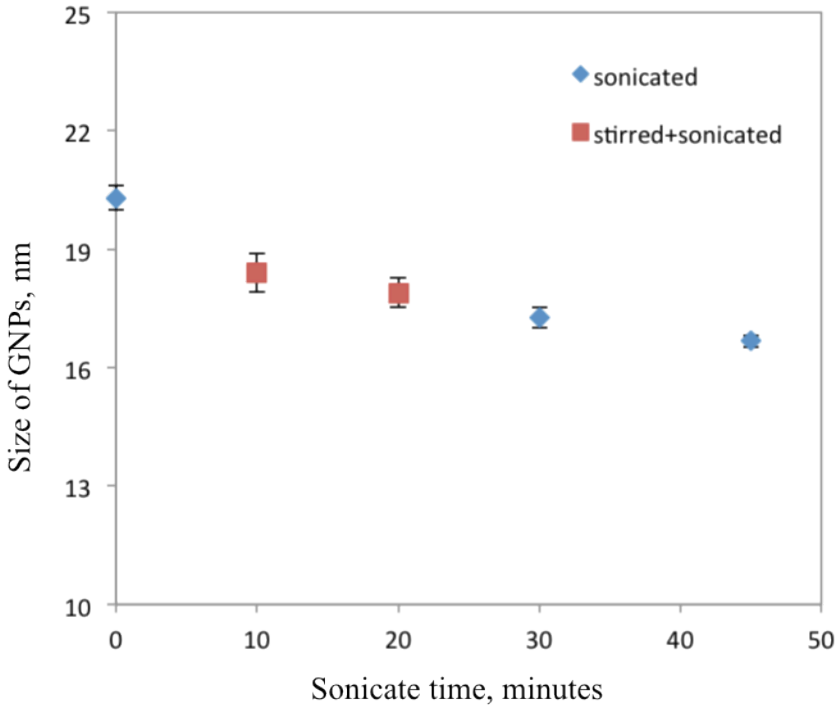

Figure 3-2 Average sizes of GNPs in DI water measured by a Zetasizer (blue points show the size of GNPs sonicated for 0, 30, and 45 minutes, and red points present the size of GNPs using a mixed magnetic stirring and ultrasonication of total 30 minutes).

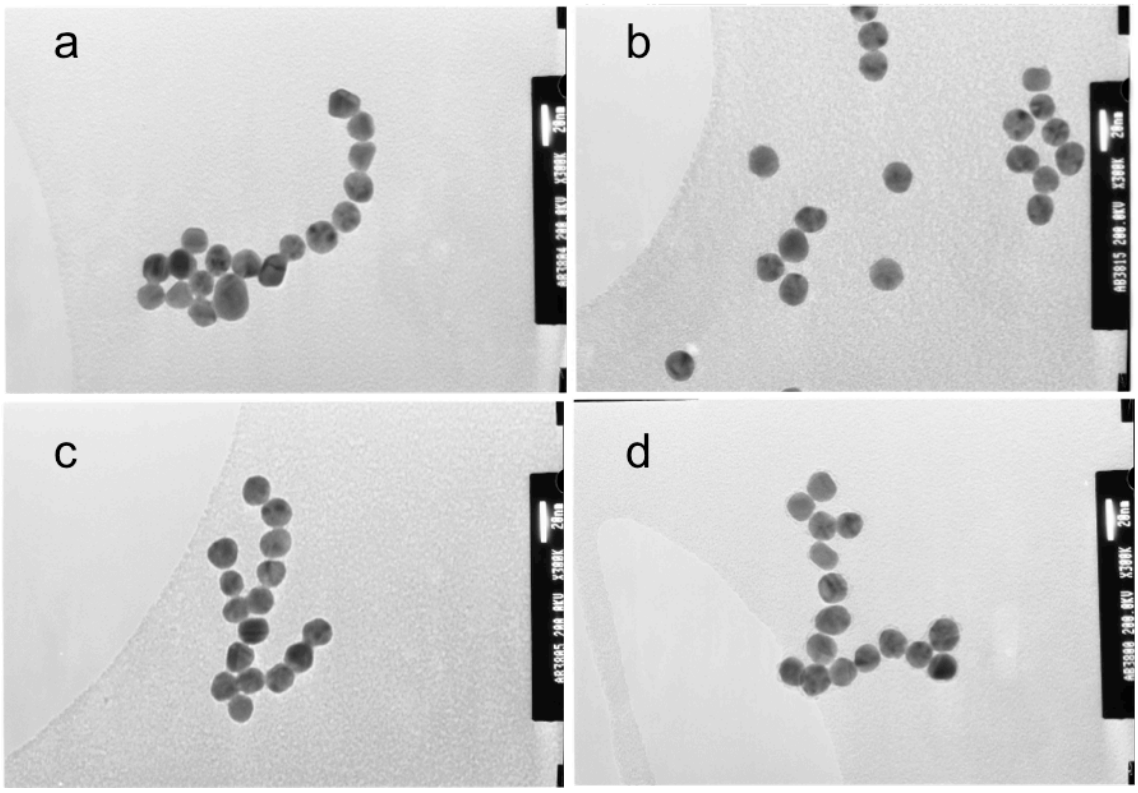

Figure 3-3 TEM image of GNPs with (a)10, (b)20, (c)30 and (d)45 minutes Ultrasonication

3.3 Gold nanofluids with plate-shaped particles

Method A

Synthesis of gold nanoplates through citrate reduction method at room temperature: the similar method as that of Huang et al. 2006 was used to synthesise gold nanoplates. Based on the citrate reduction method, 1.3 ml of 1% $HAuCl_4$ is added to 100 ml of DI water at 25^0C and then the solution was stirred by the magnetic blender for 1 minute. 0.4 ml of 38.8 mmol/L sodium citrate was added to the $HAuCl_4$ solution, after that the mixed solution was stirred for the next 30 minutes and then was exposed under natural light in the laboratory for 16 hours.

The resulting suspension of CR gold nanoplates is in cloudy brown colour. SEM image illustrates the main products of this method is in plate-like shape. In Figure 3-4, these

gold nanoplates are 220 nm-280 nm along their longest edge, revealing triangular and truncated triangular shapes with uniform edges. However, there are also some small gold nanoplates about 60 nm to 70 nm along their longest edge. The formation mechanism of citrate reduction gold nanoplates can be related to the kinetically preferred development of the redundant Au ions in the lateral direction of the small gold nuclei. Moreover, it should be pointed out that the temperature has an important effect on the reduction rate. At 25^0C, the reduction turns into substantially slow speed and changes to kinetic control that is appropriate for production of highly anisotropic structures. That is the reason why without additional capping agent or surfactant regular gold nanoplates can be fabricated by citrate reduction method. Furthermore, the existence of natural light is another important feature for formation gold nanoplates. It is difficult to process the reaction without the exposure of nature light, in spite of other reaction parameter being kept the same (Huang et al., 2006a).

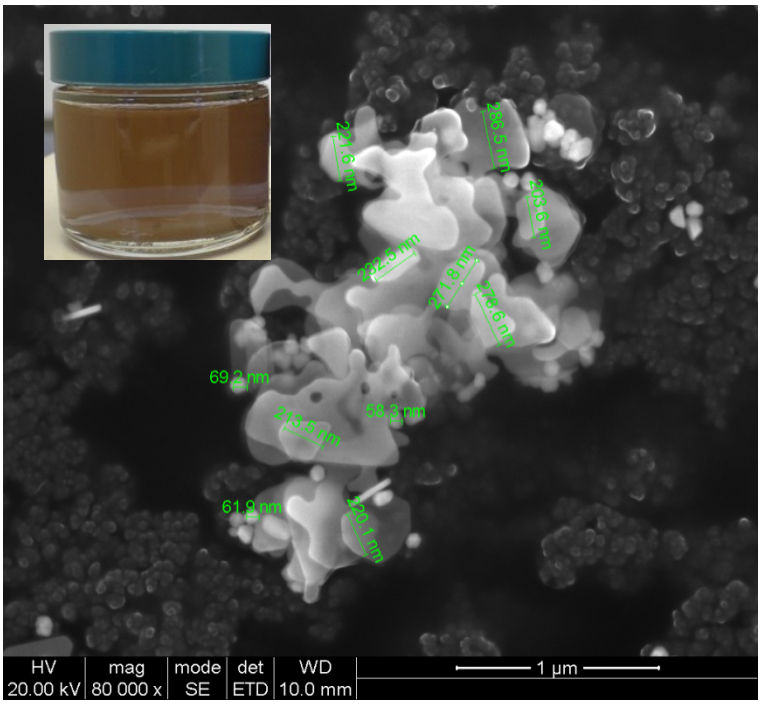

Figure 3-4 SEM image of CR gold nanoplates gold nanoplates; insert: resulting solution of CR gold nanoplates

Method B

Ultrasonic synthesis of gold nanoplates through citrate reduction method at room temperature: 1.3ml of 1% $HAuCl_4$ was added to 100 ml of DI water at room temperature and then the solution was sonicated for 1 minute. 0.4 ml of 38.8 mmol/L sodium citrate was added to the $HAuCl_4$ solution. After that, the mixed solution is divided into 5 groups with further ultrasonification time of 10, 20, 30, 45 and 60 minutes respectively. Following the ultrasonification, these mixed solutions were exposed under natural light in the laboratory for 16 hours. After 16 hours, the mixed solutions were in cloudy colour. The synthesized gold nanomaterials were separated by the centrifugation method, re-dispersed into DI water, and further purified through membrane filters for 4-6 days where the residue reactants and stabilizer were diffused away.

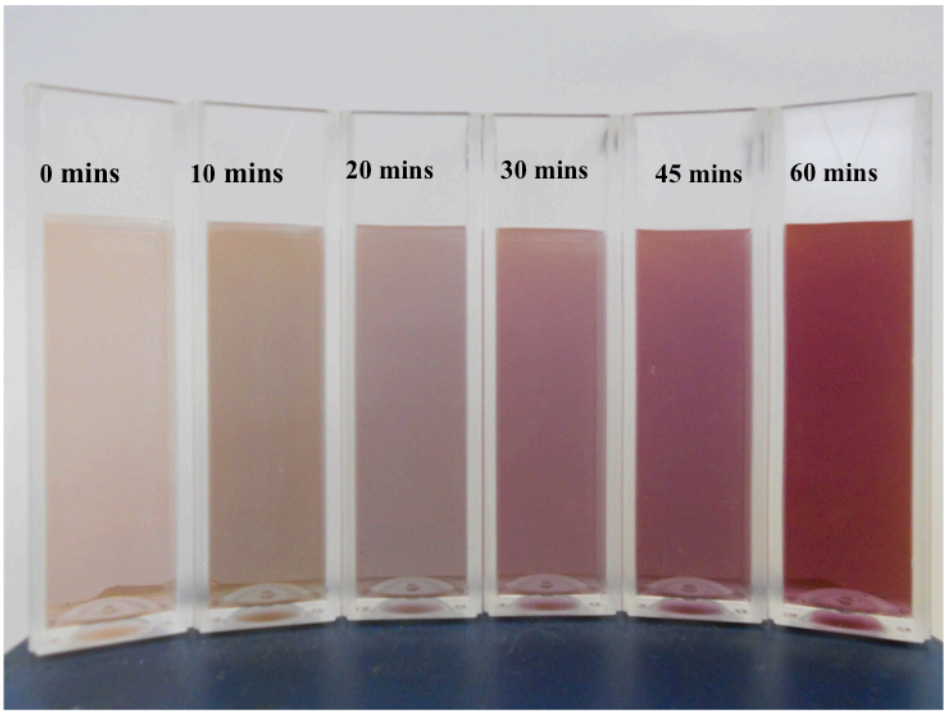

Figure 3-5 The colour of gold nanoplate suspensions sonicated for 0, 10, 20, 30, 45, 60 miuntes (left to right).

During the process, ultrasonic irradiation was the most important parameter in this work for determining the size and shape of gold nanoplates. The solution colours of gold nanoplates were different when the solutions were induced under ultrasonic irradiation for different duration. As can be seen from Figure 3-5, the color of suspensions is different due to the surface plasom resonance. Different size of gold nanoplates presents different color in their suspensions. It is demonstrated that the power of ultrasonic irradiation is strong enough to cause prompt reaction even just within 10 minutes.

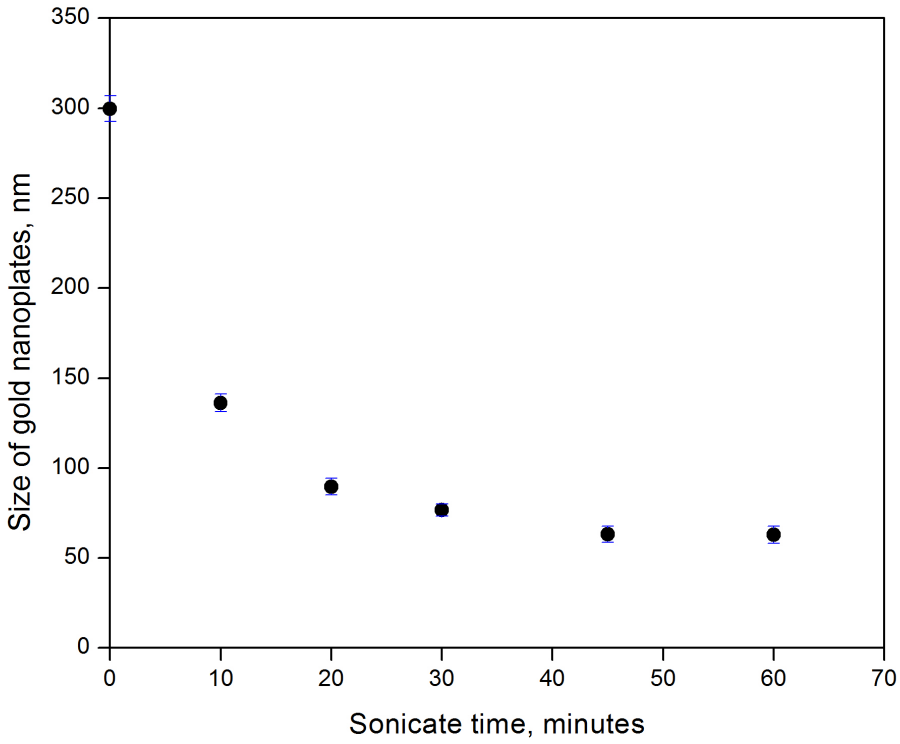

Figure 3-6 The average size of gold nanoplates in DI water sonicated for 0, 10, 20, 30, 45, and 60 minutes measured by a zetasizer.

Figure 3-6 presents that the size of gold nanoplates, measured by a zetasizer, have been decreased by the ultrasonic irradiation with the increased time. This also can be illustrated by SEM images of these gold nanoplates which are presented in Figure 3-7,

with the increasing sonicated times the size and shape of these gold nanoplates are smaller and more uniform and the main products exhibit in hexagonal shape. For example, from Figure 3-7 (a) and Figure 3-7 (d), the difference between these two synthesis progress is ultrasonic irradiation. In Figure 3-7(d) gold nanoplates is induced in ultrasonic irradiation for 30 minutes and this leads to the shape and size of gold nanoplates becoming near hexagonal shape and more uniform, compared with Figure 3-7 (a) without any ultrasonic irradiation.

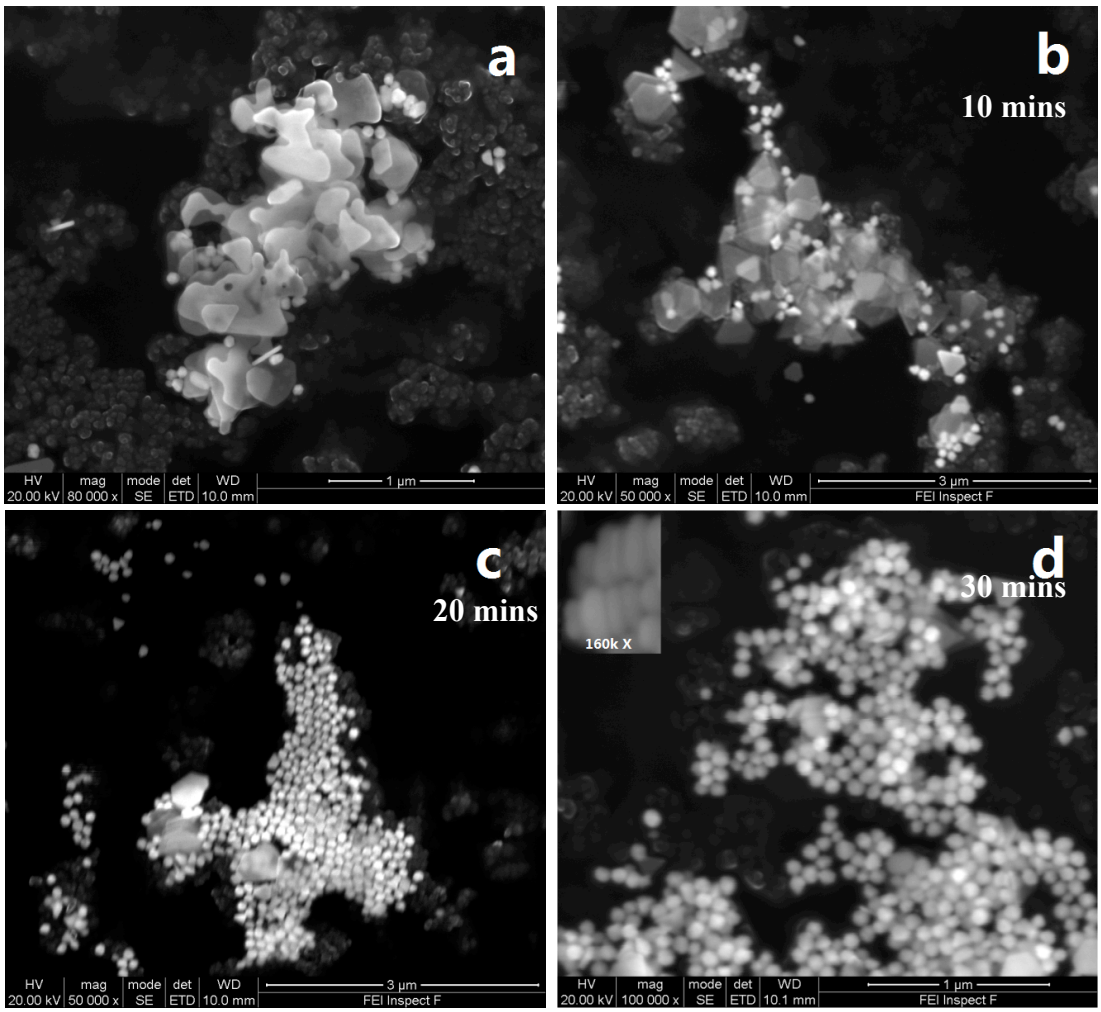

Figure 3-7 SEM images of gold nanoplates sonicated for 0 minutes (a), 10 minutes (b), 20minutes (c), 30minutes (d).d-inset shows the thickness of gold nanoplates sonicated for 30 minutes

Discussion of the GNP formation

By citrate reduction method, the size of GNPs can be controlled by the ratio of the reducing/stabilizing agents and gold (III) derivatives. In this work, 15 nm GNPs were produced by adding 0.5% (wt %) of sodium citrate, which acted as a reducing agent in the beginning and a stabilizer subsequently. Larger GNPs can be obtained by using a reduced amount of sodium citrate. At least 0.05% (wt %) of sodium citrate was required to reduce all gold (III) derivatives in this sample. Incomplete reaction occurred if the sodium citrate concentration was smaller than 0.05% (wt %). For concentrations below 0.5%, the amount of extra citrate ions was not sufficient to stabilize all GNPs, which result in the aggregation of small GNPs into bigger nanoparticles. As a consequence, a general trend of GNPs size reduction with the increase of sodium citrate was observed in the experiments, which is consistent with other studies (Daniel et al.2004). Properly controlling the ratio of sodium citrate to gold (III) derivatives, the GNP size can be engineered in the range of 10 ~ 150 nm.

The size of spherical GNPs can also be affected by ultrasonic irradiation. The average size of these spherical GNPs was about 18.2 nm with 10 minutes sonication, and 16.6 nm with 45 minutes sonication measured by Zetasizer. In addition, the ultrasonic irradiation has a significant effect on changing the morphology of gold nanoplates.

It has been demonstrated that the synthesis of anisotropic nanostructures in the liquid phase commonly involves two general methods: One is surfactant-based soft templates that can provoke the exclusive growth direction of the nanoparticles. The other one is selective adsorption of small molecules or polymers on specific crystal planes that can control the growth rate of the nanocrystals along a specific direction (Li et al., 2006b).

In this project, ultrasonic irradiation was employed to replace magnetic blender during the synthesis of spherical GNPs and gold nanoplates because it can generates strong pressure in collapsing cavities locally and immediately in the solution. Thus, the growth environment produced by ultrasonic irradiation was relatively stronger than by magnetic stirring, resulting in quasi-balanced growth of GNPs and gold nanoplates. Thus, the size and shape of GNPs (spherical) and nanoplates become smaller and more regular (Chen and Wen, 2011). Moreover, the formation of uniform gold nanostructures may be affected by different cavitation efficiency. The different ultrasound machine may generate different amounts, division, size, lifetime and dynamics of the bubbles, and thus different temperature and pressure within the collapsing cavitation. These different environments will affect the final results of synthesis of gold nanostructures (Okitsu et al., 2005).

The colour of synthesised GNPs and nanoplates originates from the surface plasma resonance (SPR). It is an optical phenomenon arising from the collective oscillation of conduction electrons, which is also responsible for the shining colour of metal colloids. SPR is a size-dependent phenomenon of GNPs (Steed and Atwood, 2009). This means that different size of gold colloids will present different colour. For example, the colour of 2 nm GNPs in toluene is dark purple, the colour of 15 nm spherical GNPs in DI water is wine-red, and that of the 90 nm GNPs in DI water is purple-red. The gold nanoplates with different size also exhibit different colour. Figure 3-5 shows gold nanoplates with different size ranging from 60 nm to 250 nm exhibit various colours. Comparing spherical GNPs with gold nanoplates with the same size of 90 nm, these two nanomaterials are unlike in colour, as shown in Figure 3-8. It suggested that surface plasma resonance of gold nanomaterials is not only size-dependent but also shape-

dependent. Orendorff's group has reported the investigation of the shape-dependent plasma resonance properties of GNPs (Orendorff et al., 2006).

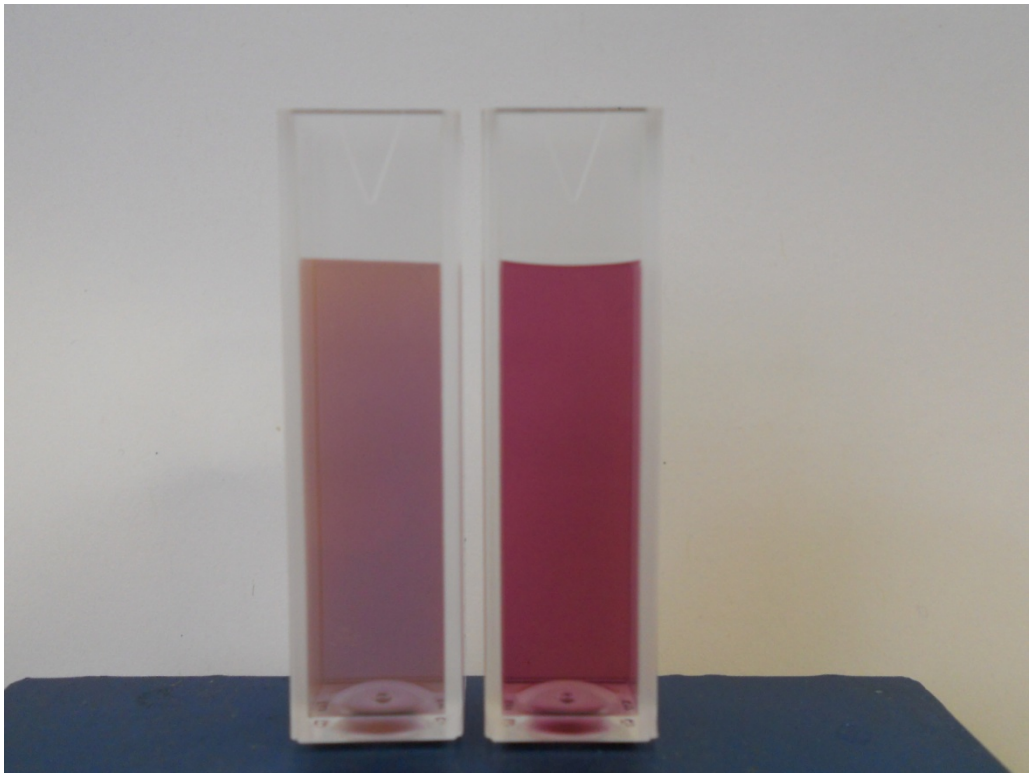

Figure 3-8 The colour of 90 nm gold nanoplates (left) and 90 nm GNPs (right)

3.4 Gold nanofluids purification

The separation and purification of samples following the wet chemical reactions are essential to elucidate the impurity effect. It has been suggested recently that the impurities presenting in GNP dispersions could be responsible for the fast heating rate (Li et al., 2011). Some impurities may also affect the viability of human cells and cause cytotoxicity (Balasubramanian et al., 2010). It will be difficult to clarify the nanoparticle effect without excluding this impurity effect. In this work, gold dispersions were purified by the membrane dialysis method for 4-6 days where the residue reactants were diffused away.

Atomic absorption spectrometer (Varian 220FS SpectrAA Atomic Absorption Spectrometer & GTA 110) was used to measure the concentration of gold dispersions. The measurement showed that the concentration of the purified GNP dispersion was determined as 32 mg/L, which was the same as that of the unpurified original GNP dispersion.

FTIR-ATR was also employed to evaluate the purity of GNP dispersions after dialysis. During the chemical synthesis of GNPs, some organic side-products were generated, together with unreacted precursors, presenting as impurities. Both of unpurified and purified GNP dispersions were concentrated under reduced pressure to yield a solid residue, which was then dried under 100 ^{o}C and subjected to attenuated total reflectance Fourier transfer infrared (ATR-FTIR) measurement. As can be seen from Figure 3-9, the GNPs sample without purification exhibit strong organic characters, while the one after dialysis shows almost no evidence of the existence of any organic species. It

proves that the process of dialysis reduces the amount of impurities to a negligible level (Chen and Wen, 2013).

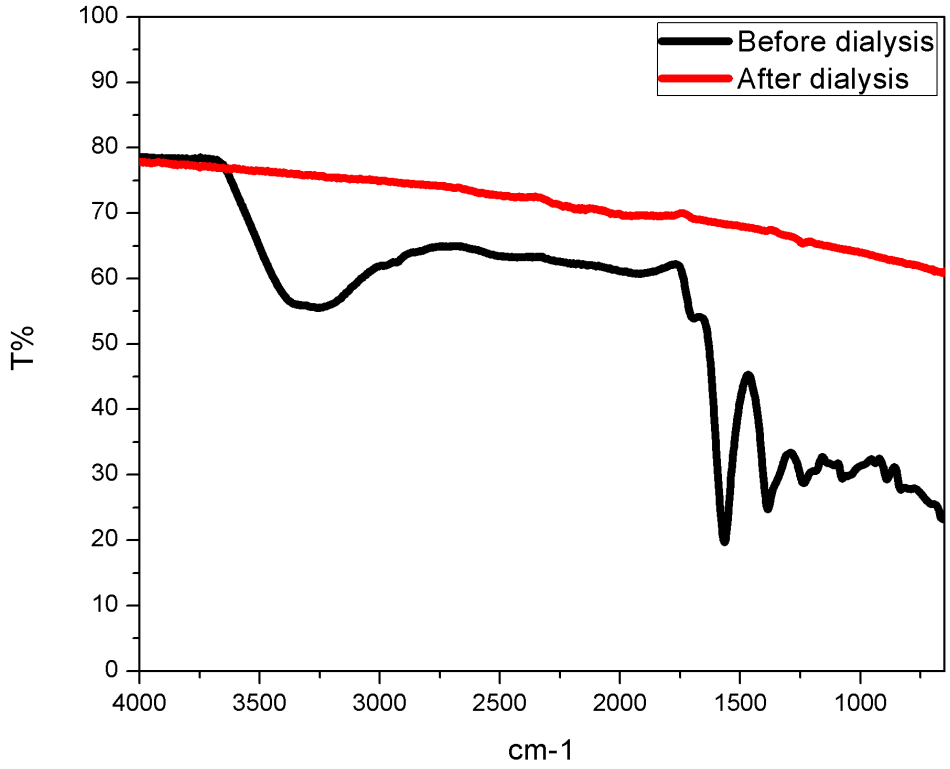

Figure 3-9 ATR-FTIR comparison of GNPs before and after dialysis

3.5 Control GNPs morphology through an DC field

5ml of gold nanosuspension contained 20 nm GNPs synthesized by citrate reduction method were applied voltage from 0 V to 90 V, shown in Figure 3-10**.** Two metallic electrodes were attached to a DC voltage source providing DC tuneable voltage from 0 to 90 V. A 1 cm insulator stick was connected to the bottom tips of the two electrodes to maintain the electric field strength steady when the voltage was applied.

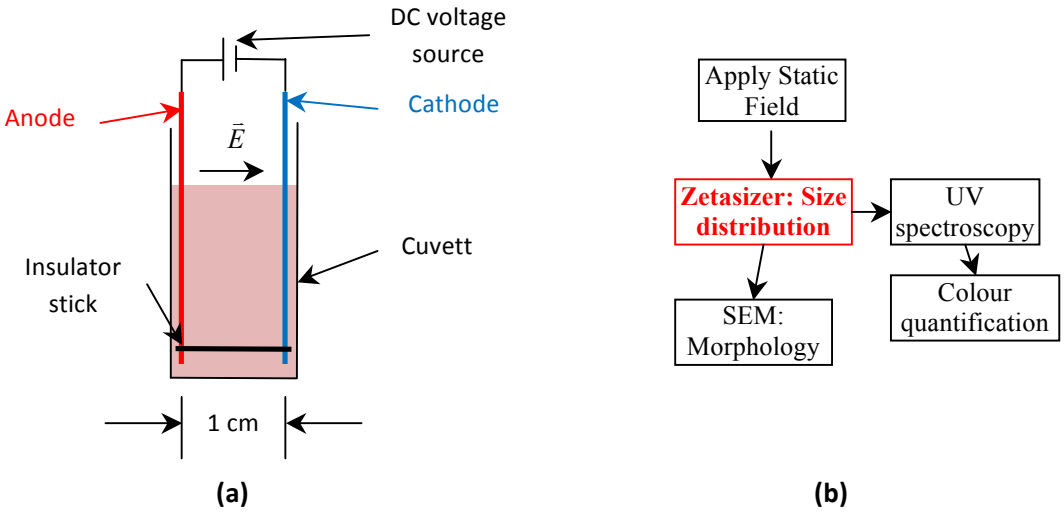

Figure 3-10 Experiment setup for DC electric filed induced effects study (a) Scheme of applying DC voltages to GNP dispersions; (b) investigation of morphology change after applying DC voltages

Figure 3-11(a) and (b) shows the colour of GNPs solutions just after applying 10-30 V voltage. From these pictures, remarkable colour difference can be observed. The colour of gold solutions is a simple way to detect the change of gold nanoparticle size. This phenomenon is related to SPR, when the size increases, the maximum absorption wavelength increases, resulting in the colour shifts. After 72 hours, the colour difference was still very obvious, but aggregations and precipitations can be seen, as shown in Figure 3-11 (c). The SEM images of these 3 samples are shown in Figure 3-12,

aggregation phenomenon can be observed in these images, which could not be focused very well because of the large variation in sample thickness.

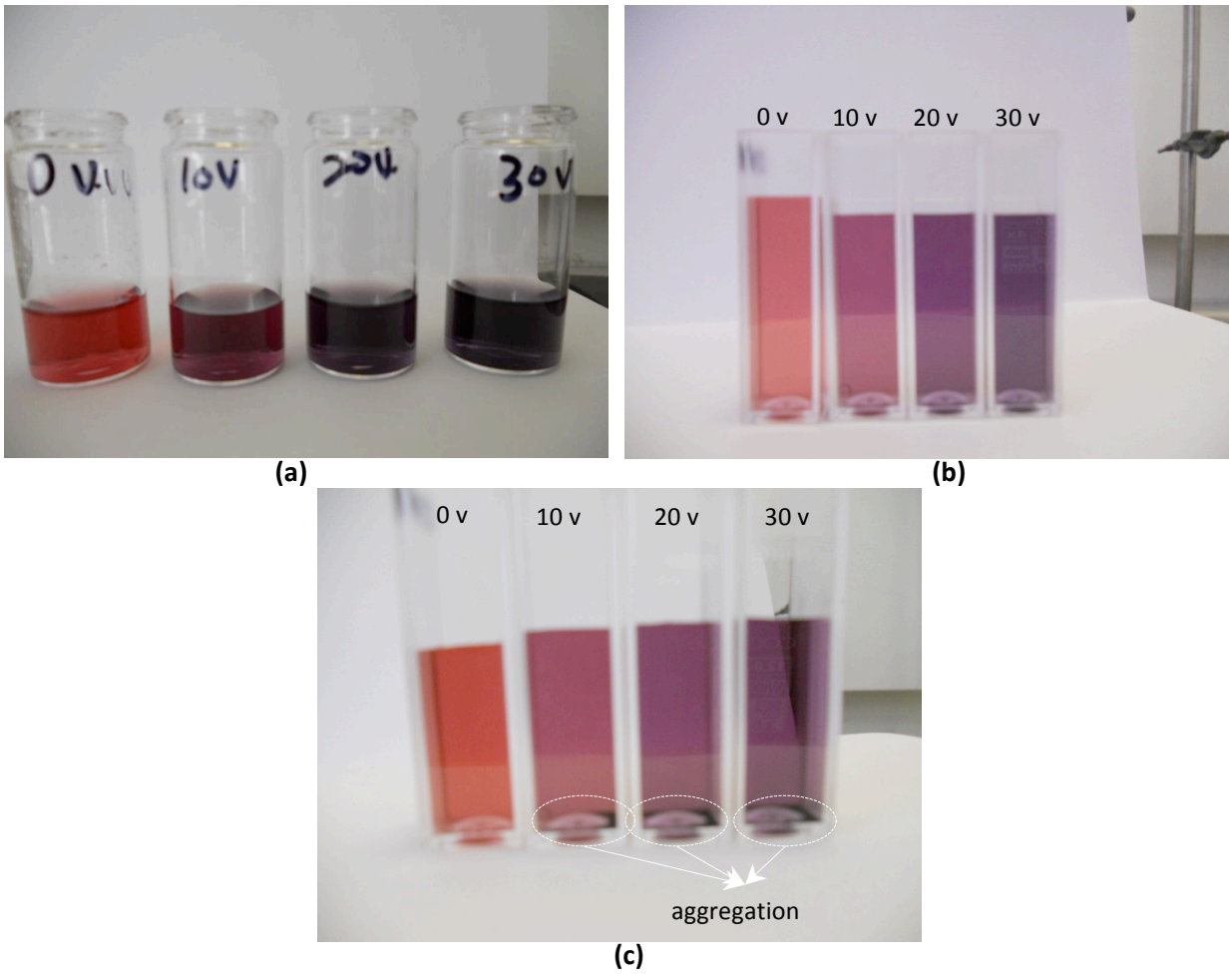

Figure 3-11 (a) and (b) colour change after applying 10-30V for 5 minutes; (c) 3 days later after the exposed to DC electric field.

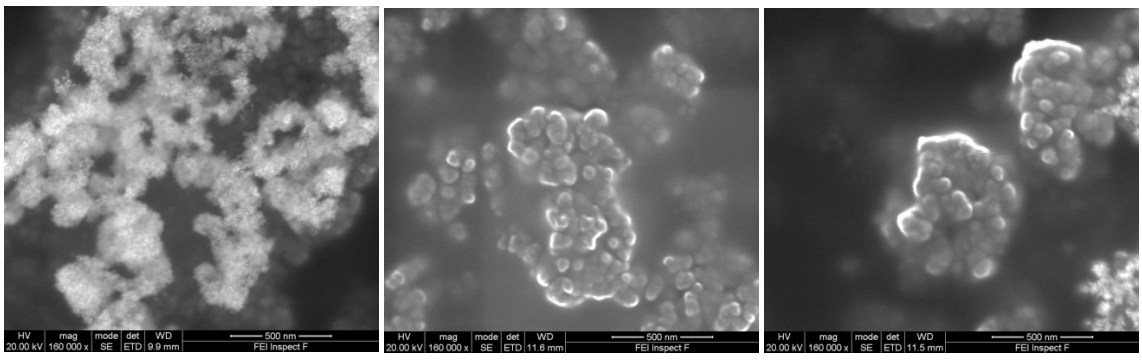

Figure 3-12 SEM images of GNPs applying (a) 10 V; (b) 20 V; (c) 30 V.

Higher voltages from 50 to 90 V were also applied for the same duration of 5 minutes. It was found that most of the GNPs aggregate after 5 minutes. Figure 3-13 shows the precipitation at the bottom of the cuvette. The samples were then sealed and left undisturbed for 24 hours. The upper supernatant layer became clear and more precipitation was observed. Zetasizer was used to identify if there is any GNPs left in the supernatant layer, and it shows that only some 10 nm GNPs are left in the supernatant layer, shown in Figure 3-14. But the concentration of 10 nm GNPs should be very small as the supernatant layer is almost colourless.

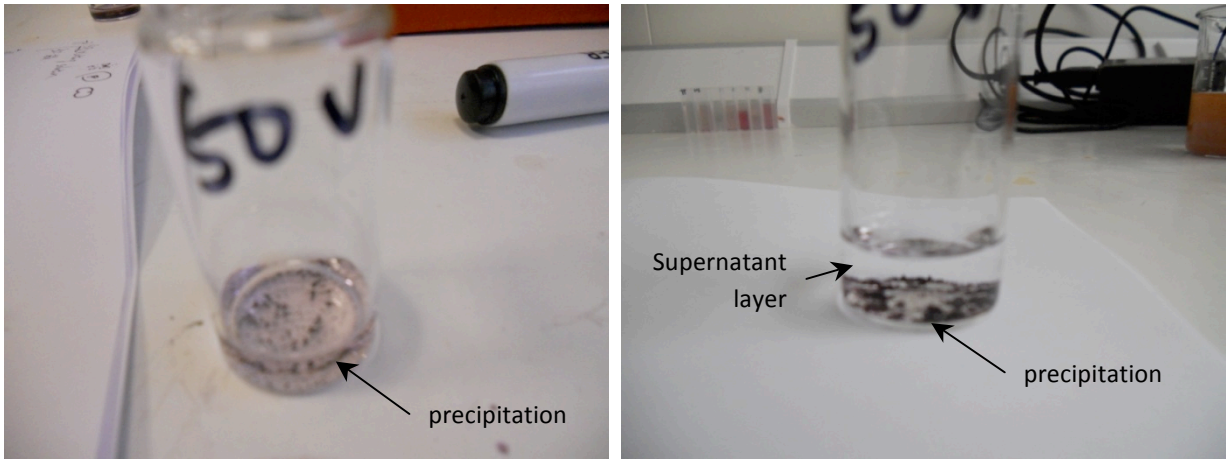

Figure 3-13 (a) 50 V voltage applied for 5 minutes; (b) 50 V voltage applied for 5 minutes, one day later

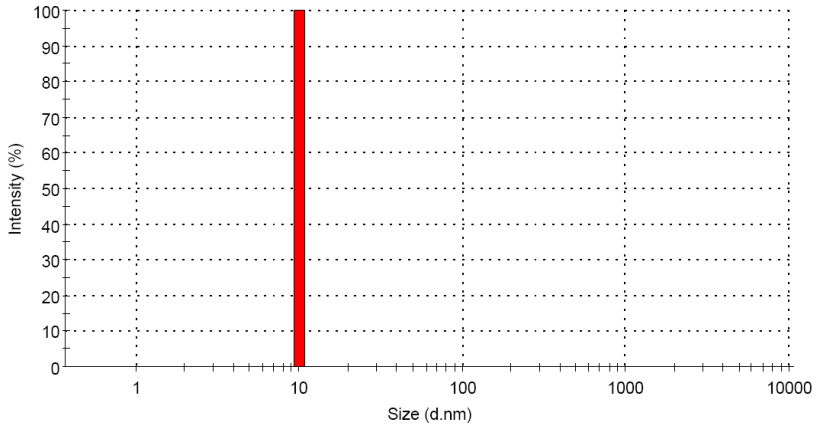

Figure 3-14 Size distribution of GNPs supernatant applied 50V for 5 minutes

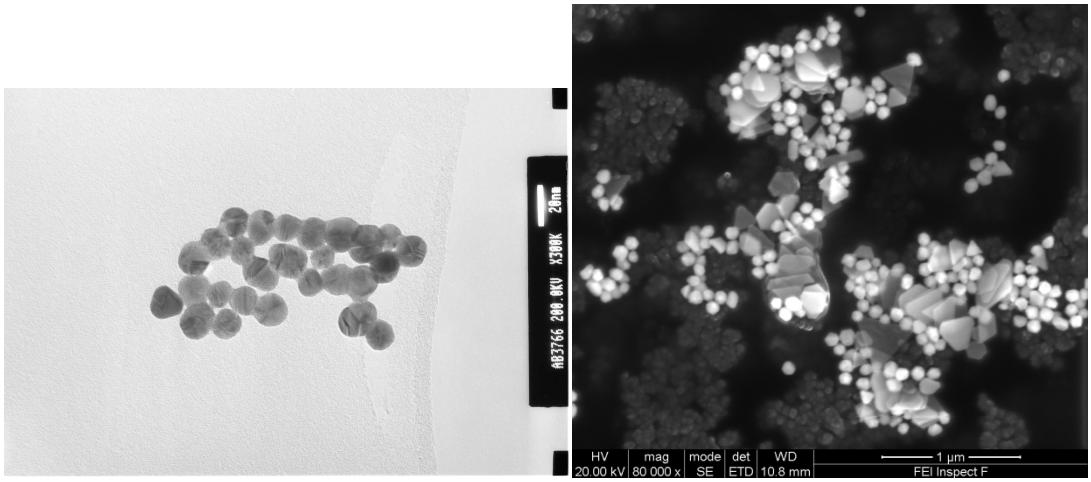

(a) (b)

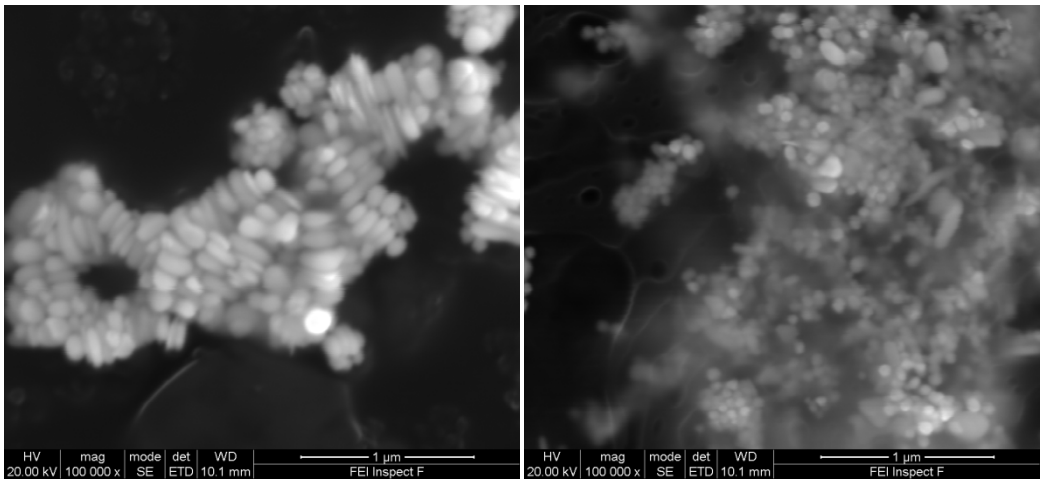

(c) (d)

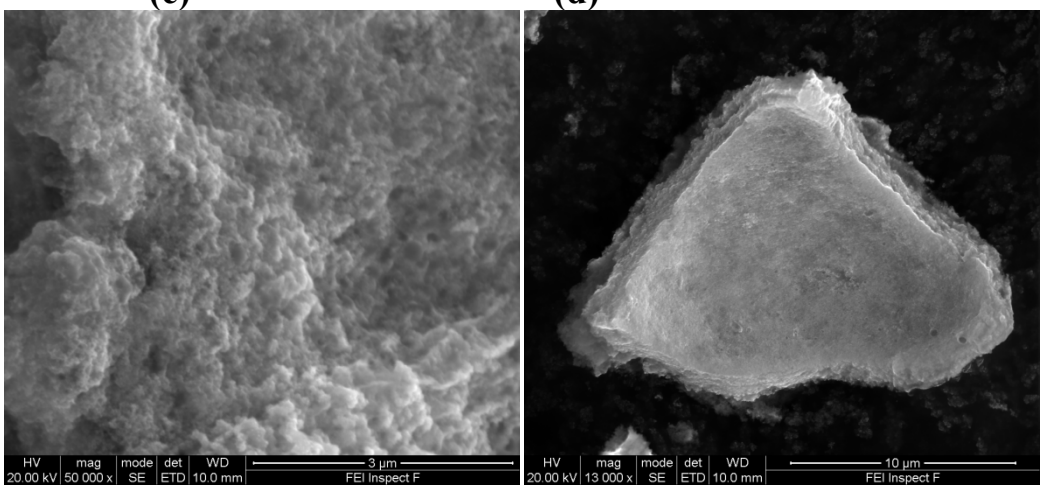

(e) (f)

Figure 3-15 SEM images of GNPs applied with different voltages: (a) 0V; (b) 50 V; (c) 60 V; (d) 70 V; (e) 80 V; (f) 90 V.

As can be seen from Figure 3-15, the morphology of formed GNPs can be controlled by applied voltage. GNPs become larger when the applied voltage is increased. Loose structures are formed at low voltage and large solid plate are formed at high voltages. It is clearly seen in Figure 3-15 (a) that particle size without applying voltage is around 20 nm. Particle size increases to at least 100 nm after applying 50 V, and some plates are formed with larger size (Figure 3-15(b)). Figure 3-15 (c) shows that GNPs clusters begin to form. Even bigger and denser structures are produced at higher voltages, as shown in in Figures (d), (e) and (f).

3.6 Study of colour shift of GNPs through an DC field

To study the colour shift process of GNPs induced by DC voltages, GNPs suspensions were firstly applied with a voltage of 5 V, under which the colour change was slow and easy to follow with increasing time of 0, 1, 3, 5 and 7 minutes. Then different voltages of 3, 7, 9, 11 V were applied for a fixed time of 3 minutes. GNP dispersions after applying DC voltages were measured by Zetasizer for size distribution, and by UV-visible spectrometer to identify the colour quantitatively. The CIE 1931 colour space was used to identify colour shift of voltage GNPs suspensions.

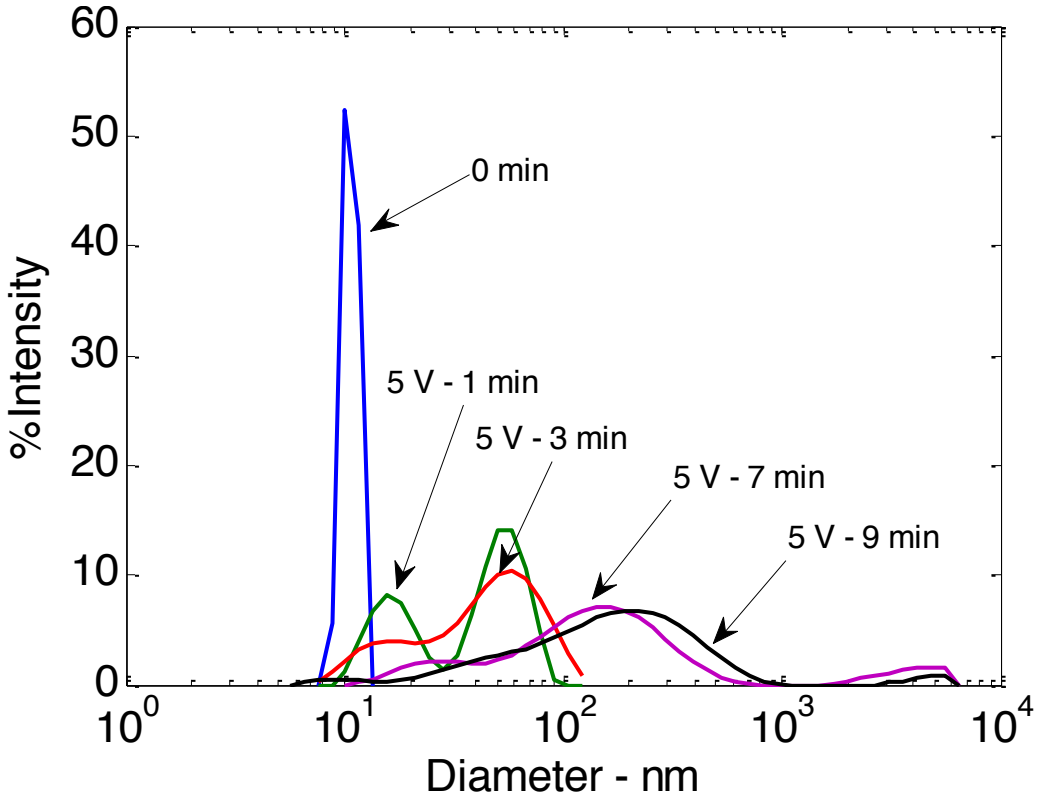

Figure 3-16 Size distribution of GNP dispersions after 5 V for 1, 3, 5, 7 and 9 minutes. The original sample (0 minutes) is a control group.

Figure 3-16 presents the size distribution of GNPs suspensions after applying 5 V with different time scale. The size of voltage GNPs increases with increasing duration when the voltage is fixed. When voltage at 5 V is applied for 1 minute, the size is increased to

around 40 nm in diameter. After 7 minutes, most of GNPs are bigger than 100 nm and some GNPs are even larger than 1000 nm in diameter.

Figure 3-17 shows the size distribution of GNP dispersions applyied with 3, 7, 9 and 11 V with the fixed time of 3 minutes. The size increases with increasing voltages, most of the particle size are bigger than 100 nm in diameter after applying varying voltages for 3 minutes.

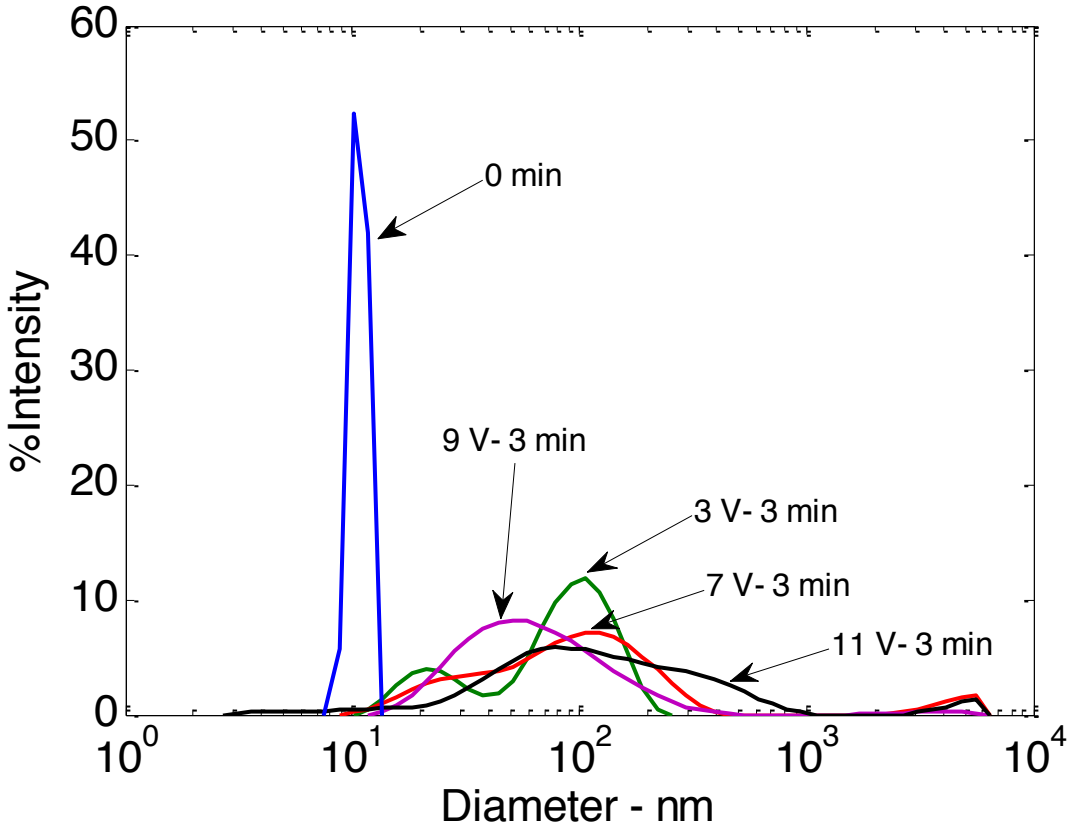

Figure 3-17 Size distribution of GNP dispersions after applying 3, 7, 9, 11 V for 3 minutes. The original sample (0 minutes) is a control group.

Figure 3-18 shows the SEM back-scattering imaging of GNPs after applying 11V for 3 minutes. GNP aggregations of sponge-like clusters are formed after applying DC voltage. Because the morphology of GNPs has been changed, the corresponding optical properties may be different from that of spherical GNPs without applying voltages.

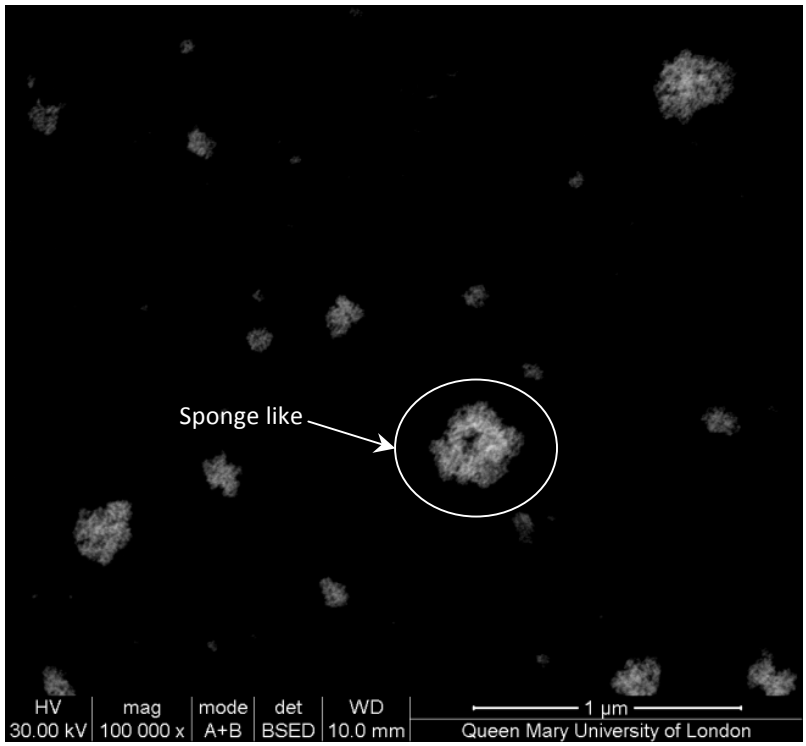

Figure 3-18 SEM imaging of GNP after applying 11V for 3 minutes.

Figure 3-19 (a) and (b) presents the UV-visible spectra of GNP dispersions applying fixed voltage (5 V) with varying time. The transmitance minimum (absorption peak) of gold dispersions at about 520 nm is red shifted with increasing durating of applied voltageas a result of increasing size of the GNP aggregations. 3-20 (a) and (b) shows the UV-visible spectra of GNP dispersions under different applied voltages with fixed time. The transmitance peak is also red shifted with increasing voltage.

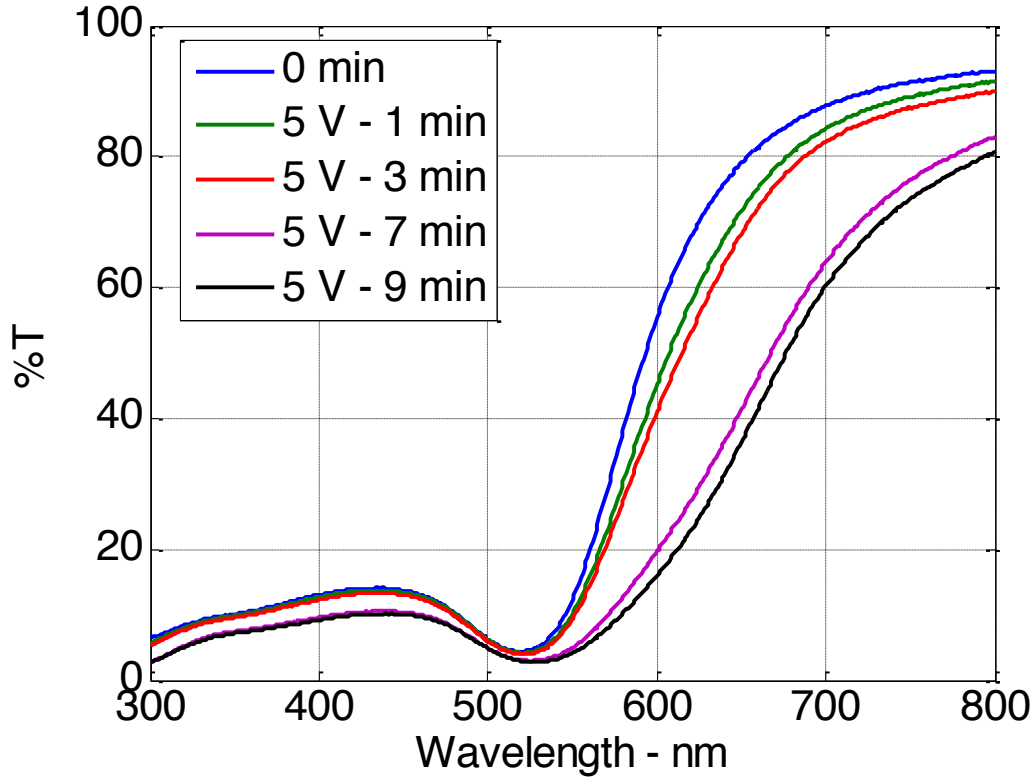

(a)

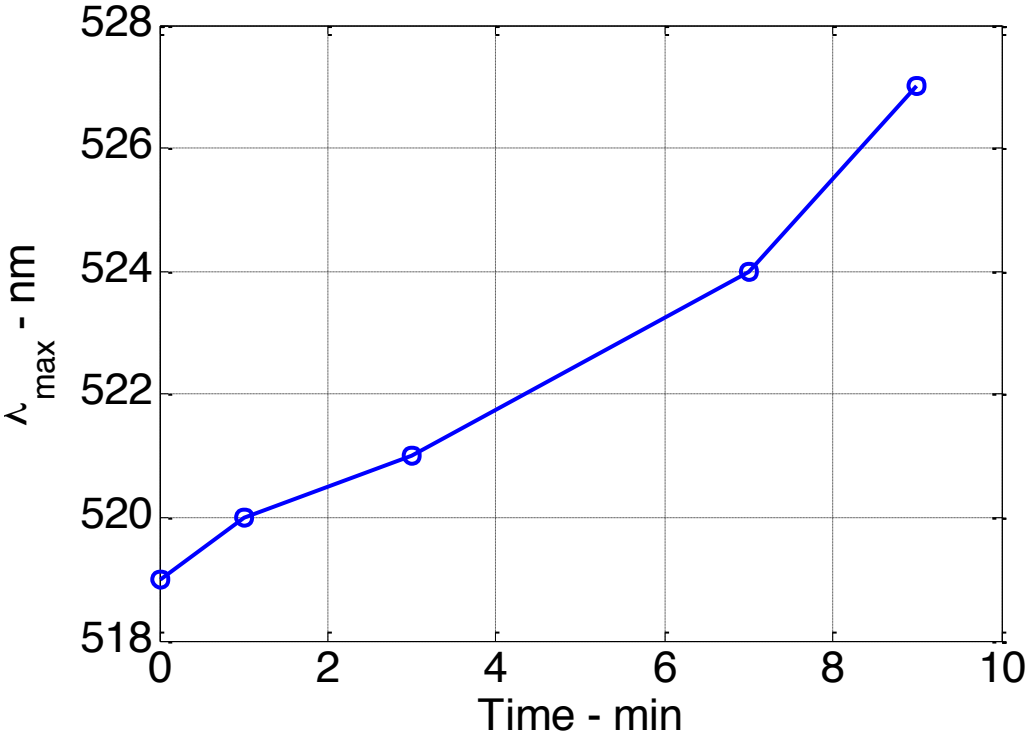

(b)

Figure 3-19(a) The UV-visible spectra of GNP dispersions with DC voltage applied for different time scales; (b) The absorption peaks at 519, 520, 521, 524, and 527 nm for the samples treated with 5 V DC voltage for 0, 1, 3, 7 and 9 minutes.

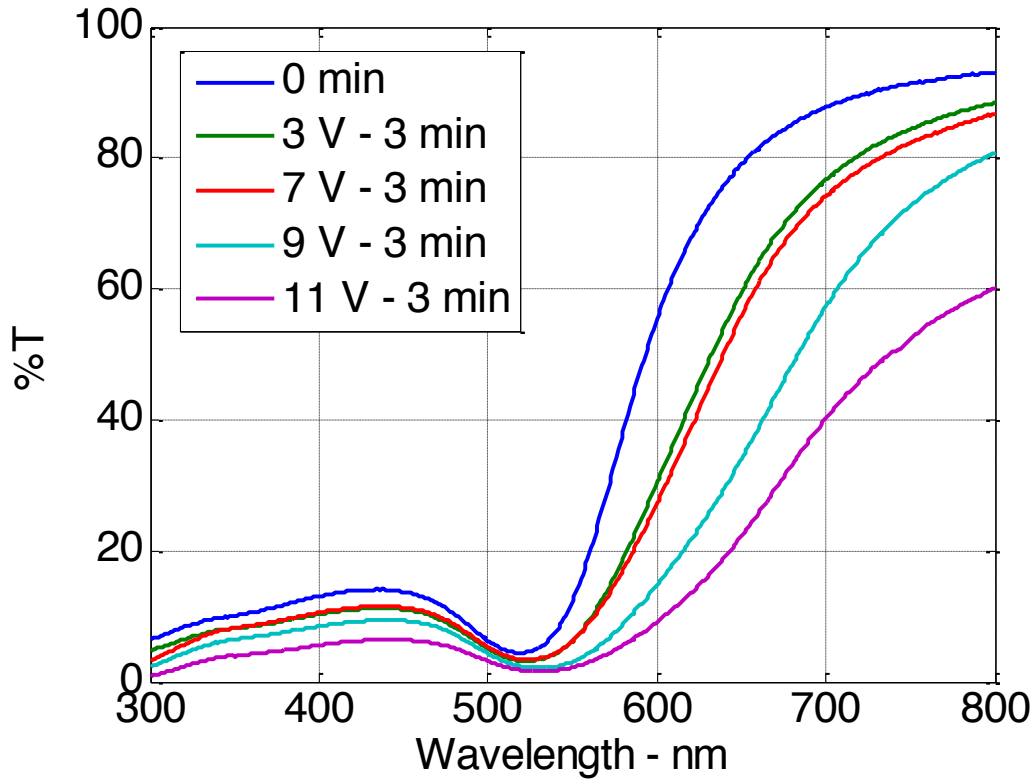

(a)

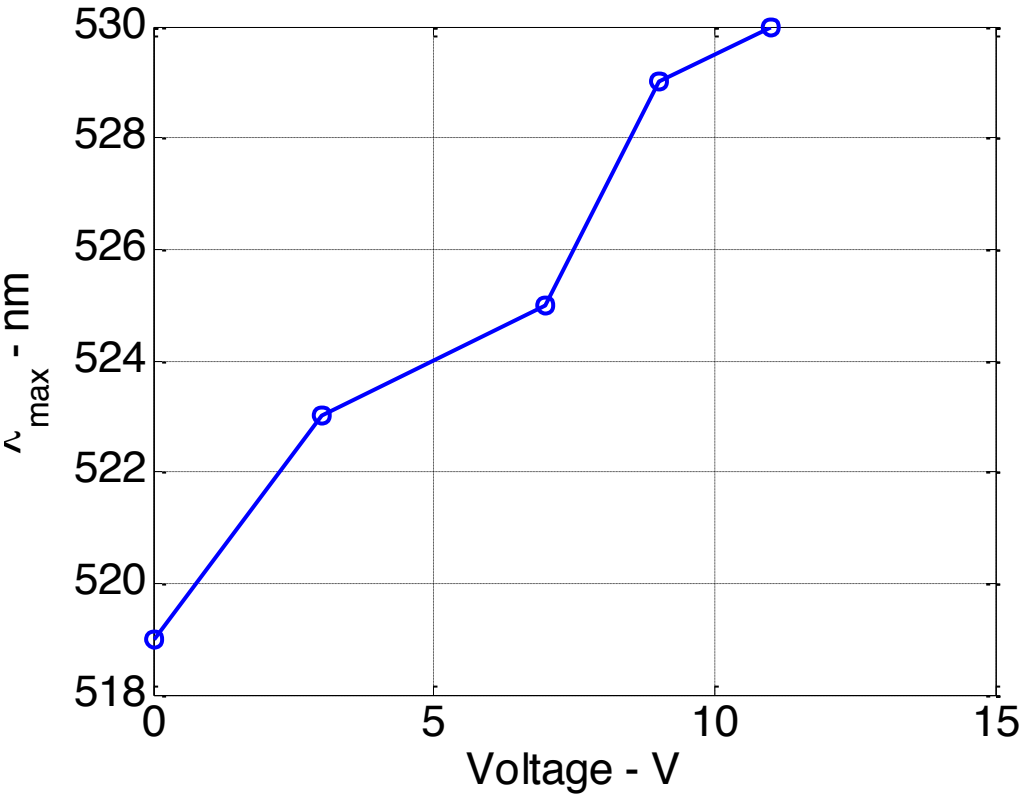

(b)

Figure 3-20 The UV-visible spectra of GNP dispersions with DC voltage applied for fixed time with varying voltage; (b) The absorption peaks at 519, 523, 525, 529, and 530 nm for the samples treated with 0, 1, 3, 7, 9, and 11 V DC voltage for 3 minutes.

Color study using the CIE chromaticity diagram

The *CIE1931* (International Commission on Illumination) colour space is a fundamental industry standard for colour description. The *CIE1931*-XYZ colour space is the first mathematically described colour spaces (Wyszecki and Stiles, 1982). It defines a colour quantitatively by two coordinates which is x and y on a two dimensional plane. Each dot on the colour space boundary presents a monochromatic light. The dot in the middle part presents a polychromatic light combined by mixing the three primary colours, whichare red, green and blue. Figure 3-21 illustrates the procedures of the colour studied by the CIE1931 colour space.

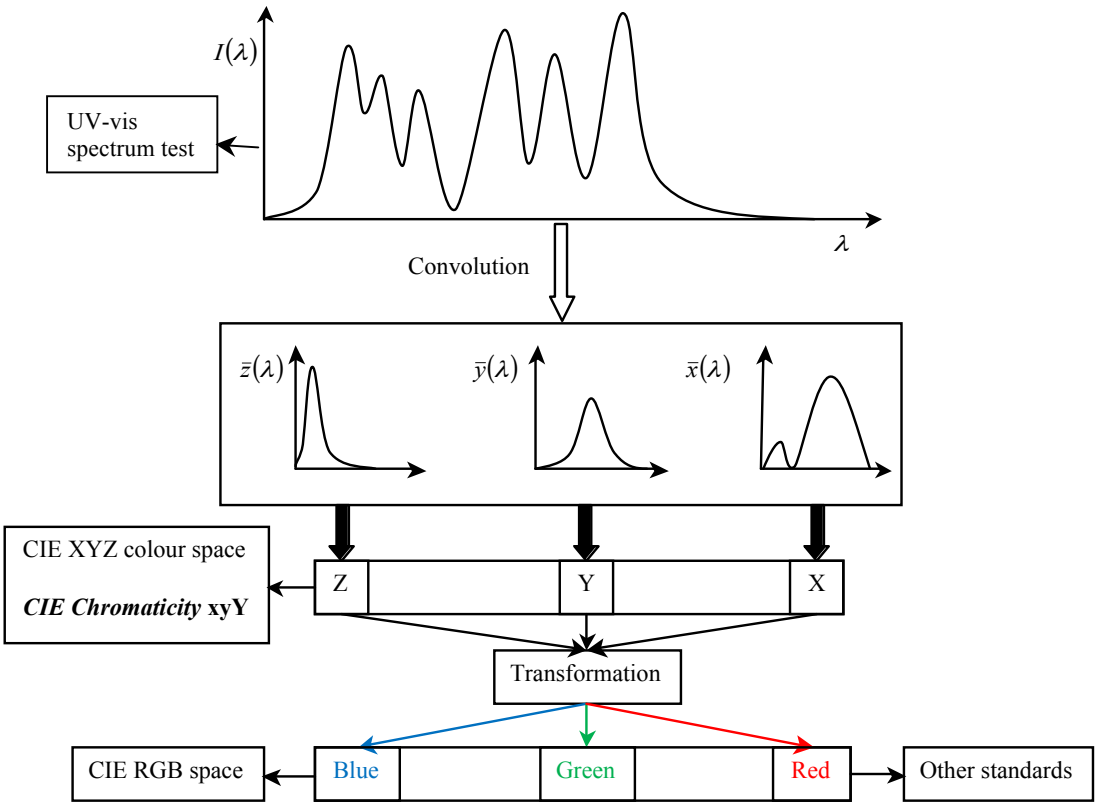

Figure 3-21 An overview of the CIE colour quantification. The UV-vis transmission spectral is convoluted by the colour matching functions to get the normalised values x, y, and Y, which are mapped to the CIE chromaticity diagram.

Human's retina has millions of colour-detecting nerves, which are categorised into rods and cones. Rods work as sensors detecting luminance or brightness and cones serve as colour measurement or chromaticity. Thus, the apparent colour may have the same chromaticity but in different brightness, or vice versa. A tristimulus measuring system are formed by three types of chromaticity, together with the brightness that is defined by the tristimulus values, X, Y, and Z. The tristimulus values of a colour with a spectral power density distribution $I(\lambda)$ are expressed by

$$\begin{cases} X = \int_0^\infty I(\lambda)\bar{x}(\lambda)d\lambda \\ Y = \int_0^\infty I(\lambda)\bar{y}(\lambda)d\lambda \\ Z = \int_0^\infty I(\lambda)\bar{z}(\lambda)d\lambda \end{cases} \quad (3\text{-}1)$$

In the *CIE1931*-xyY colour space, the Y parameter presents the brightness or luminance of a colour. The chromaticity of a colour is indicated by the two parameters x and y, given by normalised values. Hence, the CIE-xyY colour space can be formed from

$$\begin{cases} x = \dfrac{X}{X+Y+Z} \\ y = \dfrac{Y}{X+Y+Z} \\ z = \dfrac{Z}{X+Y+Z} = 1-x-y \end{cases} \quad (3\text{-}2)$$

Values of x, y obtained by normalisation of X, Y, Z can be located on the CIE chromaticity diagram to express the colour.

According to the UV-visible spectra of gold dispersion applied with 5 V and varying time, the x, y coordinates and the Y parameter are obtained, as shown in Figure 3-22. Both x and y reduce with the voltage duration. The Y component which represents the brightness, also reduce with the voltage duration. The results of GNP dispersions applied with varying voltages for 3 minutes are shown in Figure 3-24, and Figure 3-25 for the transmission spectra and the CIE chromaticity diagram, respectively.

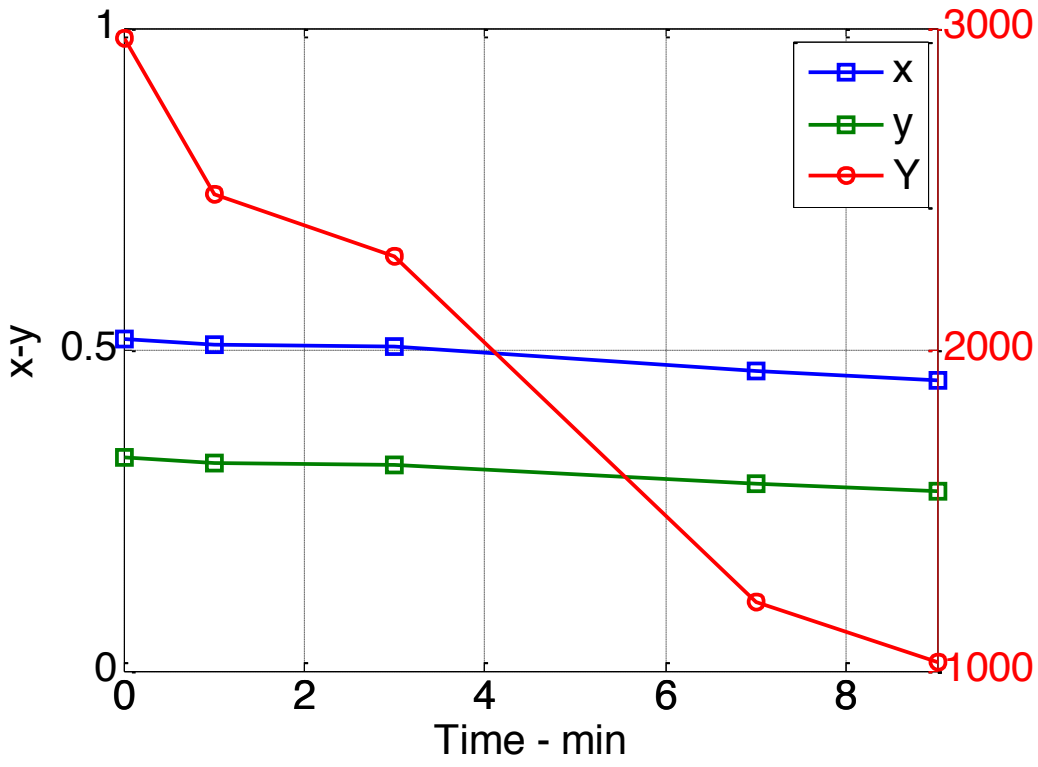

Figure 3-22 The variation of x, y and Y of GNP dispersions applied 5V for 1, 3, 7 and 9 minutes. The values of x and y present the chromaticity and Y is the brightness of a colour.

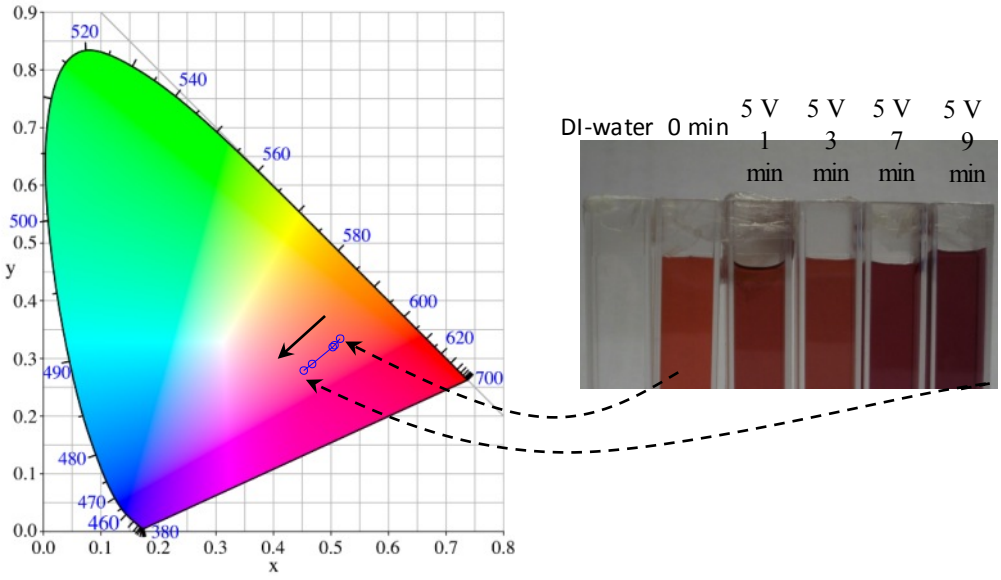

Figure 3－23 the *CIE1931*-xyY colour space of the colour of the GNP dispersions applied 5V for 1, 3, 7 and 9 minutes. The solid arrow in the diagram shows the direction of the shift of colour.

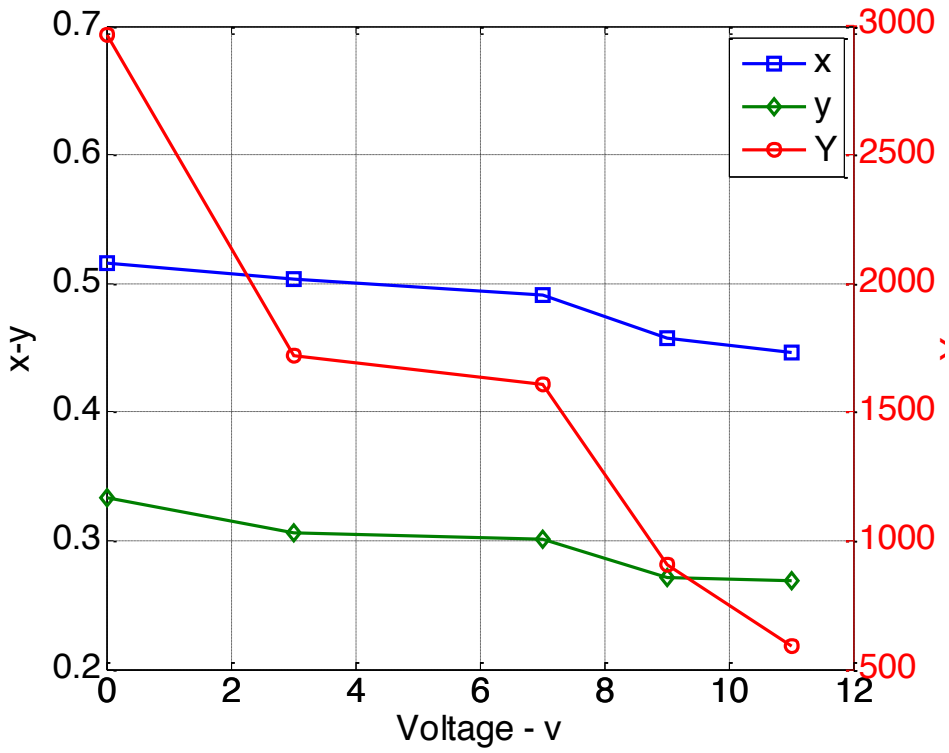

Figure 3-24 The variation of x, y and Y of GNP dispersions applied varying voltages for 3minutes. The values of x and y present the chromaticity and Y is the brightness of a colour.

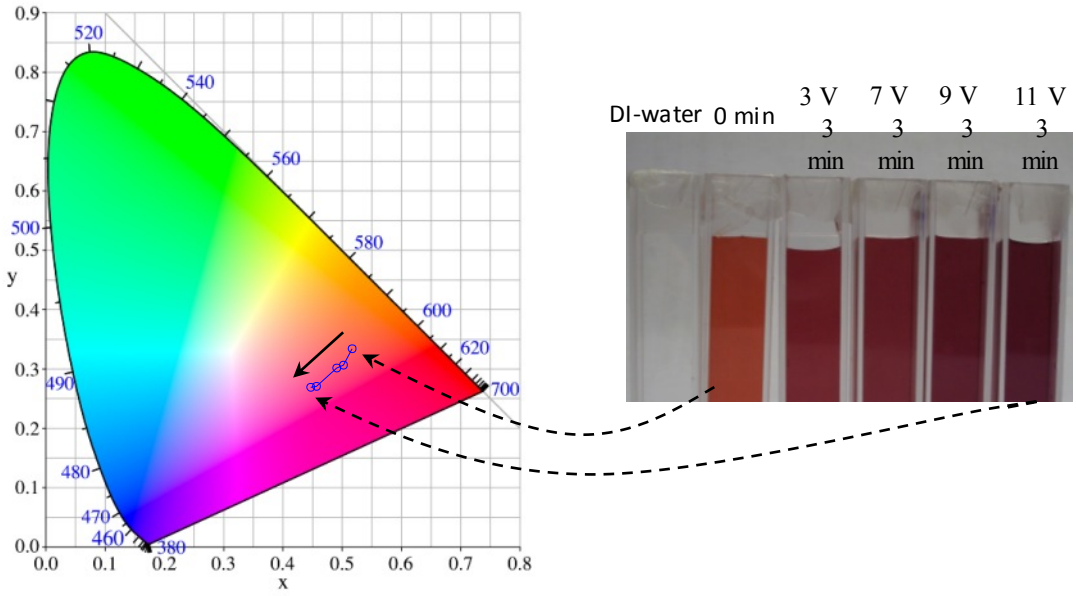

Figure 3-25 The *CIE1931*-xyY colour space of the colour of the GNP dispersions applied varying voltages for 3minutes. The solid arrow in the diagram shows the direction of the shift of colour.

The x and y coordinates are mapped to the CIE chromaticity diagram to present the colour change of GNP dispersions under the DC voltage treatment, as shown in Figure 3-23 and 3-25. The colour moves from the red region towards the blue region, specifying that the percentage of short-wavelength component is raised and the percentage of long-wavelength component is decreased. The value of Y represents the brightness of the colour. In this case, the value of Y decreases continuously because the transmission is lowered. This is reason why the sample applied with DC voltages is slightly darker than the original sample.

3.7 Synthesis Fe_3O_4 nanoparticles

Fe_3O_4 nanoparticles have caught great attention because they can be applied for disease diagnosis and cancer treatment in biomedical field owing to Fe_3O_4 nanoparticles processing high biocompatibility, chemical stability and injectability (Ghosh et al., 2011). Massart's co-precipitation method was used to fabricate Fe_3O_4 nanoparticles in this project because this preparation was carried out in an aqueous solution rather than organic solvents; the temperature can be easily controlled; and the reaction was fast with high yield (Lu et al., 2007). However, well-dispersed suspensions and uniform morphology of Fe_3O_4 nanoparticles are hard to achieve using the conventional method. Thus, a modified method (Massart's co-precipitation method with ultrasonic irradiation method) has been proposed by our group.

Conventional Massart's co-precipitation method of preparing Fe_3O_4 nanoparticles:
0.86 g of $FeCl_2$ and 2.35 g of $FeCl_3$ in 40 ml of DI water were heated to 80℃, and the solution is stirred with a magnetic blender. Then 5 ml of NH_4OH was added by a syringe. Keep heating and stirring for 30 minutes and then 1 g of citric acid in 2 ml DI water was added. The reaction temperature was increased to 95℃ and the heating and stirring were kept for 90 minutes. The whole reaction process was under the protection of argon to avoid air. The Fe_3O_4 nanoparticles suspension was purified by membrane dialysis for 3 days where residual reactants and stabilizer were diffused away.

Figure 3-26 presents Fe_3O_4 nanoparticles produced by Massart's co-precipitation methodthat has precipitated to the bottom of dialysis membrane. The aggregation of the magnetic Fe_3O_4 nanoparticlesis causes by the interaction with magnetic blander and stir bar during the dialysis process. After dialysis, the Fe_3O_4 nanoparticles were sonicated

for 5 minutes prior to the size measurement. As can be seen from Figure 3-27, the size range of Fe_3O_4 nanoparticles is quite wide from 60 nm to 400 nm and the average size of Fe_3O_4 nanoparticles is 150 nm measured by Zetasizer. In this case, Fe_3O_4 nanoparticles were produced under the magnetic equipment, resulting in particle aggregation and wide size-distribution of the magnetic Fe_3O_4.

Figure 3-26 Picture of Fe_3O_4 nanoparticles aggregation

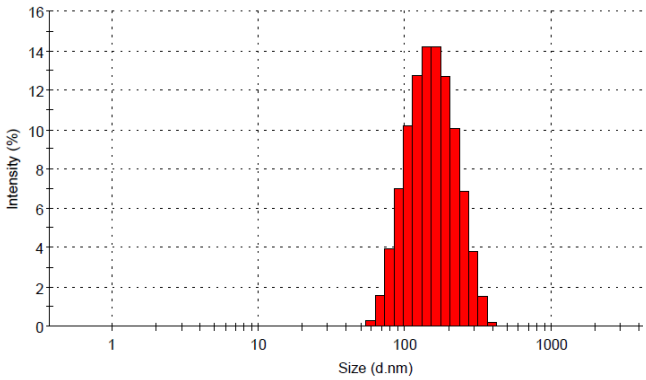

Figure 3-27 Average size of Fe_3O_4: 150 nm measured by Zetasizer.

Improved Massart's co-precipitation method with ultrasonic irradiation:

Based on the conventional Massart's co-precipitation method, only half amount of each precursor was used to produce Fe_3O_4 nanoparticles. 0.43 g of $FeCl_2$ and 1.18 g of $FeCl_3$ in 40 ml of DI water were sonicated and heated by ultrasonic bath with a temperature control system. 2.5 ml of NH_4OH was added by a syringe when the temperature increased to 70 °C. Keep heating and sonicating for 30 minutes and then 0.5 g of citric acid in 2 ml of DI water was added. The reaction temperature was increased to 95℃ and the heating and sonication were kept for 90 minutes. The whole reaction process was under the protection of argon to avoid air. The Fe_3O_4 nanoparticles suspension was purified by membrane dialysis for 3 days where the residual reactants and stabilizer were diffused away. Atomic absorption spectrometer (Varian 220FS SpectrAA Atomic Absorption Spectrometer & GTA 110) was used to measure the concentration of obtained Fe_3O_4 nanodispersions.

From both SEM and TEM images, the size of the Fe_3O_4 nanoparticles is approximately from 20 nm to 40 nm in diameter and the shape is spherical, as shown in Figure 3-28. Figure 3-29 shows that the size of Fe_3O_4 nanoparticles arranges from 20 nm to 100 nm measured by Zetasizer. The particle size measured by Zetasizer was larger than SEM result because the Zetasizer measured the hydrodynamic size of the particles, which was determined by the Brownian motion of particles. The concentration Fe_3O_4 nanoparticles suspension was 550 mg/L identified by the Atomic Absorption Spectrometry.

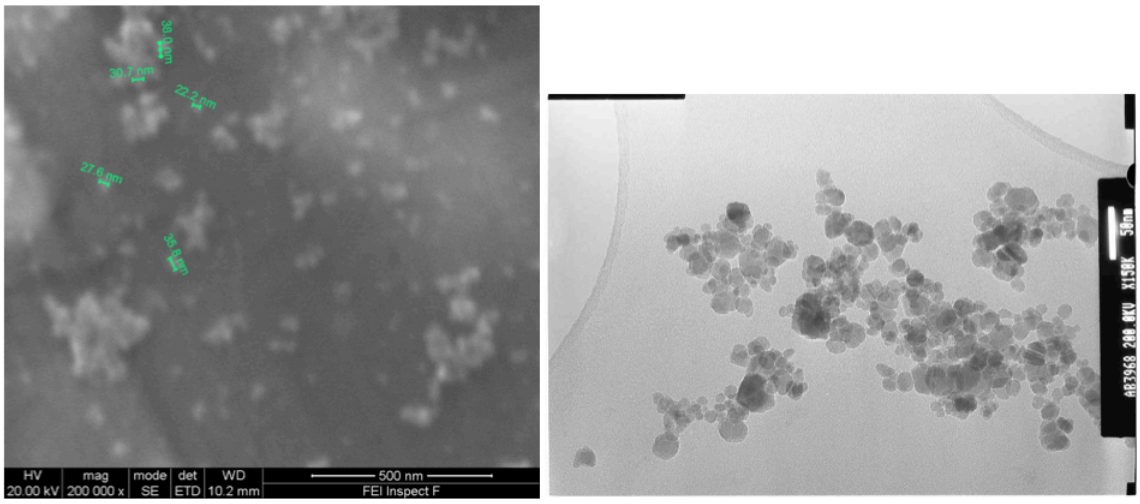

Figure 3-28 SEM image (left) and TEM image (right) of ultrasonic Fe_3O_4 nanoparticles

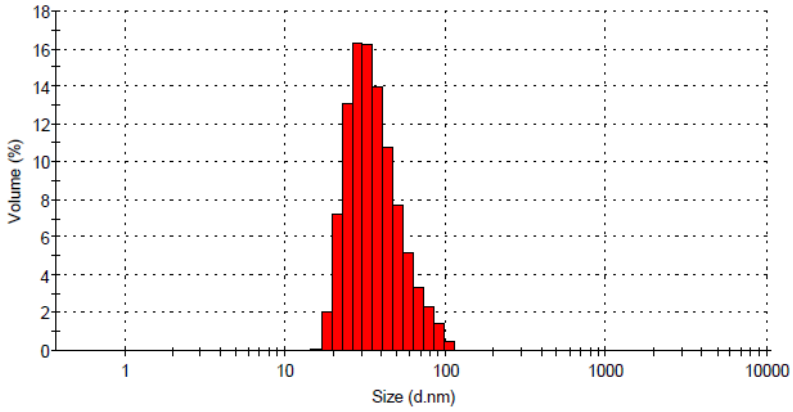

Figure 3-29 Average size of Fe_3O_4: 49 nm measured by nanosizer

3.8 Gold nanofluids with cage-shaped particles

3.8.1 Synthesis method

The synthesis of gold nanocages involved 2 steps. The first step was the synthesis of Ag nanocubes through reducing $AgNO_3$ with ethylene glycol (EG) in the presence of poly(vinyl pyrrolidone) (PVP) (Zhu et al., 2007). 6ml of EG solvent was heated to 150°C, and then 2 ml of 0.2 M $AgNO_3$ dissolved in EG was added. 2 ml of EG containing 0.1 g PVP (molecular weight = 10,000) was added dropwise within 3 minutes. The solution was stirred and heated for further 20 minutes. At last 20 ml acetone was added and the suspension was centrifuged to remove EG and PVP. Resulting Ag nanocubes were dispersed and stored in 4ml DI water.

The second step was the synthesis of Au nanocags by the galvanic replacement reaction. To 1ml of the Ag nanocube suspension wa added 50 ml of 1% PVP and the mixture was heated and sonicated at 80℃ for 10 minutes. 30 ml 0.1mM $HAuCl_4$ was injected dropwise to the Ag nanocage suspension, and then a saturated solution of NaCl was added to remove AgCl. Centrifugation was used to remove the impurities.

3.8.2 Results

Figure 3-30 shows the cage shape of nanoparticles, and the size of the particles with about 50 nm for edge lengths. The Ag nanocubes were used as the template for galvanic replacement to make gold nanocages with controlled size. Poly(vinyl pyrrolidone) (PVP) was utilized during the synthesis of Ag nanocubes to direct the growth of the {100} facets (Sun and Xia, 2003). Galvanic replacement was used because there are different electrochemical potentials between Ag and Au. Ag is oxidised into the solution as ions when Au is being adhered to the outer surface of the

cube. The reaction keeps going on, more and more Ag from the interior of the cube will be taken away from a small pit in the cubic wall, shaping a hollow Au-Ag alloyed nanobox. By adjusting the amount of $HAuCl_4$ added, the wall thickness can be controlled. A highly porous cage-structure is formed as the Ag is removed by $HAuCl_4$ from the Au-Ag alloy walls at a later stage of the reaction (Sun and Xia, 2004). The absorption peaks of cages can be easily tuned all the way from 400 nm to 1200 nm, and wide absorption cross sections are achieved in the important bio-friendly window of near-IR region. Gold nanocages are different from spherical and plate-shaped GNPs in that the absorption peak of nanocages is closer to the near-IR region.

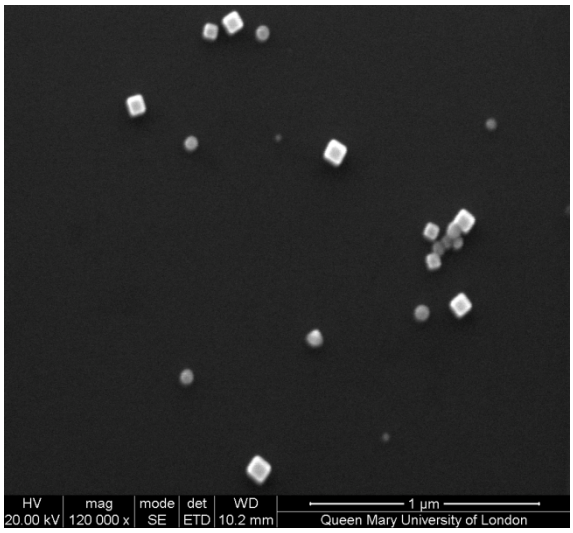

Figure 3-30 SEM image of gold nanocages

Figure 3-31 presents that the main peak of gold nanocages is at 670 nm and the absorption band is broad in range of 600-700 nm. Figure 3-32 shows the UV absorption peak of GNPs and gold nanoplates are at 520 and 576 nm. In this case, gold nanostructures can strongly absorb the light at a resonance wavelength depending on the size and shape of the nanostructures. Controlling the morphology is able to tune the absorption peaks of gold nanomaterials. The SPR of spherical shape GNPs can be

turned from 510 to 650 nm when the size of GNPs is changed from 2 to 150 nm (Daniel and Astruc, 2004). Gold nanoplates and gold nanocages have been investigated to shift the SPR peaks to the near-IR region (Pelaz et al., 2012, Skrabalak et al., 2007a). Nanomaterials absorbing in the near-IR region can be used as transducers to alter near-IR irradiation into heat, opening a new window for cancer treatment via the photothermal effect.

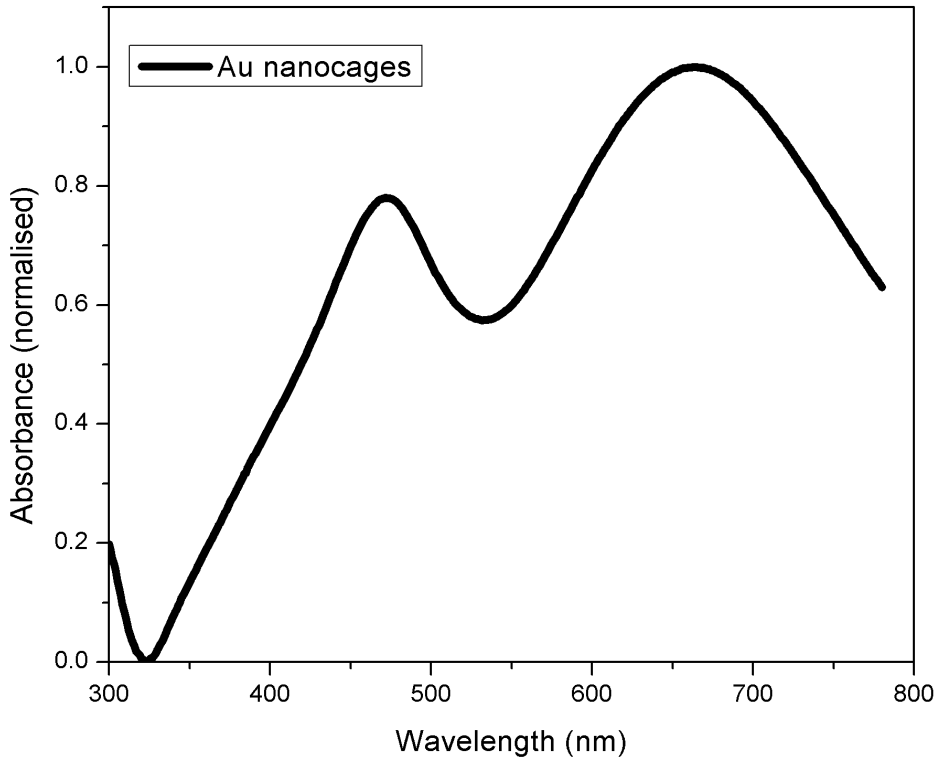

Figure 3-31 Shape effect of Au nanomaterials exposed under laser irradiation at 655 nm for 10 mins

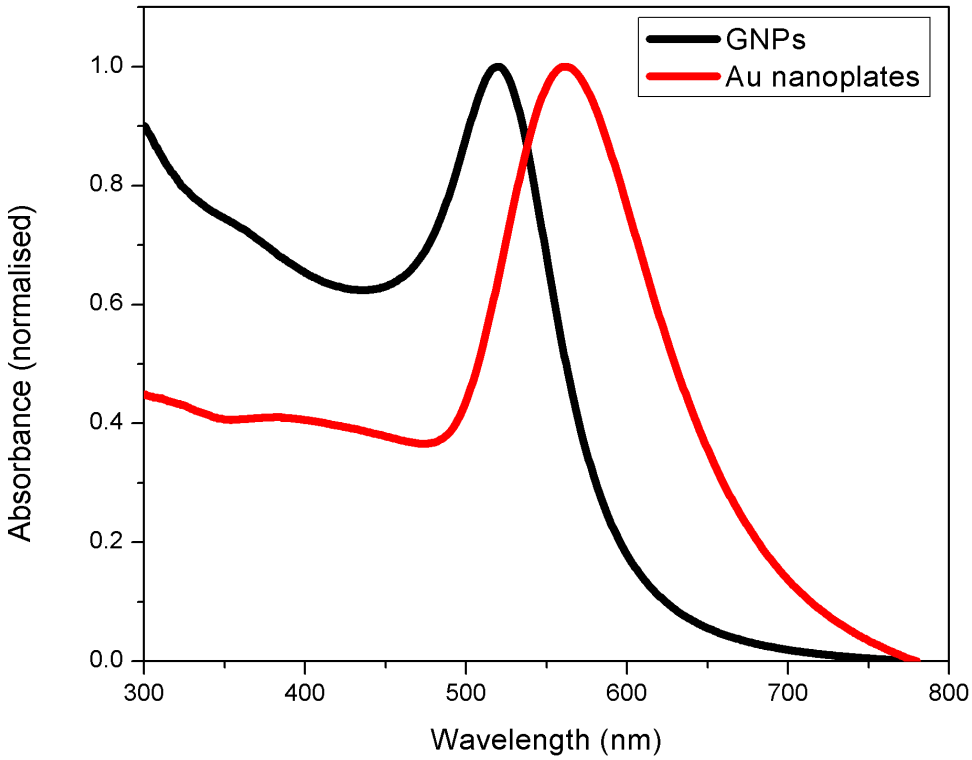

Figure 3-32 UV–Vis absorption spectra of GNPs and gold nanoplates

3.9 Microcapsules with 1D, 2D and 3D Au nanomaterials

3.9.1 Microcapsule fabrication method

The microcapsules were made through the layer-by-layer technology. The cores of microcapsules are $CaCO_3$, which was the reaction product of Na_2CO_3 and $CaCl_2$. Poly(allylamine hydrochloride) (PAH, molecular weight: 56 000) and poly(sodium 4-styrenesulfonate) (PSS, molecular weight: 70 000) were used to form the shells of microcapsules. Every capsule had an 8-layers shell, and Au nanomaterials were embedded between the 4^{th} ~ 5^{th} layers and between the 6^{th}~ 7^{th} layers. The shells were stained red by tetramethylrhodamine-5-(and 6)-isothiocyanate (TRITC) for confocal imaging.

Three different shapes of Au materials, including spheres, plates and cages, are embedded in the microcapsule layers (walls) to introduce photosensitivity to laser radiation (Figure 3-33 to Figure 3-35).

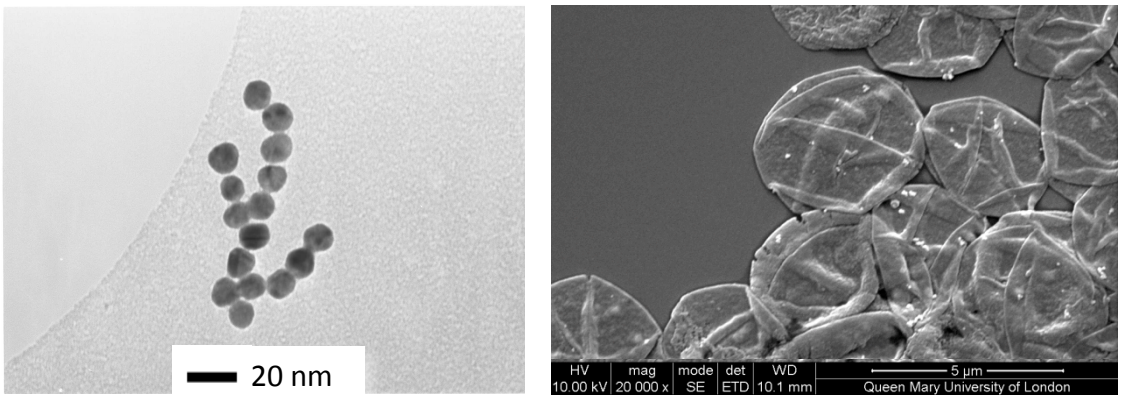

Figure 3-33 TEM image of GNPs (a) and SEM image of microcapsules with GNPs (b)

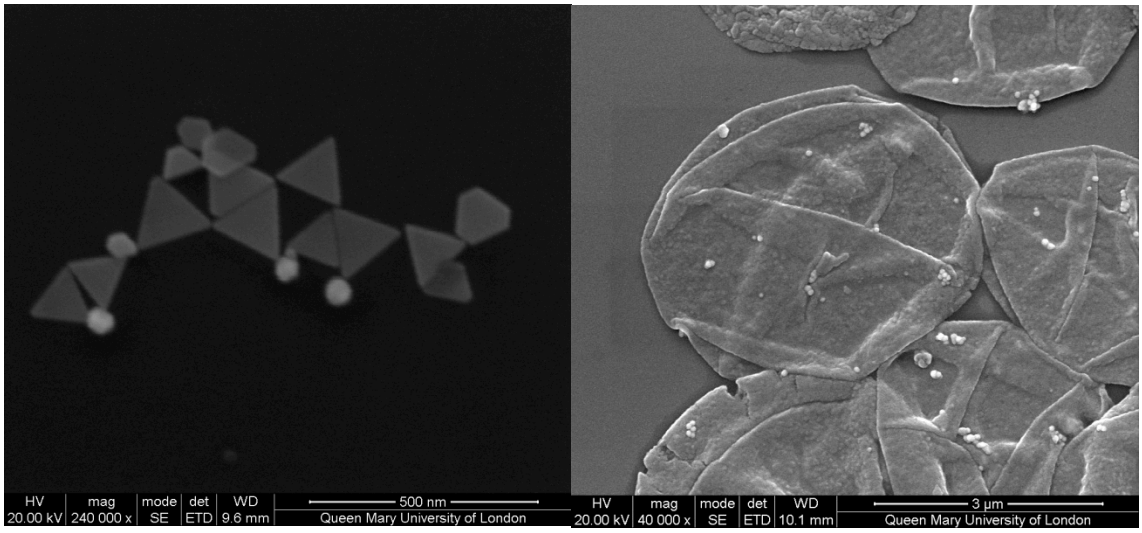

Figure 3-34(a) SEM images of gold nanoplates (b) microcapsules with gold nanoplates

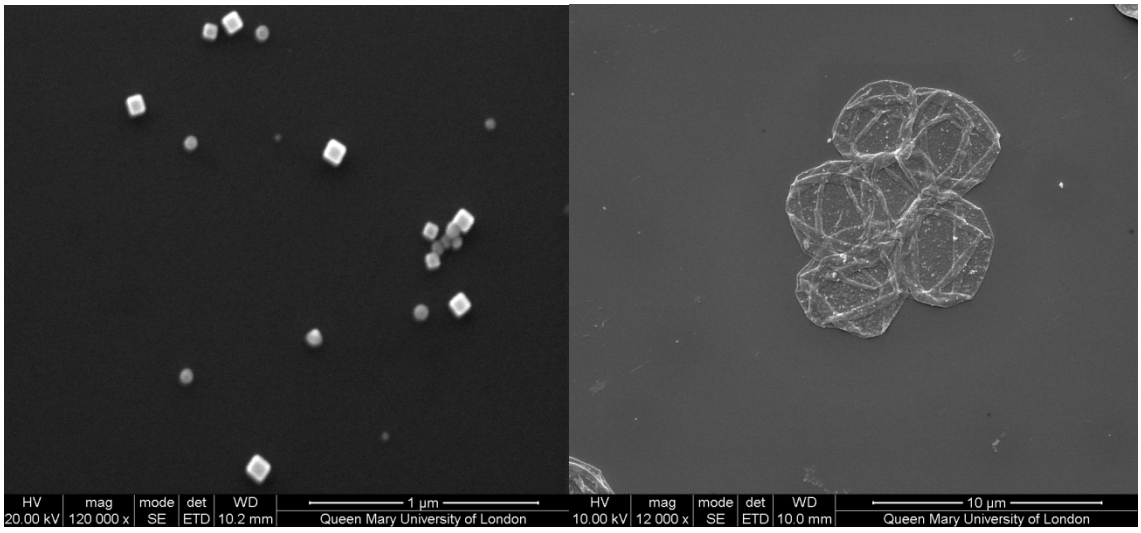

Figure 3-35(a) SEM images of gold nanocages (b) microcapsules with gold nanonanocagse

The gold nanodispersions at a concentration of 1.6 ppm were used for the construction of the shell of microcapsules containing spherical, plate-shaped and cage-shaped nanoparticles. The colourless supernatant from the centrifugation after each GNP implantation step was tested by UV-Vis spectrometer. It only contained trace amounts of gold nanomaterials, estimated less than one percent of the amount of gold nanomaterials added. Furthermore, there was hardly any free gold nanomaterials can be observed in the SEM image (Figure 3-33b, 3-34b, 3-35b). Such observations indicated

that the vast majority of gold nanomaterials have been used to construct the microcapsule walls. The literature has also reported similar results using GNPs (Bedard et al., 2010) and gold nanorods (Guo et al., 2011) in constructing capsules.

Chapter summary

（1）Different gold nanofluids were produced from the one-step approach based on the citrate reduction method with the aid of ultrasonication for particle morphology control. The ultrasonication is an important element in the formation and controlling the morphology of gold nanomaterials. GNPs with smaller size and near spherical shape compared with the conventional citrate reduction method were produced. The size of spherical GNPs can be controlled in between 10 nm and 20 nm, and the average size of gold nanoplates can be controlled in the range of 50 nm - 150 nm, with more uniform and regular shapes. Moreover, gold nanocages can be synthesized by a galvanic replacement reaction in the presence of ultrasonication. The FTIR-ATR result showed negligible residue reactants remaining in the gold dispersions after the purification process.

（2）The utilisation of direct current to control GNP morphology was investigated. DC voltages caused particle aggregation, thus GNPs became bigger when the applied DC voltages were increased. Loose structures were formed at low voltages while large solid structures were formed at high voltages. The colour change of GNP dispersions was an indication of the size change or aggregation as the DC voltage was applied. The CIE1931 colour space can be employed to quantitatively describe this colour change based on the transmission data of GNP dispersions measured by the UV-Vis

spectrometer.

(3) Microcapsules were fabricated by LBL technology and 3 different shapes of GNPs were embedded in the capsule shell to make them sensitive to matched photons.

Chapter 4 Heating behaviour of nanoparticle dispersions

4.1 Ultrasonic heating effects of gold nanomaterials

4.1.1 Experimental setup

Four concentrations (0.13 ppm, 0.4 ppm, 0.8 ppm, 1.6 ppm) of spherical shaped GNPs in the size range of 10 ~ 20 nm were prepared. The samples were held in transparent cuvettes, each at a volume of 50 ml, and were put inside a water bath filled with1 litter DI water. The heating was introduced by an ultrasonic device having a frequency of 60 kHz, positioned at the bottom of the water bath. Each heating experiment was conducted for 5 mins, where the transient temperature increase of the nanoparticle dispersion was measured by one thermocouple immersed inside the dispersion, with the data logged into a PC through a Data Acquisition System (DAQ). DI water, Al_2O_3 particles having the same spherical shape at the concentration of 250 and 125 ppm, and Ni particles having the same spherical shape at 2.5 ppm were used as control groups.

The thermal conductivity of gold nanoparticle dispersions was measured by a KD2. The device is based on the transient hot-wire method. The device has a probe with 60 mm length and 0.9 mm diameter, which integrates in its interior a heating element and a thermo-resistor, as shown in Figure 4-1. The probe is connected to a microprocessor for controlling and conducting the measurements. The KD2 Pro device was calibrated by using de-ionised water before any measurement. Five measurements were taken for each sample at a given temperature. This ensures that the uncertainty of thermal conductivity measurements was within 3%. The effective thermal conductivity of five concentrations was measured, ranging from 0.01 ppm to 3.2 ppm. Before measurement, every sample was sonicated for 3 mins to make GNPs monodispersed in DI-water.

Figure 4-1 scheme of thermal conductivity measurement by KD2 probe

4.1.2. Results and discussion

Figure 4-2 shows the temperature increase of the bulk liquid at four different concentrations of gold nanoparticle, which are 0.13 ppm, 0.4 ppm, 0.8 ppm and 1.6 ppm. It clearly shows that the heating rate of the base fluid was significant even at small concentrations of GNPs compared with DI water. The temperature of the bulk fluids increased almost linearly with the ultrasonic irradiation time. The temperature rising rate increased with the GNP concentrations. While only ~ 2 K temperature increase was observed for the control group, DI water, a temperature rise of 8.5 K was seen for gold dispersion at a concentration of 1.6 ppm, i.e. about four folds increase in the heating rate.

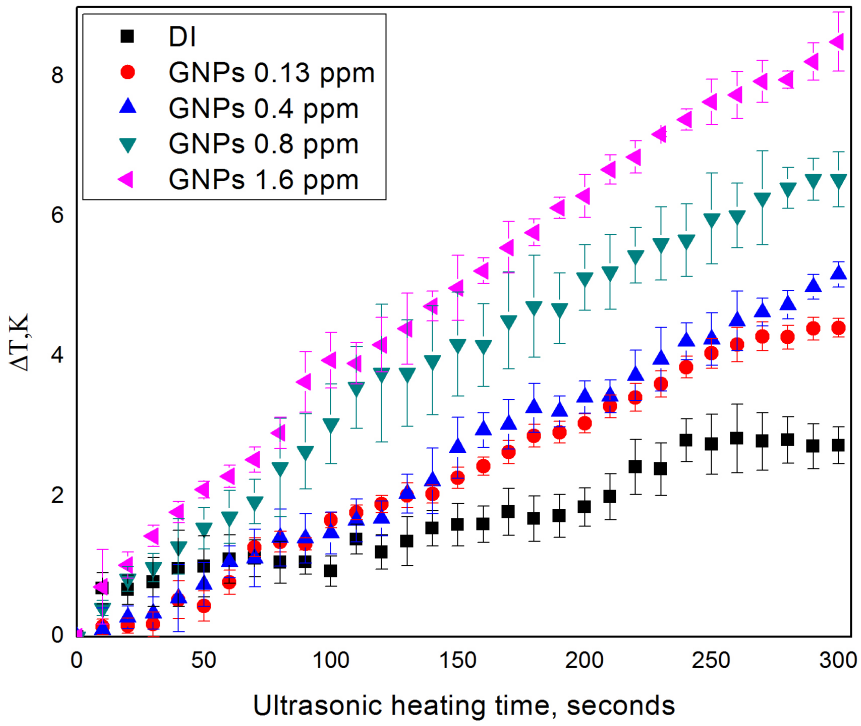

Figure 4-2 The effect of gold nanoparticle concentration on the temperature rise subjecting to an ultrasonic field

Figure 4-3 shows the comparison of different materials' heating effects and illustrates that other nanoparticles could also increase the heating rate but at a slower pace. The averaged bulk temperature increase, dT/dt, is summarized in Table 4-1. It can be clearly seen that gold nanoparticle has much higher heating capability. The temperature rise rate of the lowest concentration GNPs at 0.13 ppm was still higher than that of alumina and nickel nanoparticles at much higher concentrations. Its heating rate was around twice of that of DI water, which indicates that even dilute GNP dispersions could increase ultrasonic irradiation absorption rate significantly. It is apparent from Table 4-1

concentration effect on the heating rate is non-linear.

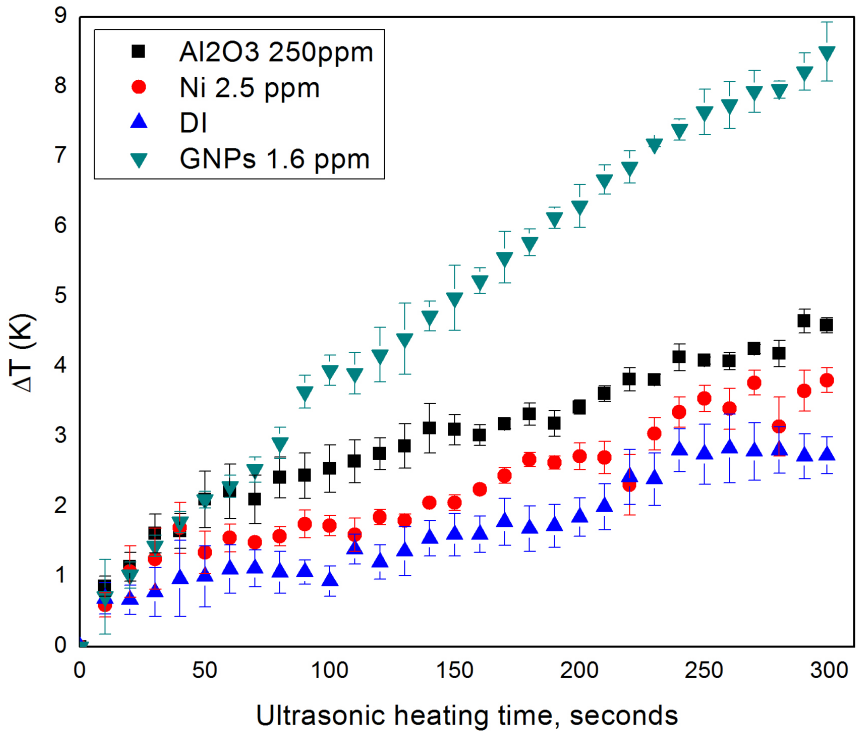

Figure 4-3 The effect of different nanomaterials on the temperature rise subjecting to a ultrasonic field

Table 4-1 Averaged temperature rise rate (K/minutes)

	DI	Au 0.13 ppm	Au 0.4 ppm	Au 0.8 ppm	Au 1.6 ppm	Al 250 ppm	Al 125 ppm	Ni 2.5 ppm
dT/dt	0.43	0.87	1.02	1.24	1.63	0.79	0.76	0.61

After the repeated membrane dialysis, the water-soluble impurities had been removed as could be seen from ATR-FTIR results (i.e. section 3-4), so the heating effect compared with DI water can be ascribed to nanoparticles. These experiments clearly show that the introduction of nanoparticles could focus ultrasonic irradiation much more rapidly than

that of pure water. Different nanomaterials have different effects whereas GNPs possess greater capability than other materials tested.

So far, it is still unclear of the reasons for increased heating rate. Many studies have revealed that a dilute concentration of nanoparticles, or named 'nanofluid', could have higher thermal conductivities than that of base fluid, which contributes to the rate of temperature increase (Wen et al., 2009, Buongiorno et al., 2009). To achieve a four-times increase in the heating rate as shown by 1.6 ppm gold dispersion, a four-fold increase in thermal conductivity is required if all the heating effect comes from thermal conduction.

However, the thermal property measurements showed that the thermal conductivity enhancement of the sample at the concentration of 1.6 ppm was only increased around 50%. It is apparent that the increase in thermal conductivity should not be fully responsible for the rapid temperature increase.

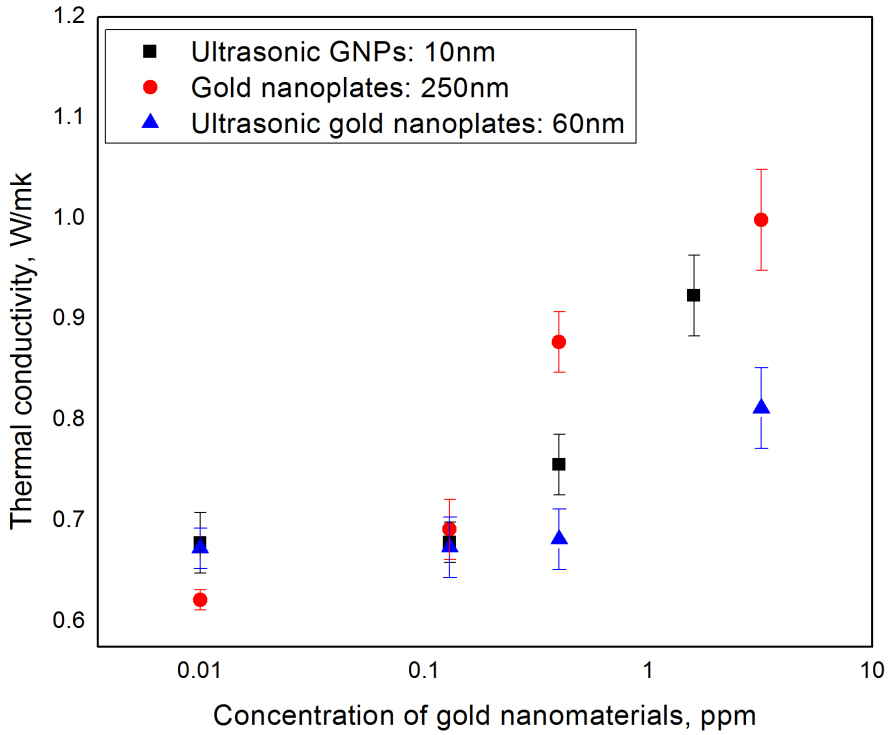

Figure 4-4 The thermal conductivities of the gold nanomaterials (250, 60, and 10 nm)

Figure 4-4 reveals the concentration dependence of the thermal conductivity of different gold nanomaterials. On one hand, when the concentration of gold nanomaterials was increased, the thermal conduction of gold nanomaterials also increased. The thermal conductivity of the lowest concentration gold nanomaterials at 0.01 ppm was higher than 0.6 W/m·K for the DI water. All the gold nanofluids have significantly higher thermal conductivity than the base fluids even when the concentrations of dissolved nanoparticles are extremely low at about 0.01 ppm. On the other hand, the thermal conductivity of gold nanofluids containing 10 nm spherical nanoparticles was higher than that of 60 nm planar gold nanoplates. When the specific surface area rises with the decreased particle size, the thermal conductivity would be higher at low particle dimensions. This size effect should be maintained until the particle size becomes notably bigger. From physics point of view, the thermal conductivity of a solid particle becomes smaller at lower dimensions due to the confinement of the phonon dynamics

by the interface. Thus, further rise in the specific surface area is penalised by a decrease in the particle thermal conductivities. Qualitatively, there would be an optimum particle size where a maximum increase in the effective thermal conductivity could be reached.

In contrast to the particle size effect, when the result of the 250 nm gold plates was compared with that of 10 nm spherical particle nanofluids, a reverse trend was observed. The thermal conductivity of 250 nm gold nanofluids was higher than that of 10 nm spherical particles. The particle at the concentration of 0.4 ppm reached about 0.9 and 0.75 W/mK for 250 nm gold plates and 10 nm spherical particles, respectively. The result showed that not only the particle size but also particle shape played an important role in determining the effective thermal conductivity. While the effect of shape was small at low particle concentrations, it began to exhibit the influence when the concentration was increased. These results are consistent with a few other investigations. For example, the Hamilton-Crosser equation predicts the effective thermal conductivity of heterogeneous combinations by incorporating a shape factor, suggesting the higher the shape factor, the higher the predicted thermal conductivity (Hamilton and Crosser, 1962). Experimentally, Kim and Peterson (2007) reported that different morphologies of carbon nanotubes affected effective thermal conductivity notably. A 37% rise in multiwalled carbon nanotube dispersion could be predicted by the Hamilton- Crosser equation with a massive shape factor (Kim and Peterson, 2007). Recently, the International Nanofluid Properties Benchmark Exercise (INPBE) presented that the effective thermal conductivities of alumina nanorod dispersions (80 nm in length and 10 nm in diameter) were 45% and 30% higher than that of dispersions containing 10 nm spherical alumina at concentrations of 3% and 1% volume fraction of nanomaterials, respectively (Buongiorno et al., 2009).

4.2 Heating effects of nanomaterials dispersions at 200 kHz and 400 kHz

4.2.1 Experimental setup

Figure 4-5 shows the experimental setup. The sample was placed in a glass tube (5 ml), which was exposed for 5 mins under electromagnetic field produced by the commercial equipment (Easy heat 8310, Ambrell UK). EM fields at frequencies of 200 kHz and 400 kHz were generated by coils of 2.5 cm diameter (8 turns) and 2.5 cm diameter (3 turns), respectively. In order to keep the temperature of the coil at ambient temperature, a provision of water circulation in coils was provided. This heating system was performed in a chamber whose ambient temperature is at about 20 °C. In order to precisely test the bulk temperature of gold suspensions and avoid the influence of EM field to thermocouples, an optical fiber temperature sensor containing two channels with computer controlled DAQ system was employed. Meanwhile optical fibre thermometer (Omega FOB102) with an accuracy of ± 0.1°C was used to detect temperature shift. Each sample was placed and fully covered in the center of the coil. DI water as a control group was measured and each sample was repeated at least 3 times. The surfactant solution of gold dispersion without dialysis was obtained by centrifugation (VWR) at 13,000 rpm for 20 minutes to remove GNPs. The supernatant was placed in another tube for centrifugation. This action needs to be repeated 10 rounds due to GNPs residue in the supernatant. A standard impurities solution was prepared at the concentration of 0.48 mg/L (Sigma-Ardrich).

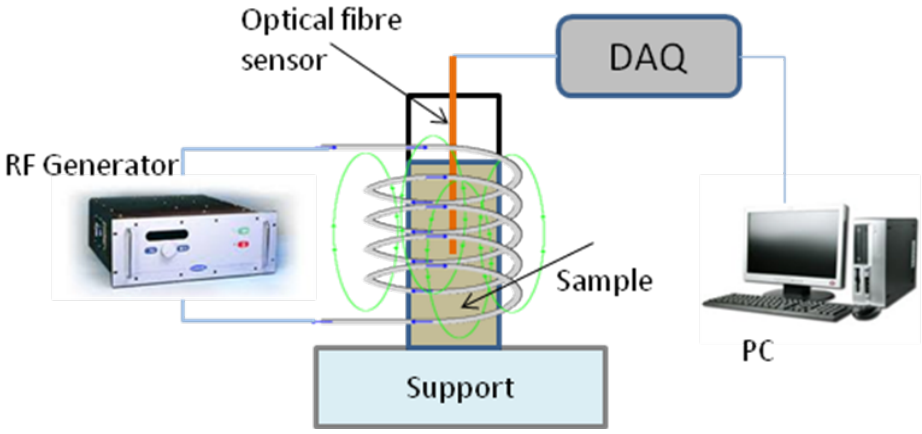

Figure 4-5 Schematic diagram of RF heating study

The bought heating-instrument has water circulation in coils to maintain the temperature of the coil at room temperature. And adjustable current (100-600 A) were used to investigate gold heating effect. Impurities of gold dispersion and standard impurities solution were tested as control groups. Spherical shaped GNPs in the size range of 10 ~ 30 nm were diluted to 4 concentrations (0.13 ppm, 0.4 ppm, 0.8 ppm, and 1.6 ppm) and pre-treated with 3 minutes ultrasonification to make GNPs monodispersed in DI-water.

4.2.2 Results and analysis

The heating ability of different concentration gold dispersions exposed at 200 kHz and 400 kHz under 100-600A magnetic fields for 5 minutes were investigated. Figure 4-6 and Figure 4-7 displayed the RF heating effects of gold dispersion at different concentrations, which are 0.13 ppm, 0.4 ppm, 0.8 ppm, and 1.6 ppm at 200 kHz and 400 kHz, respectively.

At 200 kHz, Figure 4-6 shows that even low concentrations of gold dispersions could increase the heating rate significantly compared with that of the base fluid. The bulk fluids temperature increased nearly linearly with the irradiation time. For example, the temperature increase of the lowest concentration gold nanofluids at 0.13 ppm was 5.9 K,

compared with that of 4.4K for deionized water. At the highest concentration of 1.6 ppm, the temperature increase of gold dispersion was 66% more than that of DI water. Figure 4-7 also presents that the temperature increase rate increased with the increase of nanoparticle concentration but in a non-linear fashion. At 400 kHz, the heating behavior of gold dispersions had a similar trend as that of 200 kHz. But the temperature increase observed at 400 kHz was not as high as that at 200 kHz.

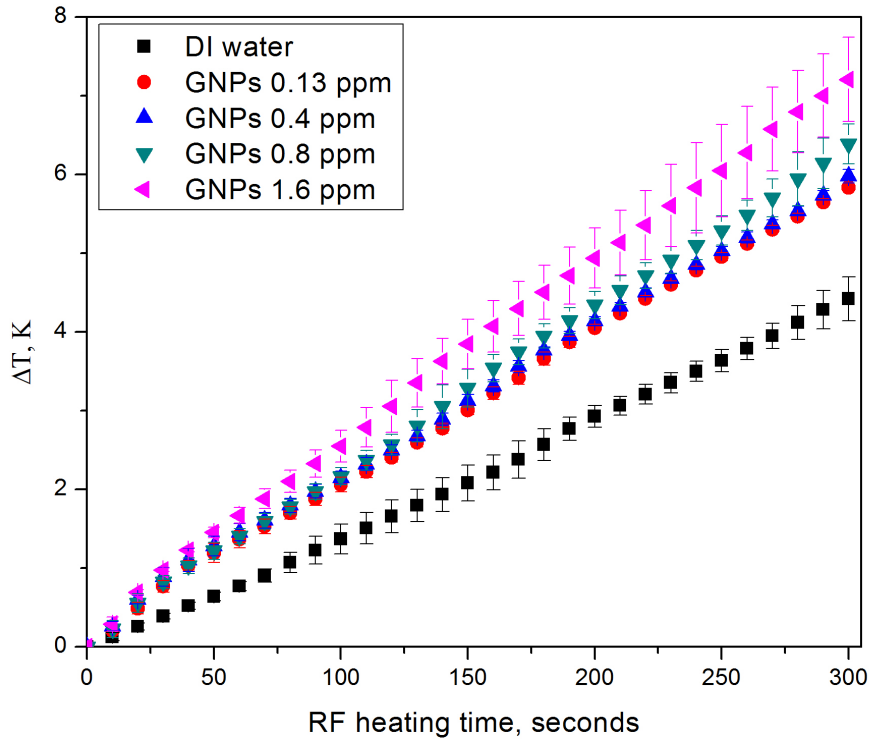

Figure 4-6 The effect of gold nanoparticle concentration on the temperature rise subjecting to a RF field at 200kHz for 5mins

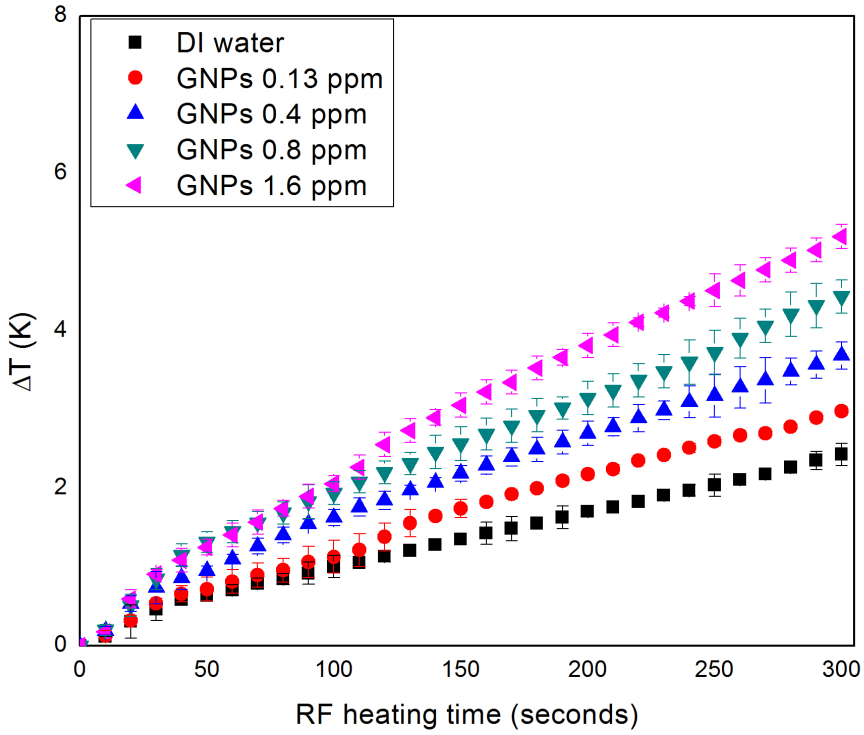

Figure 4-7 The effect of gold nanoparticle concentration on the temperature rise subjecting to a RF field at 400 kHz for 5mins

It shall be noted that there might still be traces of impurities left in the GNP dispersion though after the purification process. These impurities might contribute to the heating process. To elucidate impurities influence, the supernatant liquid and the formulated impurity solutions were also heated in the same system. Figure 4-8 and Figure 4-9 present RF heating effect of impurities of gold dispersion and standard impurities solution as well as DI water. The results of these impurities solutions were very close to the result of DI water which obtained temperature increases about 4.5 K and 2.5 K after 5 minutes RF explosion at 200 kHz and 400 kHz, respectively. It shows clearly that the heating response of these impurities behaved almost the same as the DI water. This result demonstrates the impurities of our sample have very similar absorption rate of radiofrequency at 200 kHz and 400 kHz as DI water and thus does not affect gold heating effect. Consequently the temperature difference observed in Figure 4-6 and Figure 4-7 shall be contributed solely by the GNPs.

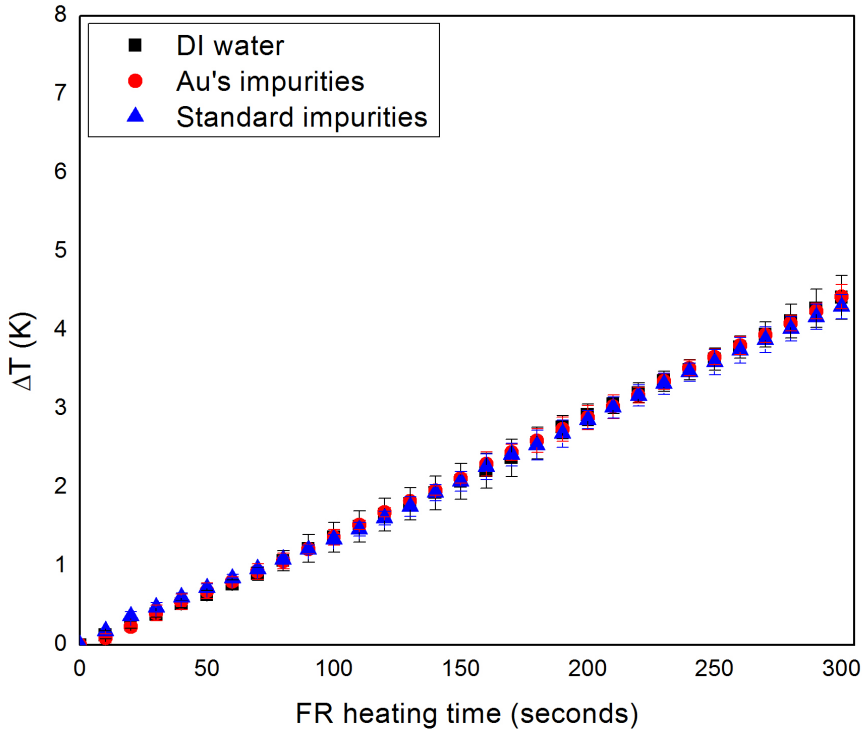

Figure 4-8 The effect of control group on the temperature rise subjecting to a RF field at 200kHz for 5mins

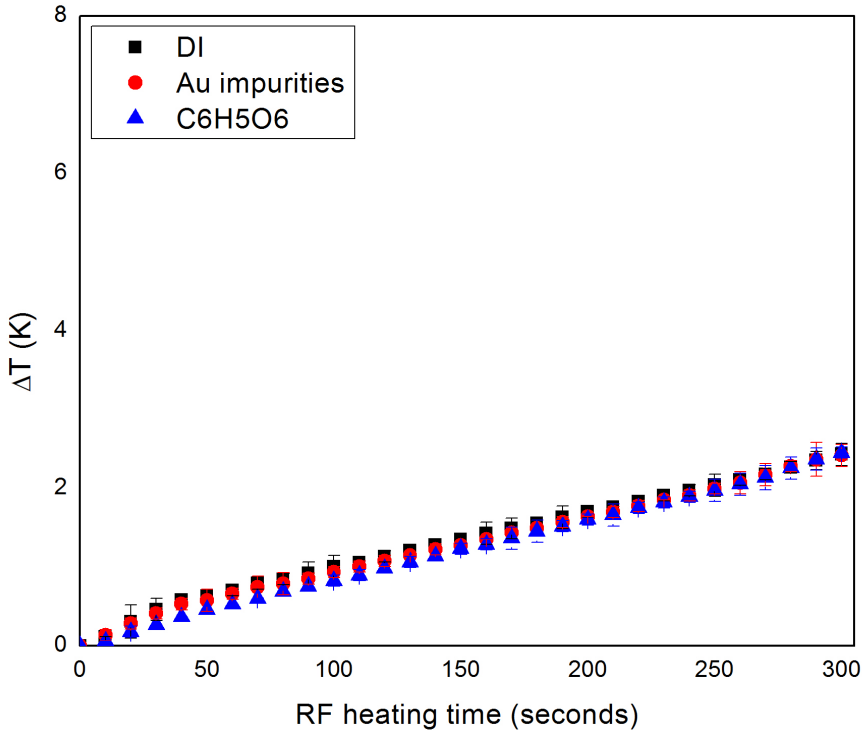

Figure 4-9 The effect of control group on the temperature rise subjecting to a RF field at 400 kHz for 5mins

Gold dispersion (1.6 ppm) was heated under different strength of magnetic field for 5 minutes to investigate the field strength effect. As shown in Figure 4-10, the temperature rising rate increased with the increase of the magnetic field. While only ~ 5 K temperature increase was observed under the lowest magnetic field at 402.2 Oe for gold dispersion at a concentration of 1.6 ppm, a temperature rise of 20.5 K was obtained at 2413.4 Oe, about four folds increase in the heating rate.

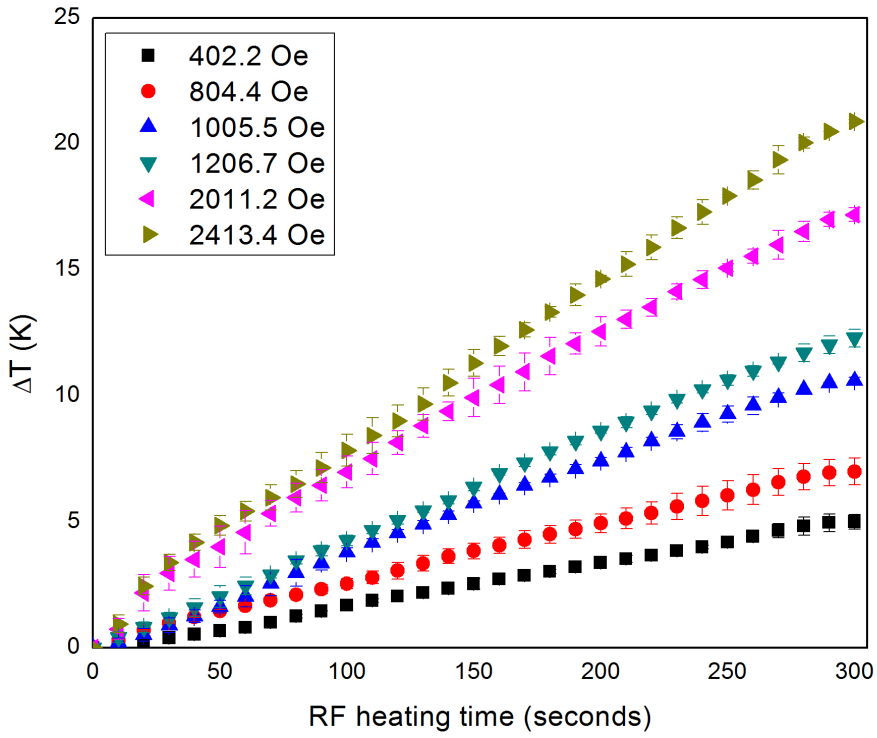

Figure 4-10 The effect of gold dispersion at 1.6 ppm under different the magnetic field

The heating effects of Fe_3O_4 nanoparticles at different concentrations were also investigated under EM frequencies of 200 kHz and 400 kHz for 5 minutes. Figure 4-11 shows clearly that the Fe_3O_4 dispersions could increase the heating rate significantly compared with that of the base fluid. The bulk fluid temperature increased almost linearly with the radiofrequency irradiation time. For example, RF heating effect of Fe_3O_4 nanoparticles at 200 kHz increased more than 40 K within 5 minutes at the

highest concentration of 1.6 ppm, while DI water just increased around 4.4 K. At 400 kHz, the heating behavior of Fe_3O_4 dispersions had a similar trend as that of 200 kHz but the temperature increase observed at 400 kHz was not as high as that at 200 kHz, as shown in Figure 4-12.

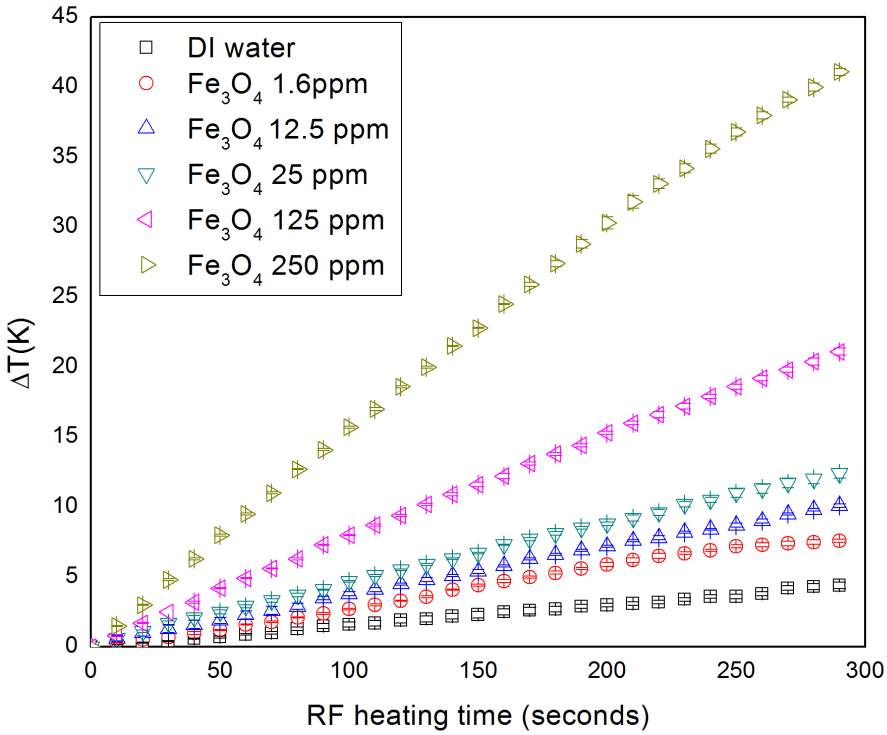

Figure 4-11 RF heating effect of Fe_3O_4 nanoparticles at 200 kHz

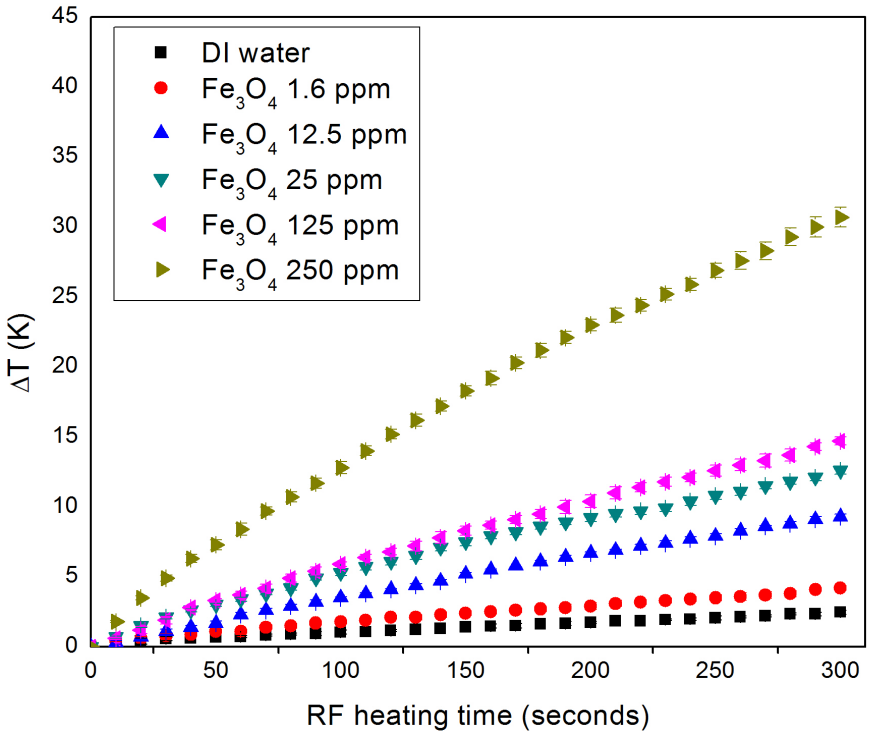

Figure 4-12 The heating effect of Fe_3O_4 nanoparticles under RF field at 400 kHz

4.3 Heating effect of GNPs at 13.56 MHz

As reviewed in Chapter 2, there are currently many conflicting results regarding the GNP heating at 13.56 MHz. It is believed that the inconsistent results are related to the effective dielectric properties, the effect of the impurity, and the field strength. Hence a systematic study has been conducted to investigate the heating effect of GNPs under 13.56 MHz. Our study was performed at 13.56 MHz utilising a home-made RF equipment, and compared with the result from the commercial device in the *Anderson Cancer Centre, US.* The dielectric properties of GNP dispersions were tested aiming to correlate the dielectric loss factor to the heating results.

4.3.1 Experimental setup

Dielectric property measurement

Dielectric property is a main factor in the study of electromagnetic effects of materials. The dielectric test was carried out by the open-ended coaxial method that has been commonly utilised in the dielectric test of biological tissues because of its simplicity, capacity and broad-band feature for non-invasive tests (Athey et al., 1982). The dielectric measurement system contains a vector network analyzer (VNA), Agilent N5230C and the Agilent dielectric property measurement software 85070E (suggested in the frequency range of 100 MHz – 20 GHz)，shown in Figure 4-13. A flange on the tip of the probe was used to facilitate the calibration including the test of open-air and short circuit as well as reference materials. The size of sample holders used in the test was in a diameter of 50 mm and depth of 50 mm in order to meet the requirement of the standard measurement process. A thermometer was used to monitored the bulk temperature of every sample before and after the test. GNP dispersions with and without purification process were tested, with the concentrations being the same as those for

heating effects experiments. A DC conductivity meter, EC-1382B*Analytical Instruments,* is employed to measure the DC conductivity of GNP dispersions.

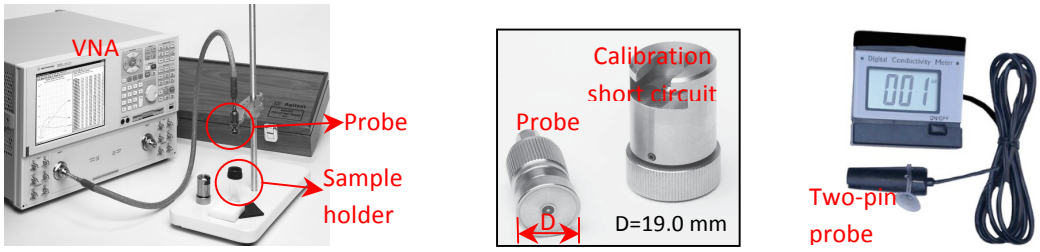

Figure 4-13 Agilent dielectric property measurement system. (a) VNA N5230C; (b) Probe, reprinted from Agilent 85070E software users manual; (c) DC conductivity meter

In-house built 13.56 MHz system

In order to study the heating effects of GNP dispersion, a designed system possessing uniform field distribution over an area larger than the sample holder was used in this study. The heating system involves a power generator, RFX600A Advanced Energy, a matching termination and a microstrip waveguide, showing in Figure 4-14 and 4-15.

The power generator can provide a power of 600 W to applicators. A relatively uniform field distribution over the air gap in this system was generated by the microstrip waveguide. This microstrip waveguide includes a top metallic plate of 70 mm in width and air gap with 10 mm in height to reach a field-strength of 16 kV/m at 600 W. A petri dish was utilised as the sample holder put in the air gap. A termination was used to reduce the reflection, and hence to suppress the standing wave.

Figure 4-14 13.56 MHz high power generator. *Advanced Energy Industries, Inc.* Module RFX 600A. (a) Front panel; (b) Rear panel.

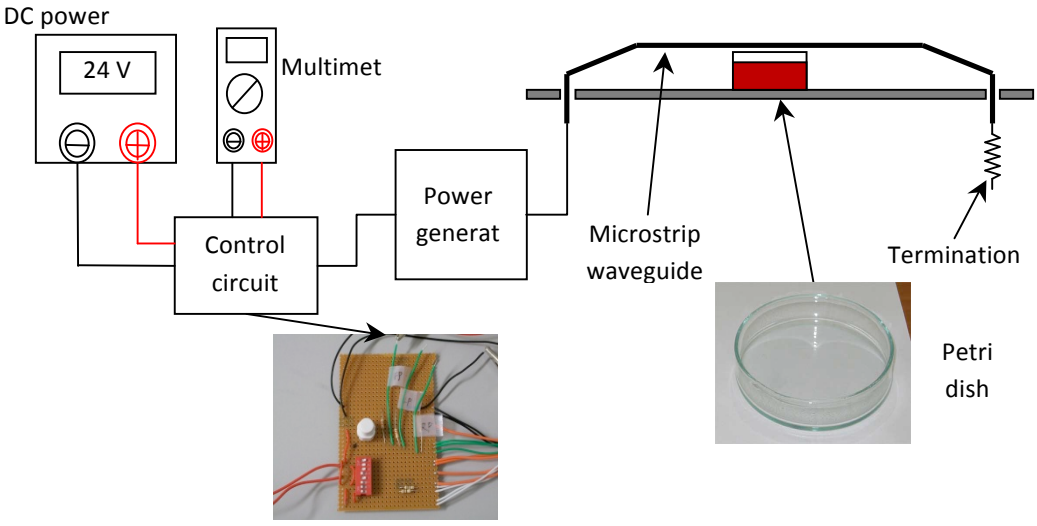

Figure 4-15 Schematic diagram of the RF heating system

Commercial electromagnetic computation software (CST) was used to predict the performance of this microstrip waveguide, and then compared with the results of the experimental measurement (VNA, Agilent N5230C). The test started from 10 MHz because of the limitation of the VNA. Figure 4-16 presents that the reflection coefficient, S11, at 13.56 MHz was lower than -25 dB, meanwhile the transmission coefficient, S21, was close to 0 dB. These results proved that the standing wave effect in the microstrip waveguide was negligible.

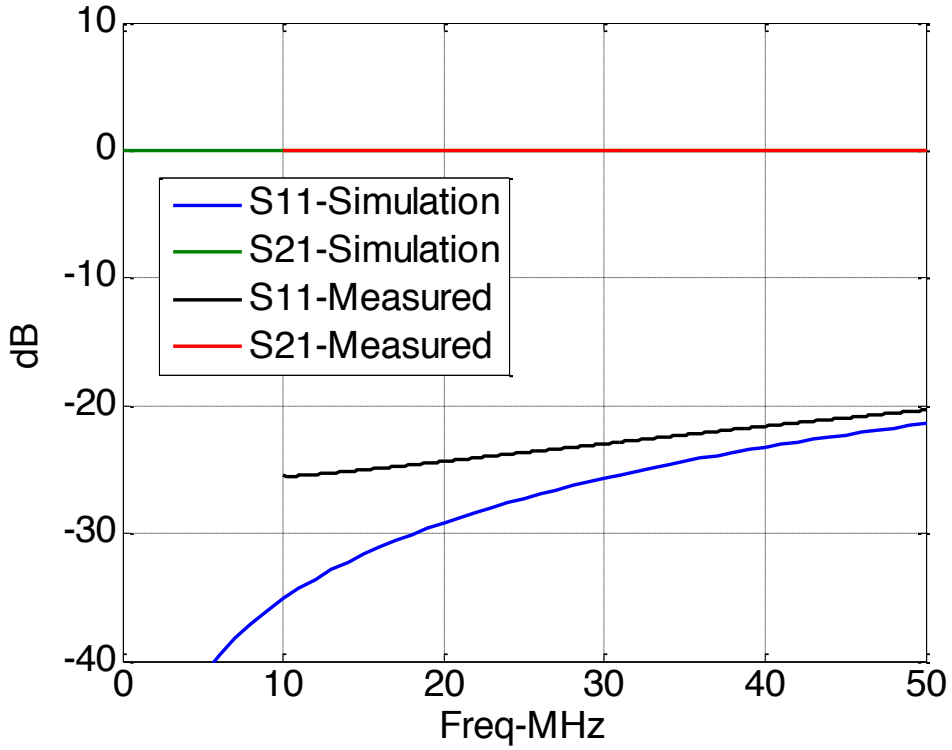

Figure 4-16 Simulation and measurement of the microstrip waveguide. Test is preformed with the microstrip waveguide linked to the two ports of the VNA to test S11 and S21

The field strength of RF heating system was simulated utilising CST and assessed by a dipole probe linked to a spectral analyzer (Rohde & Schwarz FSP Spectrum Analyzer, 9 k-40 GHz). In order to calibrate the output power in the field strength, the power level of a known field strength provided by a function generator, HP3325A, was firstly marked as the calibration data. Figure 4-17 shows the diagram of output power calibration. Based on this calibration data, the receiving power tested from the spectral analyzer was used to calculate the field strength. The field strength can be calculated from the receiving power utilising the dipole antenna theory considering the fact that dipole is commonly regarded as a receiving antenna.

The results of the test, simulation, and dipole antenna theory are showed in Figure 4-18.

The field strength at 500 W is about 16 kV/m, and around 17.5 kV/m at 600 W. The difference in the field strength obtained from these two different methods is small, i.e. within 4.6%.

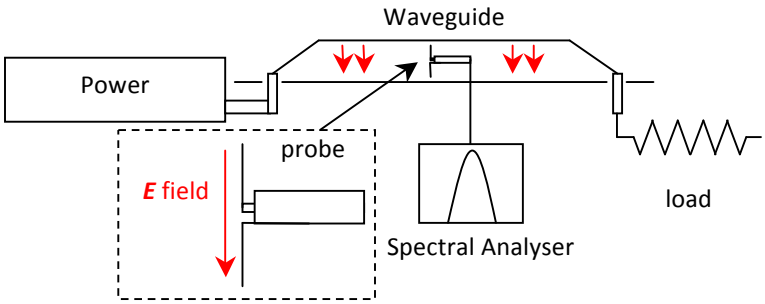

Figure 4-17 Diagram of output power calibration. A probe was put inside the gap and aligned with the electric field. A spectral analyser was utilized to record the signal level picked up by the probe

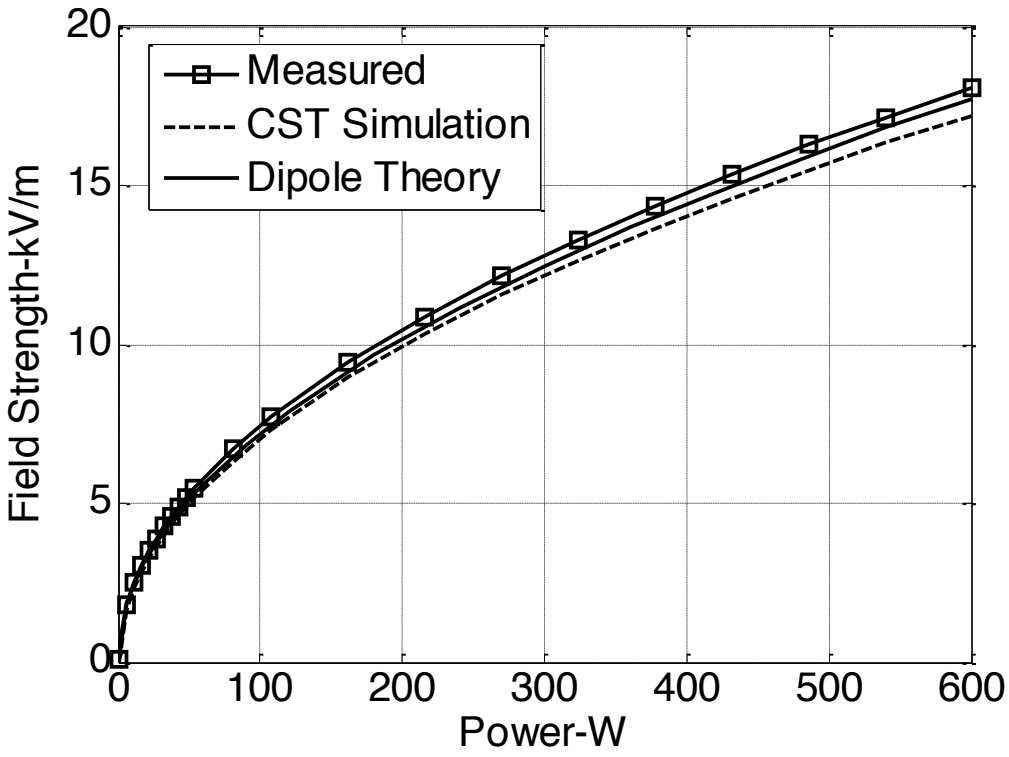

Figure 4-18 Fitted filed strength with different power level (from measured data), solid line, square mark; CST simulation, dashed line, and dipole theory prediction solid line

The RF heating system was built up and performed in an anechoic chamber whose ambient temperature is 20 °C. In order to precisely test the bulk temperature of gold dispersions and avoid the influence of electromagnetic field to thermocouples, a two-channel optical fiber temperature sensor system with computer controlled DAQ system was employed. This system can measure the temperature in-situ with an accuracy of ± 0.1 °C.The power level was set at 600 W while actually producing a real output power of about 540 W. The heating behavior of DI-water, both purified and unpurified GNP dispersions at concentrations of 0.13, 0.4, 0.8 and 1.6 ppm were tested. The power generator was switched off to let the ambient temperature of the chamber cool down to 20 °C before next test.

The Kanzius exposure system

The variance between the results from published studies and the results obtained by employing the microstrip waveguide was very different，thus it is essential to study the reason for this variance. GNP dispersions at concentrations of 0.013, 0.13, 0.4 and 0.8 ppm were posted to the MD *Anderson Cancer Centre* in Houston, Texas for test. The samples were produced by the method described in section 3.2. This test can explain the variance in the electric field strength between the Kanzius system and the microstrip waveguide, as the GNP dispersions were the same. Moreover, by doing this test we can double-check the effects of impurities on the RF heating effect.

GNP dispersions with and without purification were both measured. In addition, two unpurified samples at concentrations of 0.4, 0.8 ppm, were centrifuged at 13500 rpm for 20 minutes in MD *Anderson Cancer Centre* to separate GNPs from surfactant to study the heating effect of the base fluid including non-GNPs products. The procedure of

separating GNPs from surfactant is illustrated in Figure 4-19, where the supernatant is the base fluid.

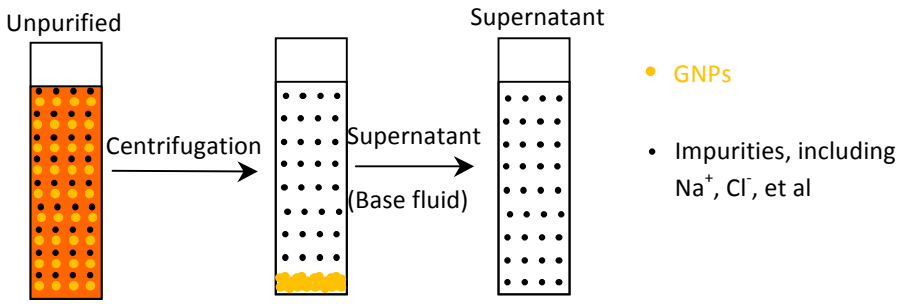

Figure 4-19 The procedure of separating GNPs from surfactant (the base fluid).

4.3.2 Results and analysis

Dielectric properties

The tested results of complex permittivity of GNP dispersions with and without purification at 23˚C (±0.1˚C) are presented in Figure 4-20, and Figure 4-21, respectively. It demonstrates very similar dielectric properties for the purified GNP dispersions, containing the real part and the loss factor, in the frequency range from 100 MHz to 20 GHz. The concentration effect of purified GNP dispersions was small and insignificant. When testing the conductivity of the GNP dispersions in the range from 100 to 500 MHz, the results at the concentrations of 0.13, 0.4, 0.8, and 1.6 ppm showed small difference because of the system fluctuation.

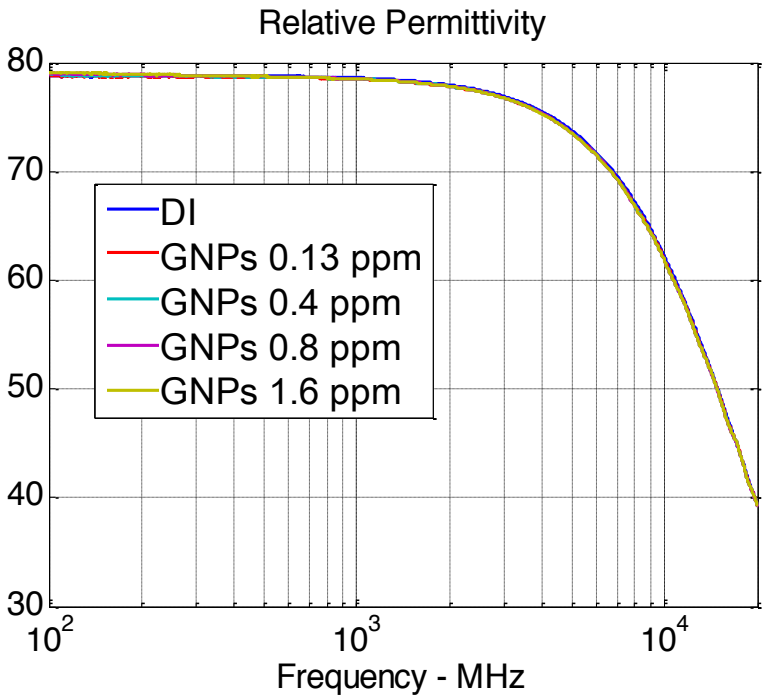
Relative Permittivity
80
70
60
50
40
30
DI
GNPs 0.13 ppm
GNPs 0.4 ppm
GNPs 0.8 ppm
GNPs 1.6 ppm
10^2
10^3
10^4
Frequency - MHz

(a)

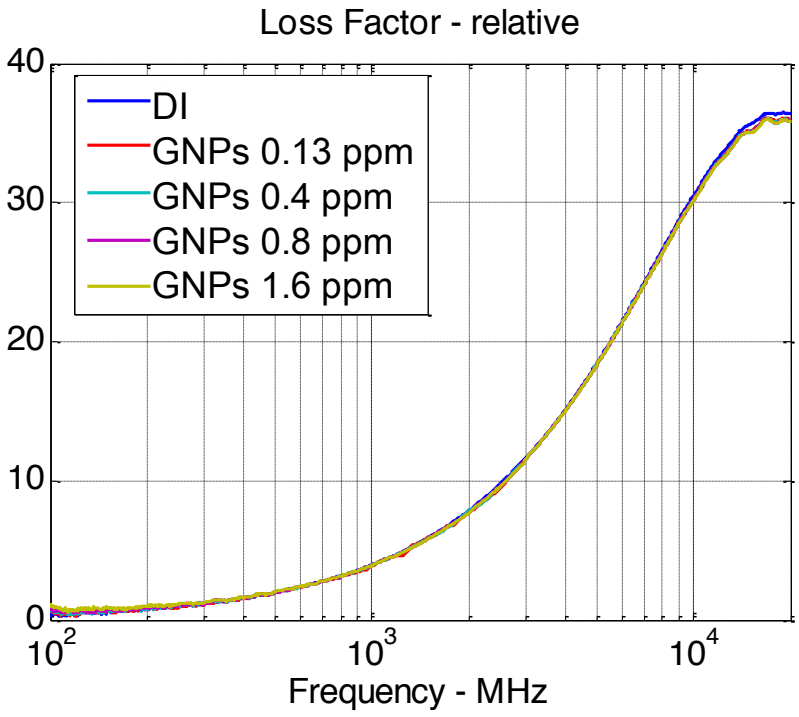
Loss Factor - relative
40
30
20
10
0
DI
GNPs 0.13 ppm
GNPs 0.4 ppm
GNPs 0.8 ppm
GNPs 1.6 ppm
10^2
10^3
10^4
Frequency - MHz

(b)

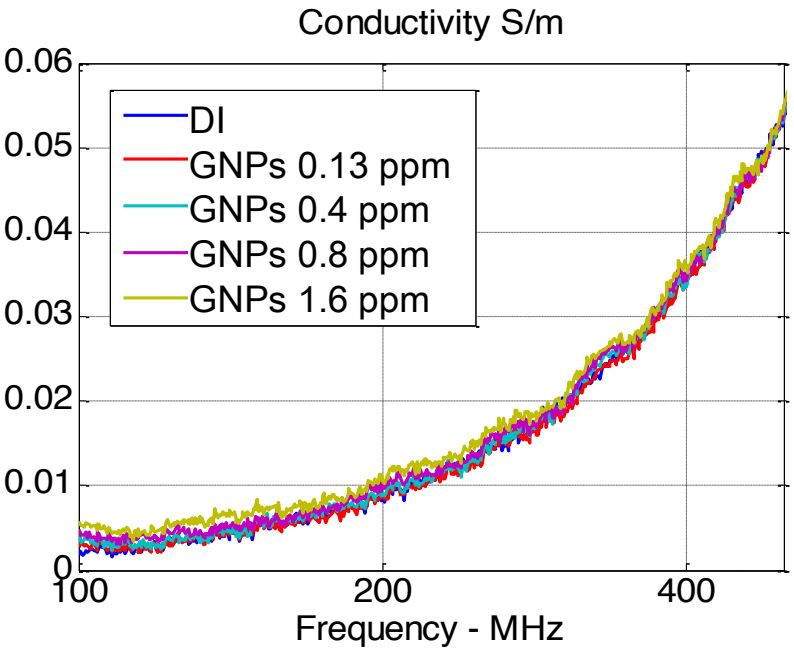

(c)

Figure 4-20 Dielectric properties of purified GNP dispersions.(a) Relative permittivity; (b) loss factor; (c) conductivity

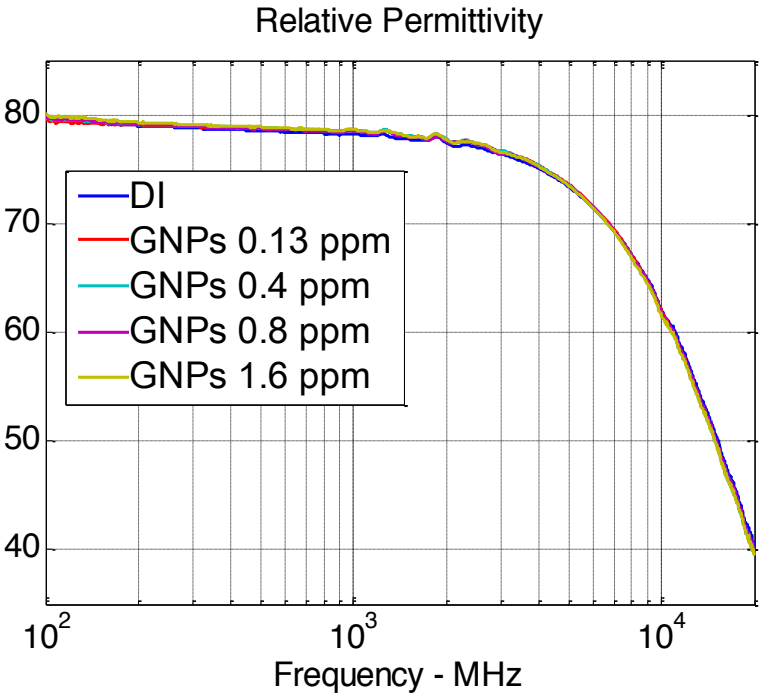

(a)

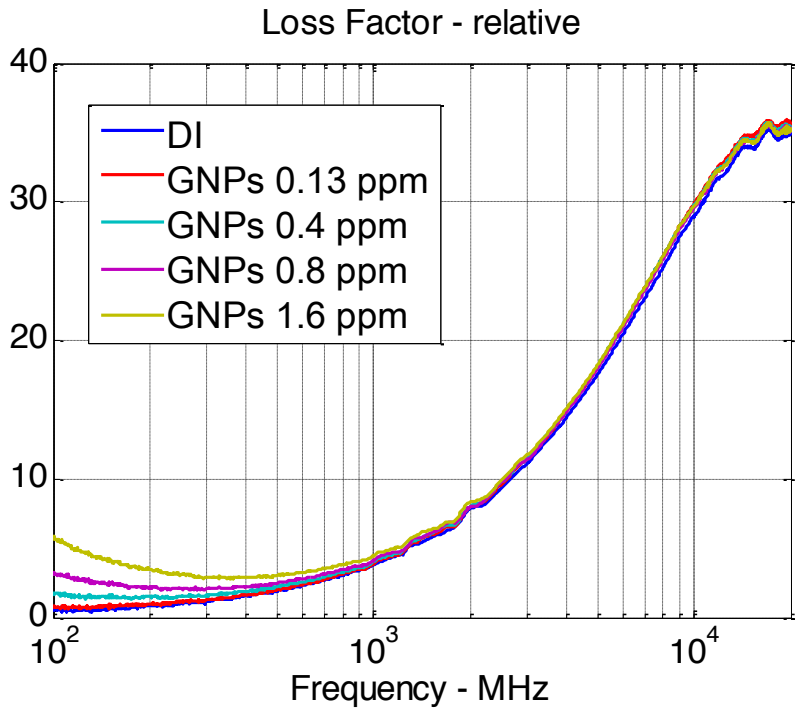

(b)

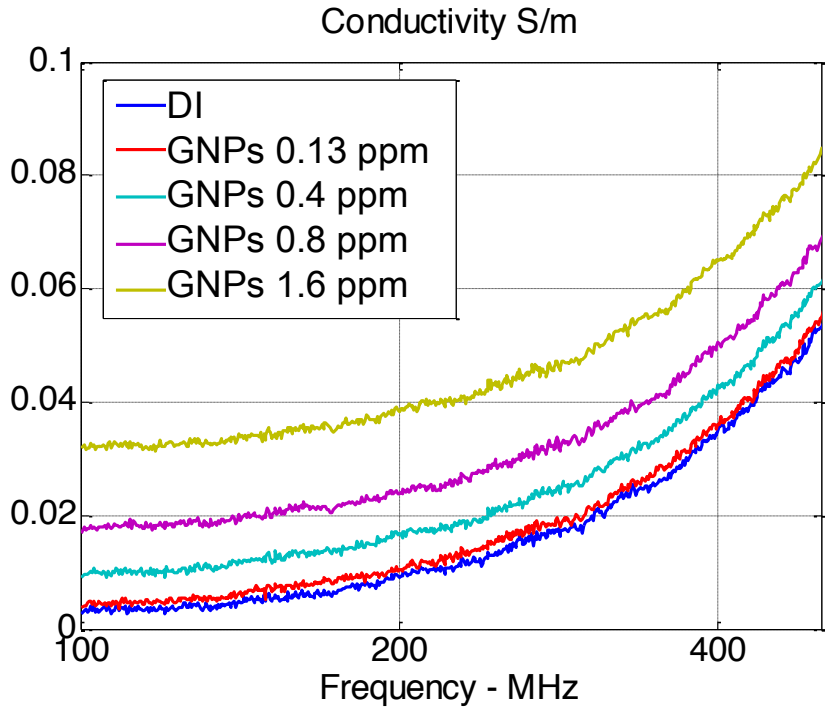

(c)

Figure 4-21 Dielectric properties of unpurified GNP dispersions.(a) Relative permittivity; (b) loss factor; (c) conductivity

The tests were performed from 100 MHz to 20 GHz. The equivalent conductivity at 13.56 MHz should be less than that of 100 MHz as proposed by the Debye model (Gabriel et al., 1996). Figure 4-21c presents that the tested conductivity of the four GNP dispersions was under 0.005 S/mat at 100 MHz. According to Debye model, it provides 2×10^{-4} S/m at 100 MHz and about 1×10^{-4} S/m at 13.56 MHz. Moreover, a DC conductivity meter with accuracy of 1×10^{-4} S/m was employed to cross-check the conductivity of the fluids. The test suggested that the DC conductivities of GNP samples were similar with that of DI-water which was smaller than 1×10^{-4} S/m (Ganguly et al., 2009). These results suggested that the conductivities of GNP fluids at 13.56 MHz should be less than 0.005 S/m and in the scale of 1×10^{-4} S/m.

Heating results from the In-house device

Each sample was exposed under RF field to be heated for 10 minutes using our homemade system. The heating results presented as the transient temperature curves are shown in Figure 4-22(a) and 4-22(b). Figure 4-22(a) displays the temperature increase of GNP dispersions without purification process, meanwhile Figure 4-22(b) is for GNP dispersions with purification process.

As can be seen from Figure4-22 (a), DI-water increased 0.2 K under RF irradiation for 10 minutes. It was detected that the Ohmic loss of the parallel plates induced local temperature increase by 0.3 K in the air gap of the microstrip waveguide after running the RF equipment for 10 minutes without putting sample. As a result, the temperature of DI-water is increased from the heating effects generated by the Ohmic loss. In addition, all the temperature increases of the unpurified GNP dispersions were higher than that of DI-water. The temperature increase were 0.5 K,0.6 K,0.8 K and 0.9 K for

concentrations at 0.13 ppm, 0.4 ppm, 0.8 ppm and 1.6 ppm, respectively. It is obvious that the temperature increase depended on the concentration of GNP dispersions.

However, for the purified GNP dispersions, none of them could obtain a temperature increase higher than 0.3 K. There was no concentration dependent feature seen in Figure 4-22(b). Comparing the results of GNP dispersions with and without purification, it revealed that the unpurified GNP dispersions can be heated up faster than the purified GNP dispersions. Furthermore, in this study the temperature increase caused by GNPs at this frequency could not be proved within the measurement accuracy because the temperature rise is too small. This phenomenon was different from the Kanzius system (Kruse et al., 2002), which will be discussed in the next section.

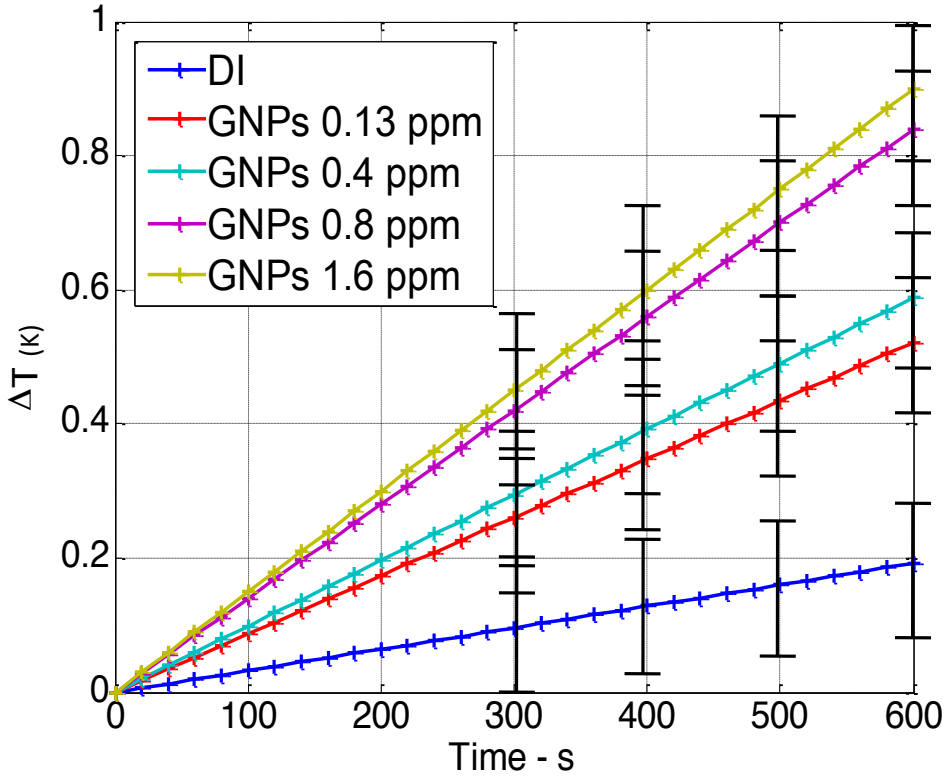

(a)

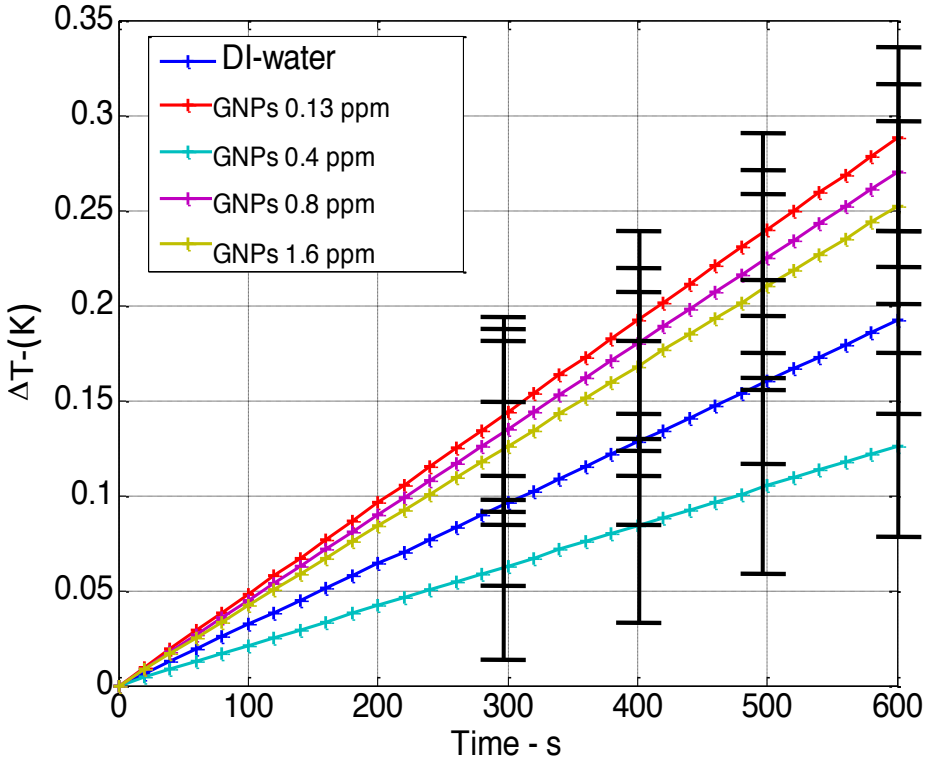

(b)

Figure 4-22 The heating effects of DI-water and GNP dispersions. (a) Unpurified samples; (b) purified samples. Measurement accuracy ± 0.1 °C

Heating results fromKanzius system

Both GNP dispersions with and without purification were exposed under the RF field in the Kanzius system at 600 W for 20 to 120 seconds. An IR-camera was used to monitor the temperature of samples during the RF heating and the accuracy of the IR-camera was ±1 ˚C. Figure 4-23 shows the temperature increase of GNP dispersions with purification under RF irradiation for 120 seconds. The temperature increase was not as much as that of previously reported (Cardinal et al., 2008, Gannon et al., 2008, Moran et al., 2009). For the highest concentration at 0.8 ppm, 4.5 K of the temperature increase was obtained after RF heating for 120 seconds. The temperature of GNP dispersion at 0.013 ppm and 0.13 ppm did not rise higher than that of DI-water within a 120-seconds RF heating period, all achieved ~2 K of temperature increase.

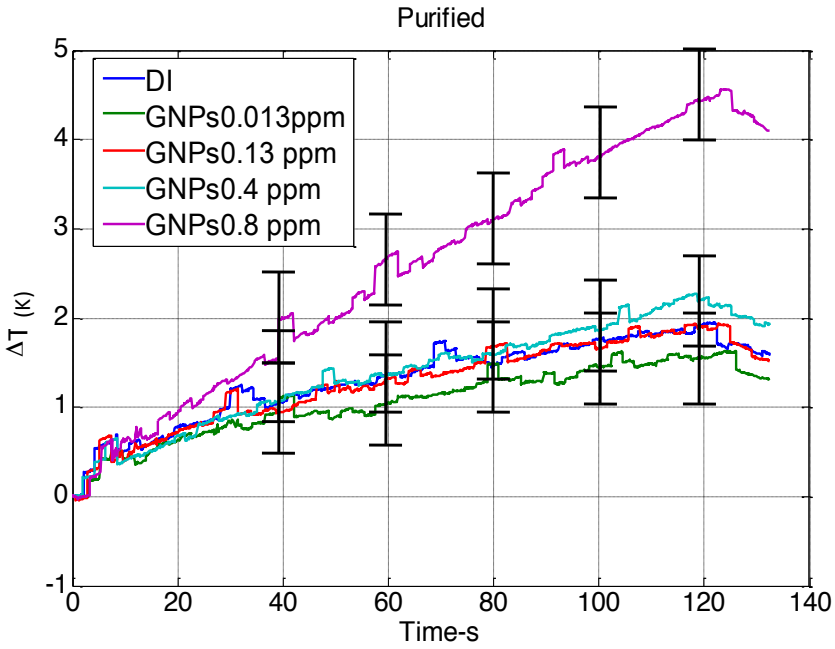

Figure 4-23 the heating effects of purified GNP dispersions under RF field by the Kanzius RF system at 600 W.

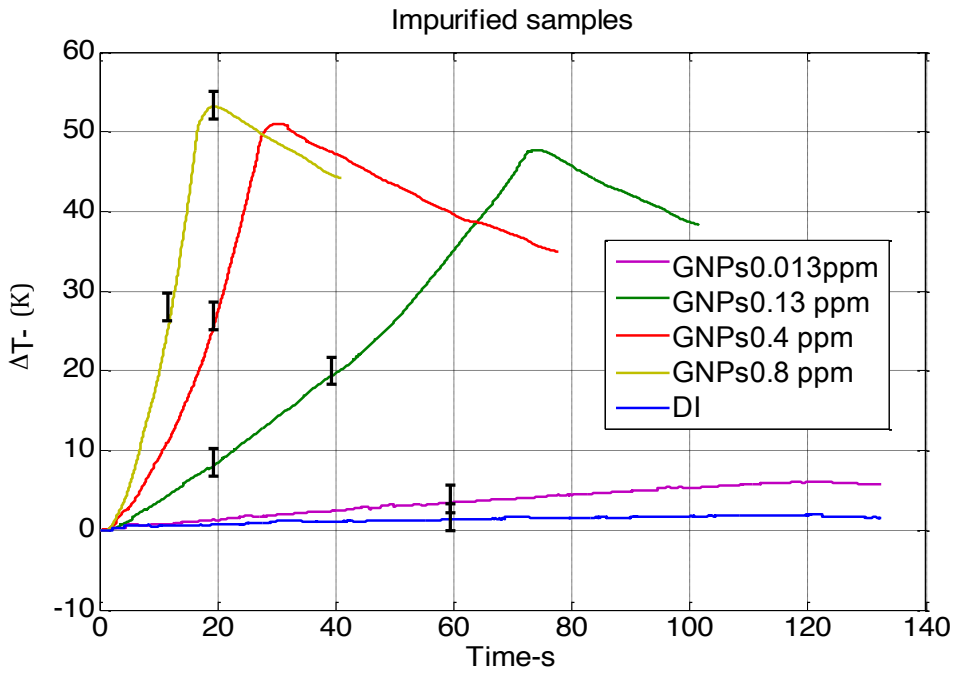

Figure 4-24 the heating effects of unpurified GNP dispersions under RF field by the Kanzius RF system at 600 W. The peak points show the time point as the RF device was switched off.

In order to study the variance between purified and unpurified GNP dispersions, the temperature increases of both groups are shown in Figure 4-25. It can be seen that the temperature of all the unpurified GNP dispersions could be increased quicker than that of purified GNP dispersions at the highest concentration. The results of this study showed that GNPs alone did not enhance the absorbing of RF energy produced by the Kanzius system at 600 W as much as the unpurified samples did. Unpurified GNP dispersions could absorb RF irradiation produced by the Kanzius system at 13.56 MHz and remarkably enhanced the specific absorption rate. To verify that the RF heating effect at 13.56 MHz is caused by the impurities, unpurified samples at 0.4 and 0.8 ppm were centrifuged to separate GNPs. The supernatant was exposed under RF irradiation produced by the Kanzius system at 13.56 MHz for 30 seconds. As can be seen from Figure 4-26, the temperature increase rates of the unpurified GNP dispersions were almost the same as that of their surfactant. According to our results, it can be clearly seen that GNPs alone did not absorb much RF irradiation at 13.56MHz. The RF heating effect was mainly caused by the impurities, which was residual of non-GNPs. Recently Li group also reported similar results of the RF heating effect caused by the impurities (Li et al., 2011). However, there was a small difference of the temperature increase between unpurified GNP dispersions and their corresponding surfactants, which might be caused by the GNPs but could not be proved within the measurement accuracy because the temperature rise difference was too small, as shown in Figure 4-26.

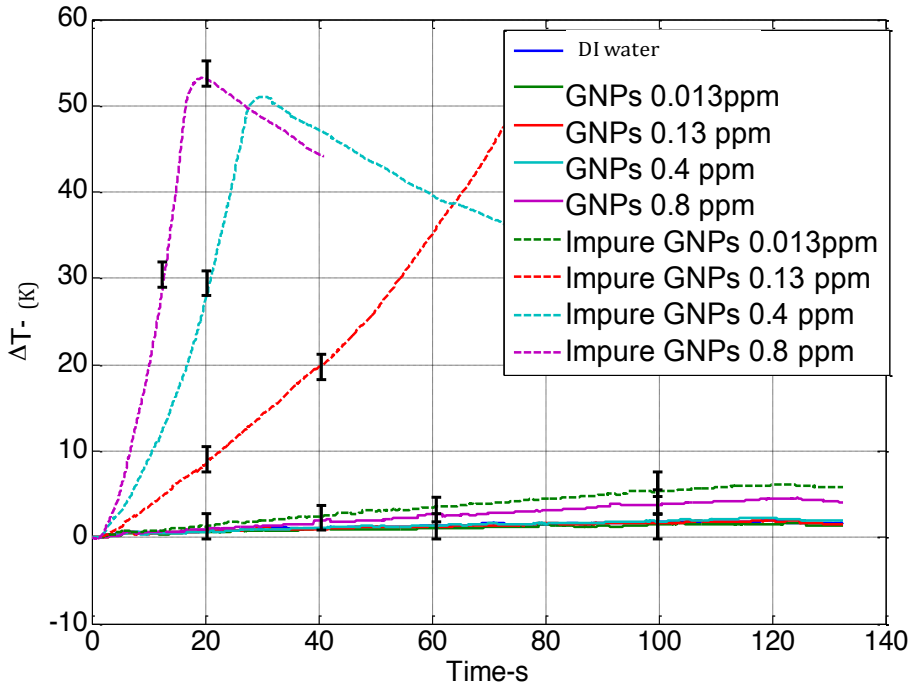

Figure 4-25 The comparison between purified and unpurified GNP dispersions. The peak points show when the RF device was switched off.

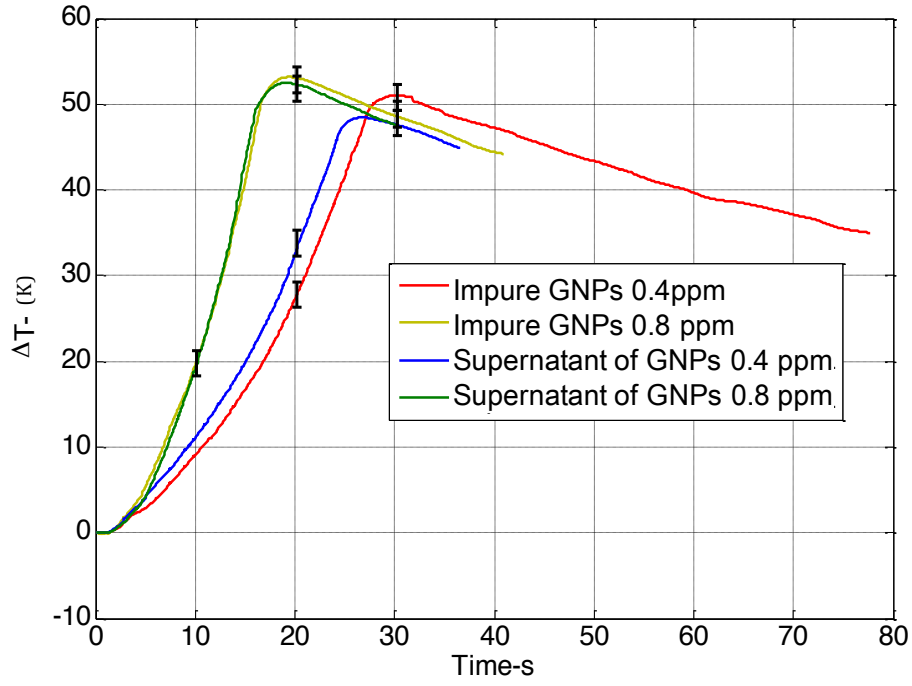

Figure 4-26 The comparison between impure GNP dispersions and their base fluids. The peak points show when the RF device is switched off.

There are a few differences between the results obtained from the Kanzius system and our in-house built system. Firstly, DI-water was heated up to 1.5 °C in two minutes by the Kanzius system. However, using the microstrip waveguide only a temperature rise of 0.3 K was obtained. Second, the field strength of the Kanzius system in the sample was higher than our system. For example, a temperature increase of 4.5 K was observed under the Kanzius system at 0.8 ppm, while the temperature increase was 0.27 K under our system.

4.4 Heating effects of gold nanodispersions at 2.45 GHz

4.4.1 Experimental setup

The study of heating effects of GNPs was also carried out by a microwave oven with a peak power of 480 W, as shown in Figure 4-37. The chamber of the microwave oven includes a plastic bowl, which is fixed by sticky tapes to make sure the sample holder and the glass beaker are at the same height with the microwave source. A hole of 2.7 cm in diameter is designed on the top ceil of the microwave oven chamber to place an optical fiber temperature sensor (Omega FOB102) with an accuracy of ± 0.1 °C to record temperature with heating time. Microwave oven sends pulsed microwave every 30 seconds, the width of the pulse is 5 seconds for the lowest power level and 25 seconds for the peak power level.

Figure 4-27 Setup of microwave heating system

The experiments were performed on DI-water and purified gold nanoparticle suspensions under microwave electronic field. DI-water was utilised as a control group. GNPs were diluted to 2 concentrations (0.13 and 1.6 ppm) and subjected to 3 minutes ultrasonification prior to experiment to make GNPs monodispersed in DI-water. Each sample of 50 ml dispersion placed in a glass beaker was exposed under the microwave

equipment for one minute. Transient temperature curve was obtained by the optical fibre temperature measurement system.

4.4.2 Results and analysis

The temperature shift with heating time at the power level of 480 W is presented in Figure 4-38. The temperature increase with the varying concentration of gold nanoparticle suspension were not easy to be observed because water gave a strong "background noise" at 2.45 GHz. DI water is a good absorber of 2.45 GHz electromagnetic waves which was confirmed by the experiment results. In the first 100 s, the temperature increase of GNP suspension at 1.6 ppm and DI water were 64.0 ˚C and 61.9 ˚C, respectively. But before 90 s it was difficult to distinguish the temperature increase of these 3 samples.

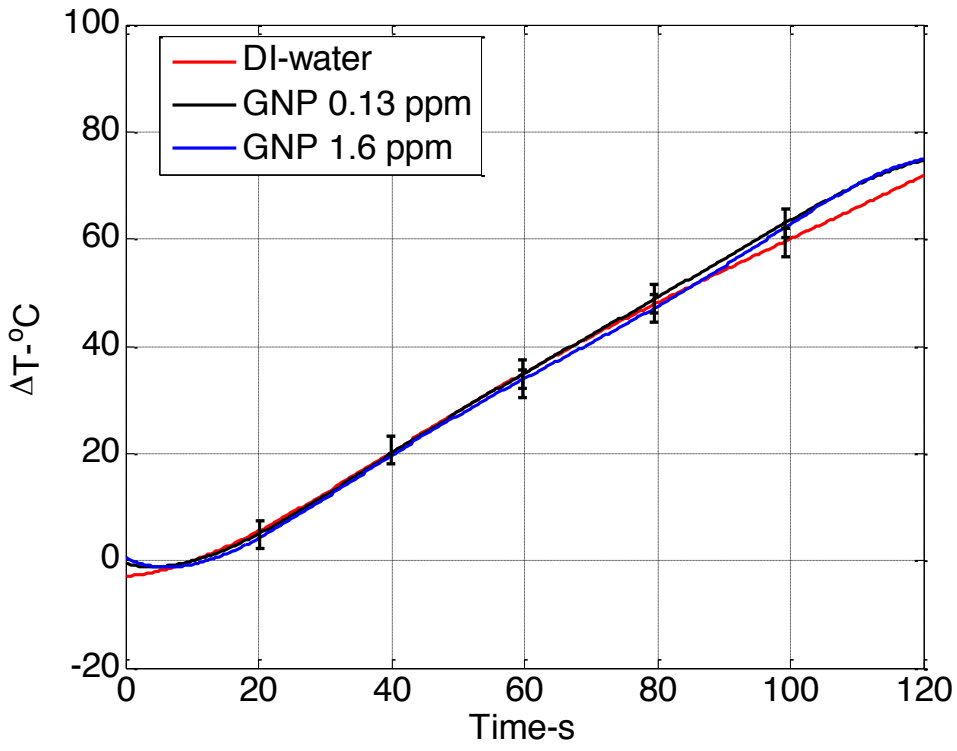

Figure 4-28 Temperature increase with heating time of varying concentrations at microwave power level of 480W

4.5 Laser heating effects of gold nanomaterials

4.5.1 Experimental setup

Laser heating effect experiments were performed using a laser with 655 nm wavelength. The samples were placed in a safety chamber with a hole drilled on the top ceil and the 655 nm red light laser was fixed on the top of chamber and aligned to the centre of the cuvette through the hole to heat up 3.5 ml of gold nano dispersions for 10 minutes, as shown in Figure 4-29. Gold nanofluids with spherical shape particles, plate-shaped particles and cage-shaped particles were at concentrations of 0.13, 0.4, 0.8 and 1.6 ppm. The temperature was monitored by an optical fibre sensor with an accuracy of ±0.1 ºC with the optical fibre close to the inner wall of the cuvette to avoid direct laser illumination. The laser produced a rectangular spot size of 1 cm in length and 0.5 cm in width and the power of the laser was 0.5 W in a continuous wave mode. Microcapsule samples encapsulated between two glass slides were placed in the central of the chamber and exposed under the laser irradiation for 15 minutes.

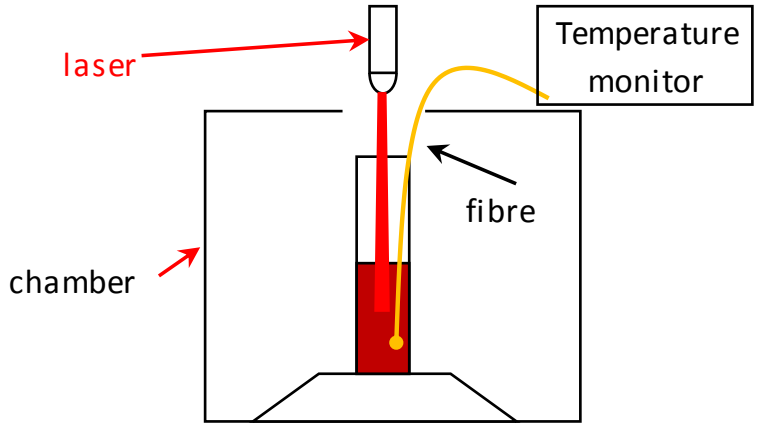

Figure 4-29 Schematic diagram of the laser heating system

4.5.2 Heating results

Heating results of gold nanomaterials

To compare the temperature increase produced by laser irradiation, gold nanodispersions of different morphology and concentrations were exposed to a continuous wave laser at 655 nm with output power of 0.5 W.

For the shape effect of gold nanomaterials, Figure 4-30 clearly shows that the heating effect of gold nanocages was most significant, while the effect of gold nanoplates was in the middle, and both of them were better than that of sphere-shaped GNPs.

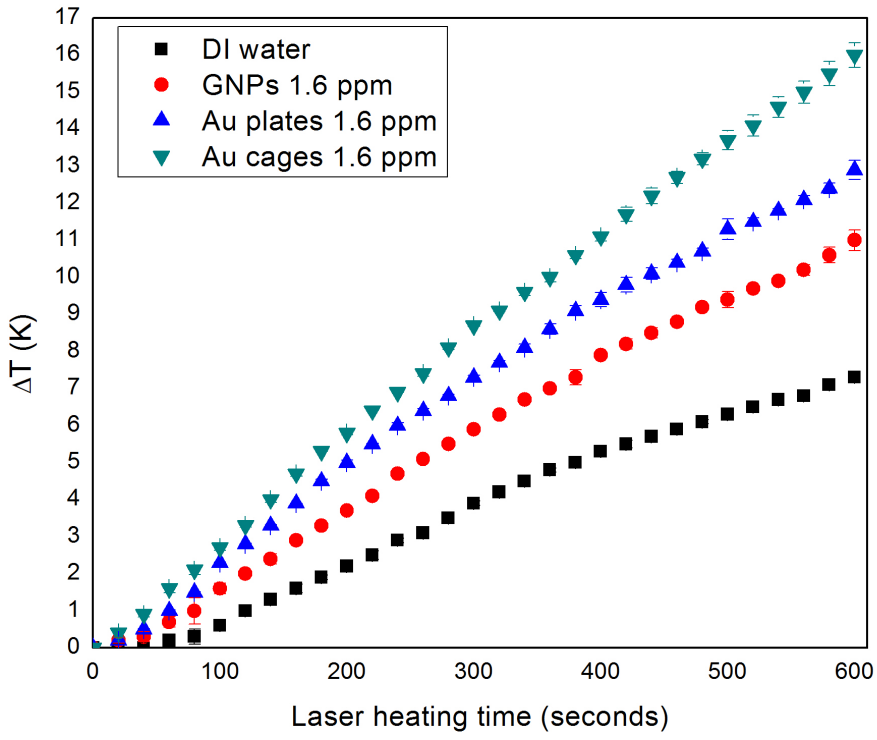

Figure 4-30 Shape effect of Au nanomaterials expose under laser irradiation at 655nm for 10mins

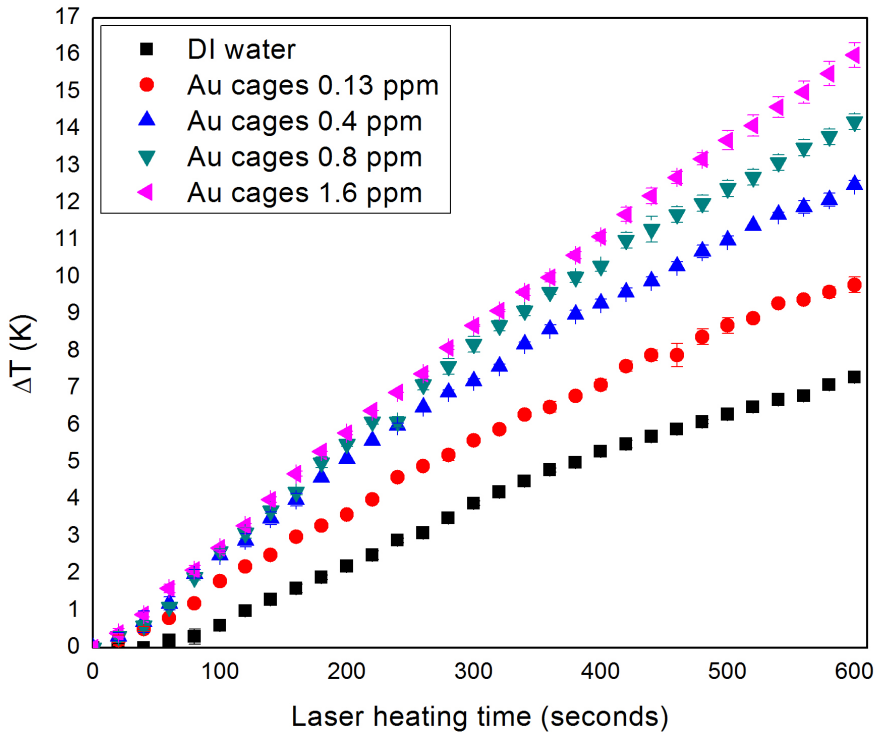

Figure 4-31 Concentration effect of Au nanomaterials expose under laser irradiation at 655nm for 10mins

For the concentration effect of gold nanocages, Figure 4-31 illustrates that the temperature increases of 16, 14, 12 and 9 K were achieved for concentrations of 1.6, 0.8, 0.4 and 0.1 ppm respectively under laser irradiation for 10 minutes. At the meantime, Au nanoplates and GNPs also had concentration effects on laser heating, as shown in Figure 4-32 and 4-33. Temperature increases of 13 K and 11 k were observed for the Au plate and GNP dispersions at their highest concentration of 1.6 ppm, respectively. The temperature increases of different Au suspensions were all higher than that of the base fluid.

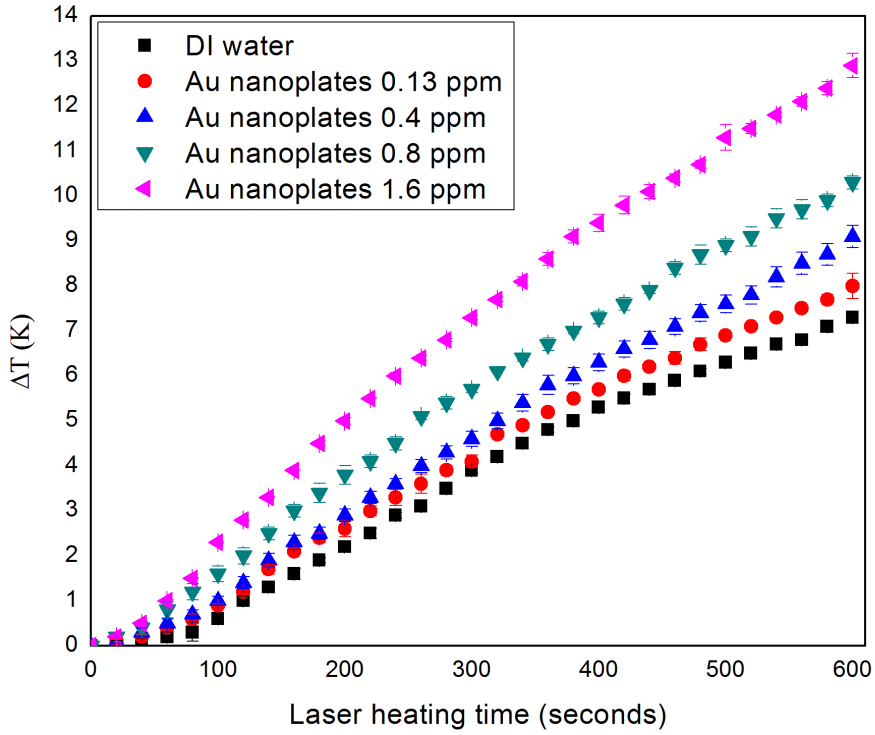

Figure 4-32 Concentration effect of Au plates expose under laser irradiation at 655nm for 10 mins

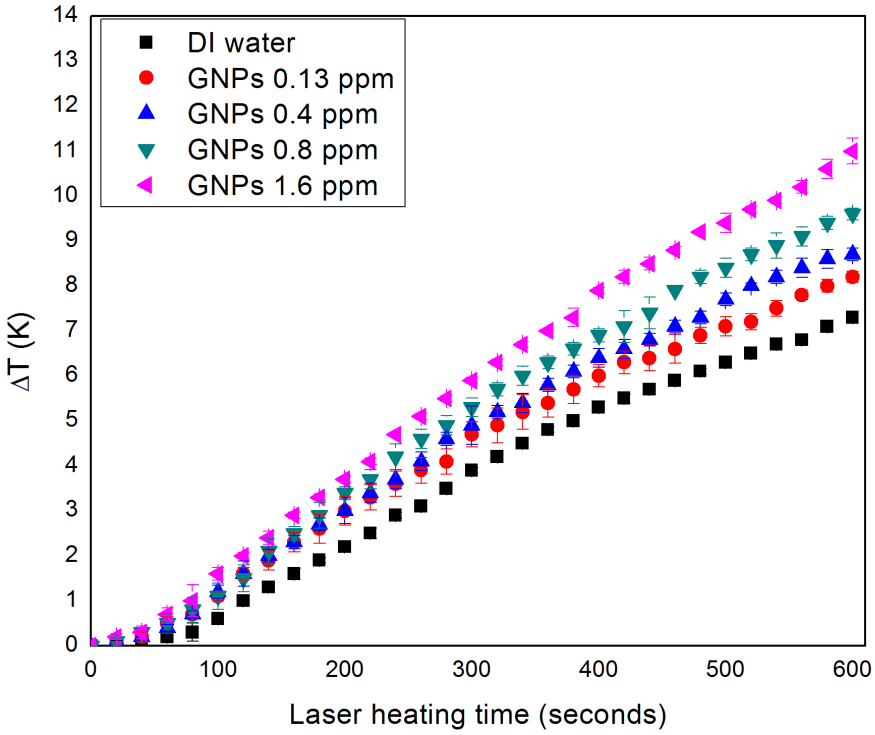

Figure 4-33 Concentration effect of GNPs expose under laser irradiation at 655nm for 10 mins

Heating results of microcapsules

The application of the heating effects of gold nanomaterials was examined in microcapsules. The gold nanomaterials were embedded in the wall of microcapsules through the layer-by-layer (LBL) technology, as described in Chapter 2, to produce NIR-laser sensitive microcapsules.

The heating effect of nanocages in microcapsules was firstly examined. Figure 4-34(a) shows the morphology of the capsules outside the exposed area of illumination spot, and the intact microcapsules appeared as bright red circles. 4-34 (b) presents the morphology of the capsules exposed under direct illumination of the continuous-wave 655 nm laser, and it can be seen that the morphology changed significantly. The microcapsule shells ruptured partially or completely. After laser irradiation the size of capsules also shrunk significantly. For example, the average size of capsules without laser treatment was about 4 μm, while the size of capsules after laser treatment decreased to about 1 μm.

SEM images of these capsules were taken. 4-34(c) shows the morphology of the capsules without exposure to the illumination spot and the intact spherical capsules were seen in the image. The size range of capsules was 3- 4 μm which was very similar to that in Figure 4-34(a). Figure 4-34(d) presents the morphology of the deformed capsules exposed under illumination spot and the intact spherical capsules could not be seen in this image. The size of these deformed capsules was about 1-2 μm. These SEM images were in good agreement with the confocal images, and both confirmed that the morphology of capsules with Au nanocages was changed after laser exposure.

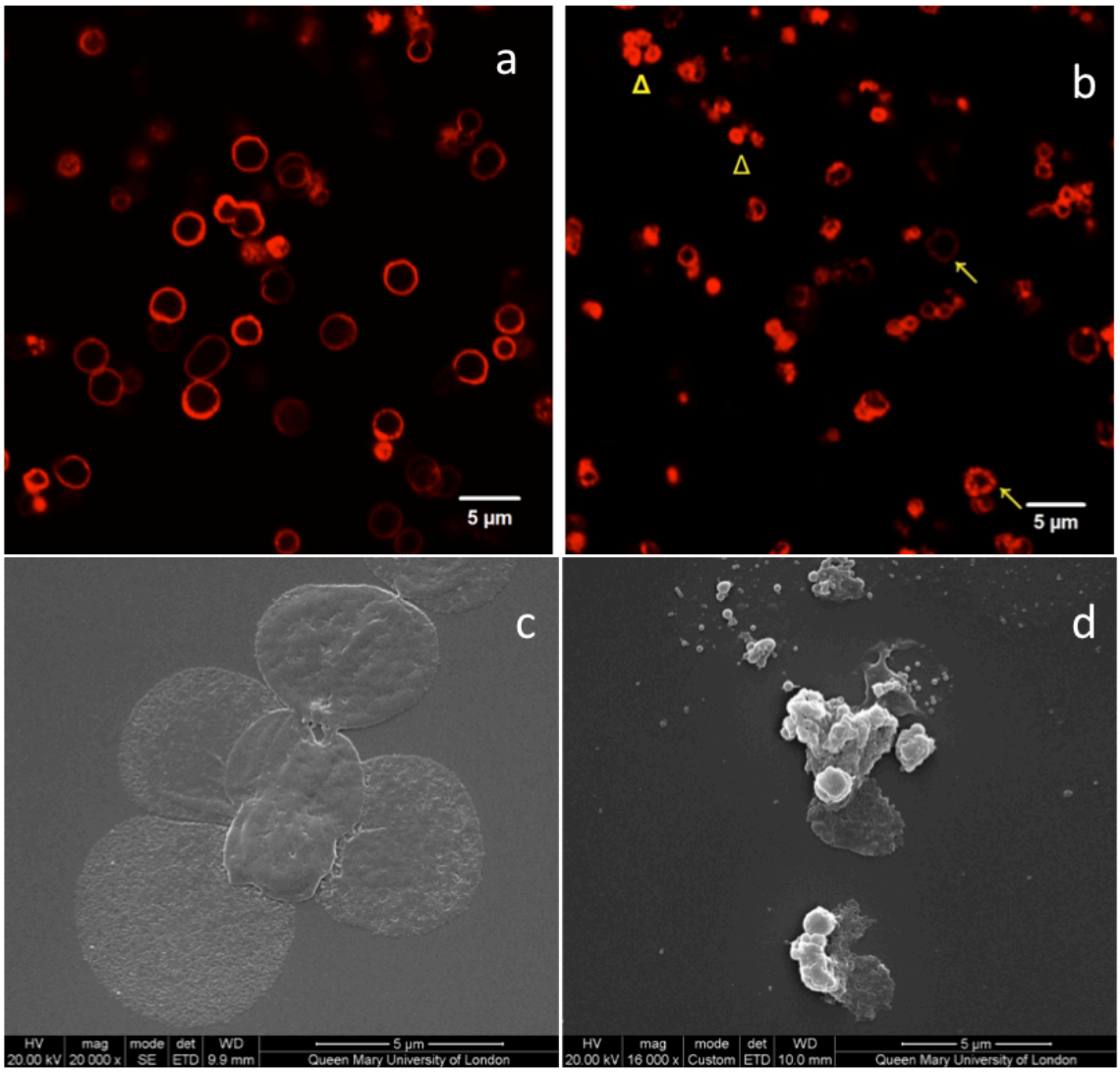

Figure 4-34 Au nanocage-capsules before (left) and after (right) laser for 15mins

The heating effects of nanoplates and spherical-shaped GNPs in microcapsules were also examined. Figure 4-35 and 4-36 present the confocal images of heating effects on capsules with Au plates and GNPs with and without laser heating, respectively. The morphologies of these two kinds of capsules were not changed appreciably after laser exposure.

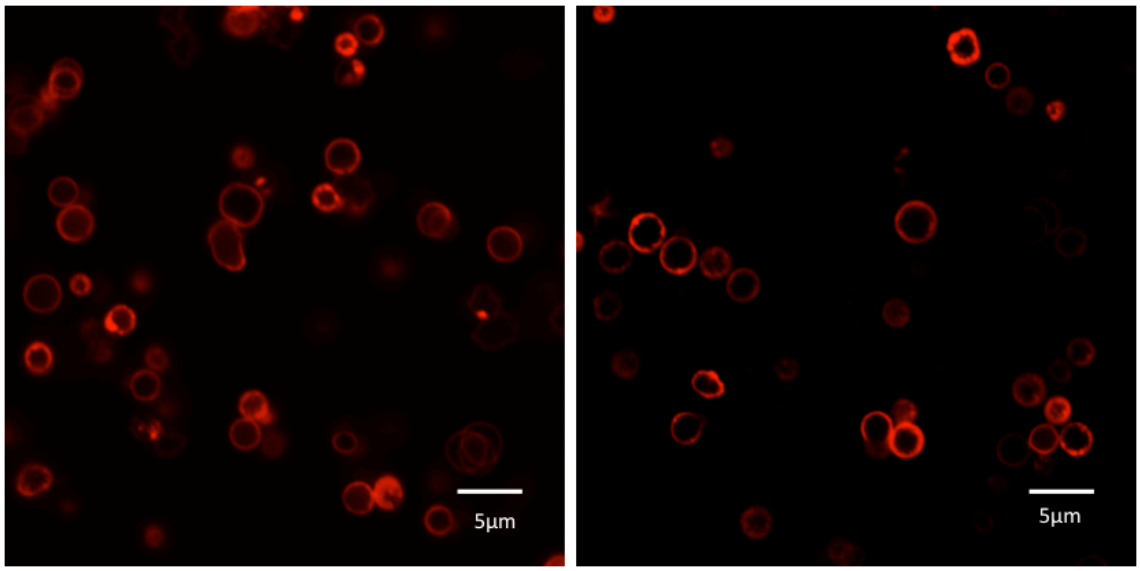

Figure 4-35 Au plate-capsules before (left) and after (right) laser for 15min

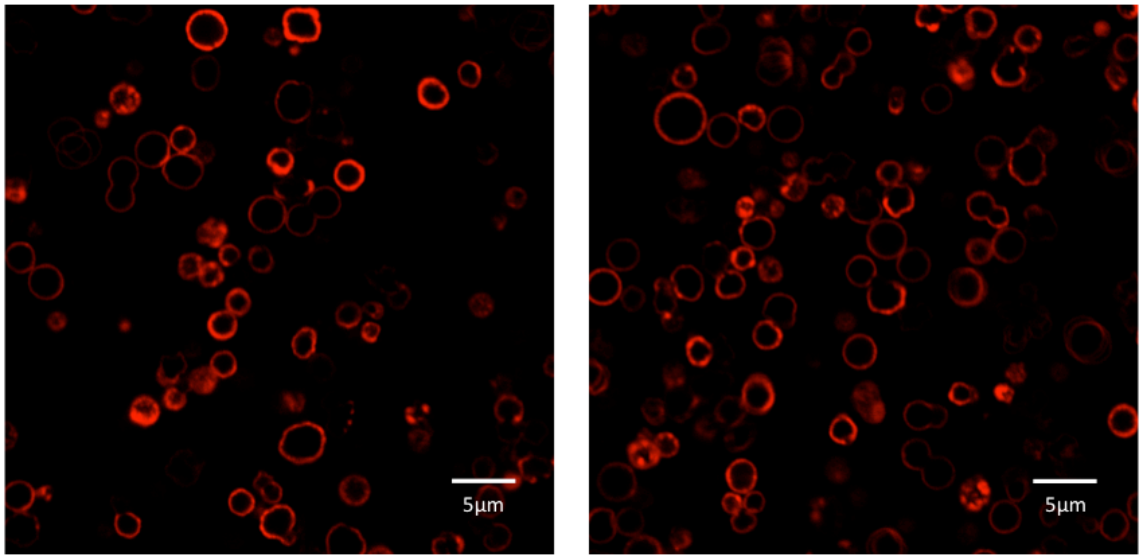

Figure 4-36 Au GNP-capsules before (left) and after (right) laser for 15mins

It has been reported that the structure of microcapsules could be reorganized from lose polyelectrolyte layers into dense framework by heating. These nanoparticles were embedded in the polymer shell to absorb photons and generate heat, which can change the length of the polymer chain rapidly. The weight of capsules was not changed, but the size was reduced after heating, resulting in a denser structure (Dejugnat et al., 2007).

Kohler et al. explained that the thermal shrinkage is the result of going beyond the glass transition of the polyelectrolyte. The layers are changed into viscoelastic stage and restructured by electrostatic and hydrophobic forces to a status with lower total Gibb's energy (Koehler et al., 2006). Moreover, different components of capsule shell have different thermal expansion coefficients that can cause significant thermal stresses resulting in capsule rupture (Arif and Yilbas, 2008). Similar results were also reported by other groups (Guo et al., 2011, Pavlov et al., 2011a).

4.6 Discussion

The experiments showed that nanoparticles can influence the absorption of the external field. Significant heat increase was observed under ultrasonic field, but different results were seen under different frequencies of the EM field. Under extreme low frequency (200 – 400 kHz) and high frequency (i.e. laser at 655 nm wavelength), significant heating effect were observed for low concentrations of GNPs. For instance, the effect of GNPs was comparable with that of magnetic nanoparticles at 200 kHz, as shown in Figure 4-37. For EM at the MHz-GHz spectrum, the experiments showed some effect from nanoparticles, and the results were sensitive to the presence of impurities. Such results contrast strongly to many other studies, where significant bulk temperature increase (i.e tens of Kelvin) was reported by low concentrations of gold dispersion at 13.56 MHz (Cardinal et al., 2008, Gannon et al., 2008, Moran et al., 2009).

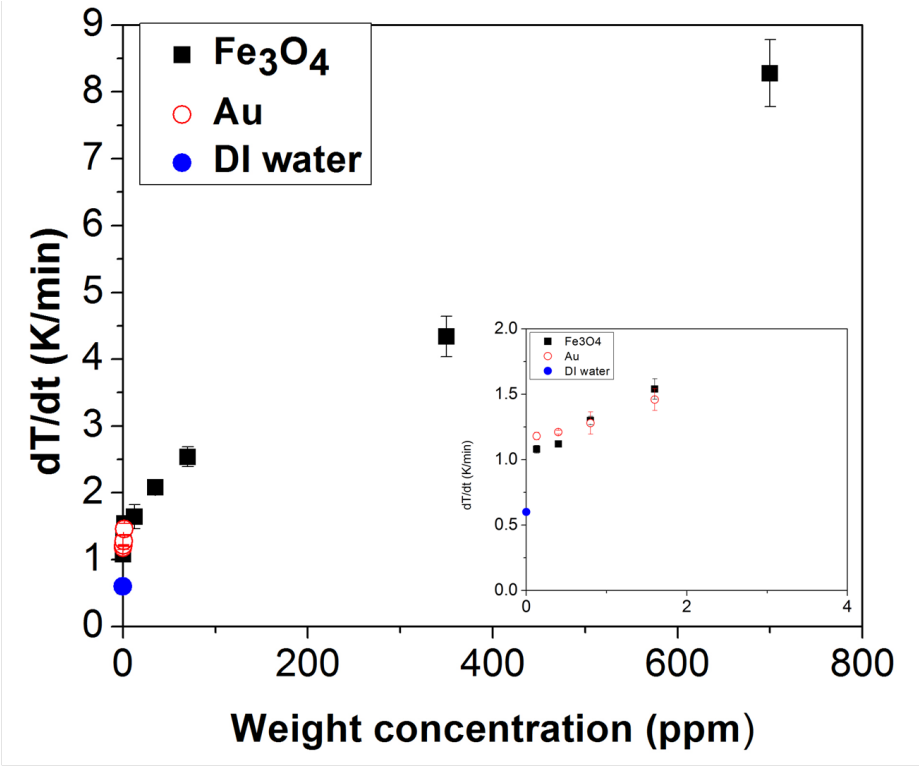

Figure 4-37 Comparison of the average heating rate between GNP and Fe_3O_4 dispersions under EM field at 200 kHz

Clearly, nanoparticle's absorption capability can be affected by both nanoparticles (type, size, shape and concentrations) and heating source (i.e., acoustic, EM frequency and intensity), depending on the interaction of the nanomateirals with the external field. Depending on the heating source, the heating mechanism varies. While some have been established in the physics domain, many are still subjective to strong debates, especially regarding the interaction of GNPs with EM at low frequencies. Generally speaking, ultrasonic heating is due to the cavitation effect caused by the growth and collapse of bubbles. The heating of GNP dispersion under visible light is associated with the surface Plasmon resonance process. The heating of nanoparticles with EM at low frequency (extending from kHz to GHz) should have similar mechanisms, varied between magnetic and non-magnetic materials. A detailed discussion will be conducted below from these three aspects: ultrasonic heating, interaction of nanoparticles with EM at low frequency, and heating of nanoparticles at the visible light spectrum.

4.6.1 Heating effect under ultrasonic field

Ultrasound is a mechanical wave with a low frequency, such as the one used at 60 kHz in the experiment, the major effect is through the cavitation process. The increase in heating rate might be related to an enhanced cavitation effect by the existence of nanoparticles. During a typical cavitation process, bubble volume expands at a negative pressure phase and ends in bubble collapse or fragmentation. Stable cavitation leads to bubble oscillation or transient cavitation where small bubbles undergo large excursions in volume and then terminate in violent collapse in a homogeneous fluid. Various elements can influence the intensities of the cavitation. These elements may contain the size and number of the nuclei, ambient pressure, amount of dissolved gases, vapour pressure, viscosity, surface tension, and the frequency and duration of the ultrasonic

energy. Nanoparticles may act as bubble nuclei to reduce the cavitation threshold and produce more cavitation bubbles, which could cause a higher temperature increase rate (Chen and Wen, 2011). A few previous studies have also shown that different nanoparticles containing latex, silica, GNPs and Fe_3O_4 can enhance the cavitation process (Ho et al., 2011, Smith et al., 2009, Farny et al., 2005). The presence of nanoparticles speeds up the energy transport procedure from ultrasound to thermal energy through cavitation bubbles. Different nanoparticles with different size and concentrations will affect the heating rate notably. Much higher temperature increase rates occurred in dispersions containing smaller GNPs may suggest that smaller particle size is better in providing cavitation nuclei.

4.6.2 The EM heating at low frequency

Magnetic nanoparticles heating under the EM field at low frequency

In the physics field, different low frequency heating mechanisms have been proposed. There are mainly three mechanisms: eddy current heating (or Joule heating), hysteresis heating or relaxation loss. For magnetic particles, the eddy current loss causing heat is negligible because magnetic particles have very high resistivity ($\rho = 10^2$ Ohm·cm). For example, the temperature rise causing by the eddy current is given by (Ghosh et al., 2011).

$$ED = \frac{(\mu\pi d f H_0)^2}{20\rho} \quad (4\text{-}1)$$

Where μ is the permeability of a material, d is the diameter of the particle, and ρ is the resistivity of the material. The calculated temperature rise for magnetic particles is negligible. The major contributors for the magnetic particles are either through the hysteresis heating or through the relaxation loss. For large magnetic nanoparticles

whose size are larger than the size of the single domain, hysteresis heating is the key contributor, where magnetic particles experience a procedure of microstructural alignment. The mechanism included in this realignment contains domain wall motion and magnetization rotation. For smaller magnetic particles whose size is smaller than that of the single domain, the heating is in the form of relaxation loss, either Neel type or Brownian type. The contribution from the Neel type increases as the particle size becomes smaller.

While these established theories can explain the result of magnetic nanoparticles reasonably well, strong debates are still ongoing in the academic field regarding the interaction of GNPs with EM field at the low frequency. As GNPs are non-magnetic, both hysteresis and relaxation mechanisms are not applicable. According to the conventional thought of the major three contributors, the only heating mechanism under EM field for GNP dispersions should be the resistive Joule heating effect. It could be predicted that the temperature increase rate of GNP dispersions will be much lower than that of Fe_3O_4 dispersions. However, as can be seen from Figure 4-37, the average heating rate of GNP dispersion at 200 kHz was closer or slightly higher than that of Fe_3O_4 dispersions under low concentrations. For heating at 13.56 MHz, very small bulk temperature rise was observed, the Joule heating mechanism alone may not be sufficient to explain the result. A number of potential mechanisms will be discussed below, including the dielectric loss model, Joule-Heating model, Mie's theory and Electrophoretic Particle Acceleration model, to enhance our understanding in this topic.

Metal nanoparticles heating under EM field at low frequency

Dielectric loss

For a lossy medium, the theoretical rise in temperature can be calculated utilising

$$\Delta T = \frac{\sigma(\omega) \cdot \left|\vec{E}\right|^2 \cdot t}{2\rho \cdot C}, \tag{4-2}$$

where, σ is the effective conductivity, t is the heating time, $\left|\vec{E}\right|$ is the field strength in samples, ρ is the density, and C is the specific heat capacity. If the complex permittivity of alters, the σ andthe $\left|\vec{E}\right|$ will alter consequently, resulting in a alteration in the heating rate.

Out measurements were performed from 100 MHz to 20 GHz. The equivalent conductivity at 13.56 MHz will be lesser than that of 100 MHz as supposed by the Debye model (Gabriel et al., 1996). The conductivities of four GNP dispersions were tested to be under 0.005 S/mat for 100 MHz. According to Debye model, it provides 2×10^{-4} S/m at 100 MHz and about 1×10^{-4} S/m at 13.56 MHz. Moreover, a DC conductivity meter with accuracy of 1×10^{-4} S/m was employed to cross-check the conductivity of the fluids. The tests suggested that the DC conductivities of GNP samples are similar with that of DI-water which is smaller than 1×10^{-4} S/m (Ganguly et al., 2009), and the conductivities of GNP fluids at 13.56 MHz should be less than 0.005 S/m and in the scale of 1×10^{-4} S/m.

The typical effective media theory can elucidate the insignificant influence of dielectric properties of GNP dispersions. From a macroscopic viewpoint, the Maxwell-Garnett model can be used to model the permittivity of a mixed medium, such as metal particles with spherical shape in a dielectric medium

$$\frac{\varepsilon'_{eff} - \varepsilon'_1}{\varepsilon'_{eff} + 2\varepsilon'_1} = q\frac{\varepsilon'_m - \varepsilon'_1}{\varepsilon'_m + 2\varepsilon'_1}, \tag{4-3}$$

where ε'_m is complex permittivity of the metal particles with spherical shape, ε'_1 is complex permittivity of surrounding medium and ε'_{eff} is the effective dielectric constant as well as q is the volume fraction of the metal particles. In the Maxwell-Garnett model, a constant electric field is expected and applied in an EM field with wavelength that is bigger than the particle size and separation distance. It should be pointed out that the Maxwell-Garnett model is a small-q theory that is suitable for this GNP samples. For GNP dispersions at the lowest concentration, such as in the scale of ~10^{-6}, Eq. (3) expects that the maximum effective permittivity rise will be smaller than 7.8×10^{-6}, and for the highest concentration of GNP dispersion at 1.6 ppm, the maximum effective permittivity rise will be smaller than 0.0001%. It is apparent that the difference in the mixture permittivity is insignificant from the viewpoint of macroscopic theory.

From a microscopic viewpoint, the dielectric properties are because of corporate dynamics of molecules under the impact of an EM field. In our case the stable GNP dispersions containing GNPs are supposed to be well suspended in DI-water and preform as dipoles in an electric field. Thus, the effective permittivity of DI-water and polarized nanoparticles can be written as

$$\varepsilon'_{eff} = \varepsilon'_1 + q\left(4 - \varepsilon'_1\right). \tag{4-4}$$

The detailed derivation is presented in Appendix I. It is expected that the maximum permittivity rise will be smaller than 7.8×10^{-6} for the highest concentration of GNP dispersion at 1.6 ppm, the maximum effective permittivity rise will be smaller than 0.0001%. These results are the same as the results predicted by the macroscopic Maxwell-Garnett model.

The heating rate can be analysed by

$$\frac{d\Delta T}{\Delta T} = \left|\frac{\Delta\sigma(\omega)}{\sigma(\omega)}\right| + \left|\frac{2\Delta|\vec{E}|}{|\vec{E}|}\right| + \left|\frac{\Delta\rho}{\rho}\right| + \left|\frac{\Delta C}{C}\right|. \quad (4\text{-}5)$$

The heating rate of GNP dispersions will maintain the same as that of DI-water unless there is one element being altered remarkably. The field strength in GNP dispersions is not changed significantly as the complex permittivity suffers a tiny change. Moreover, the density and specific heat capacity do not change significantly because the concentrations are too low. Generally speaking, the alteration in the heating rate is expected in the scale of 10^{-6}. The dielectric loss indicates that the variance in temperature increase between GNPs and DI-water should be ~10^{-6} and this would not be able to be monitored by using our temperature sensor.

On the other hand, for the GNP dispersions without purification process, it has been detected that the loss factor rises apparently with the rising of the concentration. The conductivity performs a strong concentration dependent feature. When any of non-GNP residues after the reaction, i.e. Na^+, Cl^-, remain in the basic fluids, the conductivity of unpurified GNP dispersions will be increased and cause a dependency on the concentration. Those residues have significant influence on the permittivity and RF heating effects. The alteration in the permittivity has been proved by our test. An effective conductivity of the highest concentration at 1.6 ppm is 0.0325 S/m at 100 MHz and its DC conductivity is 0.0266 S/m tested by a DC conductivity metre. Considering the RF heating effect, a CST simulation presents that the temperature rise is 0.5 K that matches the test, which is done by diluted NaCl liquid at the same DC conductivity of 0.0266 S/m at 100 MHz.

As a result, the dielectric test does not support significant temperature increase triggered by GNPs absorbing RF irradiation. The little temperature increase of purified GNP dispersions is not able to be credited as the evidence that GNPs can rise the SAR. The temperature increase of unpurified GNP dispersions is mainly caused by the non-GNP residues. Moreover, according to our investigation, the field strength of 16 kV/m might not be correctly estimated in some previous literatures and this deserves further investigation (Cardinal et al., 2008, Gannon et al., 2008, Moran et al., 2009).

Joule-Heating

A Joule-heating model was proposed to explain the temperature increase (Moran et al., 2009). Base on this model, the heating rate of the bulk fluid can be written as

$$\frac{dT}{dt} = \frac{\sigma(\omega) \cdot n \cdot a \cdot d \cdot \left|\vec{E}\right|^2}{VC_w}, \qquad (4\text{-}6)$$

where σ is the conductivity of Au, n is the number of GNPs, a is the cross section of a gold nanoparticle, d is the diameter, $\left|\vec{E}\right|$ is the field strength in the host water, V is the volume of the GNP dispersion, and C_w is the heat capacity of water. This model can also be utilised to clarify the size-dependent heating effect of GNP fluids and it is stated that GNPs in small size can be heated up faster. On the other hand, this mode cannot be accurate because of some reasons. Firstly, nad/V in (4-6) is 1.5 times the volume fraction of GNPs in the nanosuspension, suggesting that there is no size dependent effect if the volume fraction stays the same. Secondly, the field strength in the equation is incorrectly used as the field in the host water rather than the field inside the GNPs, which is many orders of magnitude lower because of the larger conductivity of Au than water. Utilising the right field strength value, see Appendix I, Eq. (4-6) expects that the

bulk temperature rise should be in the scale of 10^{-18} Celsius rise in temperature over 180 seconds for the highest GNP concentration employed in their studies. Regarding our case, the expected value should be in the same scale of 10^{-18} Celsius over a period of 600 seconds for the concentration of GNP dispersions at 1.6 ppm. As a result, the Joule-heating mechanism cannot be right and cannot clarify the results in previous publication (Cardinal et al., 2008, Gannon et al., 2008, Moran et al., 2009).

Mie's theory

Recently, Hanson's group studied the mechanism of heating effects by classical Mie's theory and quantum mechanism. According to Mie's theory, the energy of EM waves absorbed by GNPs is very tiny below the low THz regime. The theory also suggests that at a frequency of 1.7 THz the heating contribution from phonon is much smaller than that from electron-hole pair at the surface, not mentioning the frequency range in our study is much lower. As a result, the quantum mechanism indicates that the GNPs are not responsible for the significant EM energy absorption.

In the higher frequency region, i.e. visible or NIR range, the interaction between photons and GNPs is attributed to the surface plasmon resonance (SPR) effect, and can be well explained by the classical Mie's theory (Kerker, 1969). This interaction requires that the periphery dimension of a GNP is comparable to the wavelength of light at visible or NIR spectrum. The matching between the size of particles and the wavelength is the fundamental requirement of resonance.

Electrophoretic Particle Acceleration

The theories mentioned earlier, including the effective medium theory, Joule-heating

model and the Mie's theory can not explain well why GNPs are able to rise SAR and increase the bulk temperature at the low RF frequency of 200 KHz, 400KHz and 13.56 MHz. Hence, alternative theory is required to explain the heating effects of GNPs at the frequency range.

Very recently, Sassaroli et al. (2012) and Corr et al. (2012) proposed their theoretical and experimental evaluations suggesting that the heating mechanism can be interpreted by the electrophoretic oscillation of charged GNPs across finite length scales in response to a time-varying low-frequency electromagnetic field (Corr et al., 2012, Sassaroli et al., 2012). The results showed that the heating mechanism is dependent on the GNPs size, concentration and surface area (containing the concentration of citrate coating), and the heat production is remarkably reduced as the GNPs are aggregated.

In our case, GNPs behave like negatively charged particles because of the existence of the negatively charged citrate-capping layer on the surface. The movement of the GNPs can be expressed by the equation given by Sassaroli et al as following.

$$\nu_0 = \frac{qE0}{\beta}\frac{1}{1+i\omega\tau} \quad (4\text{-}7)$$

where ν_0 is velocity of the charged GNPs, q is the nanoparticle charge, E_0 is the amplitude of applied electrical field, β is the friction coefficient given by Stoke's law ($\beta = 6\pi\mu_f a$ where μ_f is the coefficient of viscosity of the host medium and a is the GNP radius), τ is equal to m/β (where m is the GNP mass), ω (2πf) is the angular frequency.

Then the power loss can be calculated from the following equation, based on the assumption that the heat generated is from the electrophoretic oscillation of charged GNPs.

$$P = IV = \mathcal{N}qv0(\omega)|E| \quad (4\text{-}8)$$

where P is the power (W), I is the current (A), and V is the voltage, N is the number of NPs per unit volume, E is electric-field strength (V/m). This relationship can be used to give the theoretical increase in temperature:

$$P \Delta t = mc \Delta T \quad (4\text{-}9)$$

$$\frac{\Delta T}{\Delta t} = \left(P \frac{\Delta t}{mc}\right) = P/mc \quad (4\text{-}10)$$

Where m is mass of sample (kg), C is Specific Heat Capacity that is the sample-specific heat capacity calculated as a mass weighted mean value of GNPs and water. The heat-capacity of GNPs is negligible due its low concentration, and thus a heat capacity for water (4.18 J g^{-1} K^{-1}) is taken as the sample's heat capacity (Motoyama et al., 2010, Ghosh et al., 2011).

From the equations above, Sassaroli et al. also deduced the expression of dielectric loss as a function of the motion of charged particles in response to a time-varying electromagnetic field at low radiofrequency.

$$\varepsilon''_{flow} = \frac{\mathcal{N}q2}{\beta\omega\varepsilon_0} \frac{1}{1+(\omega\tau)^2} \quad (4\text{-}11)$$

According to the above equation, the dielectric loss of GNP suspensions decreases as the frequency ω increases, which is what has been observed in our experiments, i.e. the temperature increase at 200 KHz was higher than that at 400 KHz, and the heating effect at 400 KHz was higher than that at 13.56 MHz.

A main effect on the microwave (MW) heating should present on the GNP dispersions, rather than that of the base fluid. It is not easy to analysis if water could cause enough

interaction between electromagnetic waves/field and GNPs to take effects. Dielectric loss dominates the microwave heating effect in our case. The experiment results of dielectric loss of GNP dispersions and DI water were in very small difference. This result is also similar to our MW heating result where there was only small difference between DI water and GNP dispersions. A similar example of microcapsules with GNPs absorbing microwave irradiation at 2.45 GHz was reported (del Mercato et al., 2011). Their results showed that the morphology of microcapsules with GNPs were deformed after microwave exposure compared to capsules without GNPs. Microwave heating effects of GNPs were presented in strong local surface defects and finally lead to collapse of microcapsules after 4 minute MW exposure. The heating effect of water under the same MW irradiation was also reported in their study. The wall of the capsules without GNPs is destroyed via vibrations of the molecular dipoles of water after 10 minute MW exposure. The result suggested that GNPs is able to absorb MW irradiation and rupture capsules for a short period of time.

Regarding the result of the research using GNPs under EM field at microwave frequency (Ghahremani et al., 2011), cell survival rate was used to present the effectiveness of microwave hyperthermia with GNPs. The highest concentration at 26.4 mg/ml of 40 nm GNPs presented the most effective result as the survival rate dropped down to 4.1%, which meant the heat was generated locally and focused in the cell due to existence of GNPs. The other investigations were reported to avoid water effect, for example Mashal group used jelly-like breast tissue mimicking material, and Cook group used real Porcine Muscle (Mashal et al., 2010; Cook et al., 2010). Further investigations are required to understand the mechanism and avoid water effect to reveal the gold effect in this sense.

4.6.3 EM heating at visible light spectrum

As mentioned earlier, in the visible or near-infrared region, the mechanism of thermal enhancement by GNPs is owing to the surface plasmon resonance (SPR) effect, which can be interpreted by the classical Mie's theory (Kerker M., 1969).

When the UV-Vis absorption band of GNPs overlaps the wavelength of incident light, it is able to cause the excitation of surface plasmon. Plasmon resonance is a collective oscillation of a large number of electrons. The overlap between the absorption band of GNPs and the electromagnetic wavelength is the basic demand of resonance. A research related to heat generated by metal nanoparticles under laser irradiation was reported by Govorov et al., who proposed that the local temperature around a single spherical nanoparticle in water can be described by a simple equation:

$$\Delta T(\mathbf{r}) = \frac{V_{NP} Q}{4\pi k_0} \frac{1}{\mathbf{r}} (\mathbf{r} > R_{NP}) \qquad (4\text{-}12)$$

Where V_{NP} is the NP volume, k_0 is the thermal conductivity of water, r is the distance from the center of an NP, Q is the heat generation. This equation is valid outside the NP, i.e. $r > R_{NP}$, where R_{NP} is the NP radius. The surrounding medium also can be changed to a chemical solution, or a polymer.

In our heating experiment of different nanomaterials, gold nanocages showed the most effective laser heating due to the overlapping of laser wavelength (655 nm) with the absorption band of gold nanocages with an absorption peak at 670 nm. The heating effects of GNPs and Au plates could be observed, but not as good as Au nanocages. And comparing the heating effect of GNPs and Au plates, the latter one was better. As

the heating effect for different nanomaterials were measured at the same concentration, the differences of heating effect originate from the different overlapping extent of their absorption band with the laser wavelength. The absorption band of GNPs and Au plates only partly match 655 nm laser (Figure 4-38).

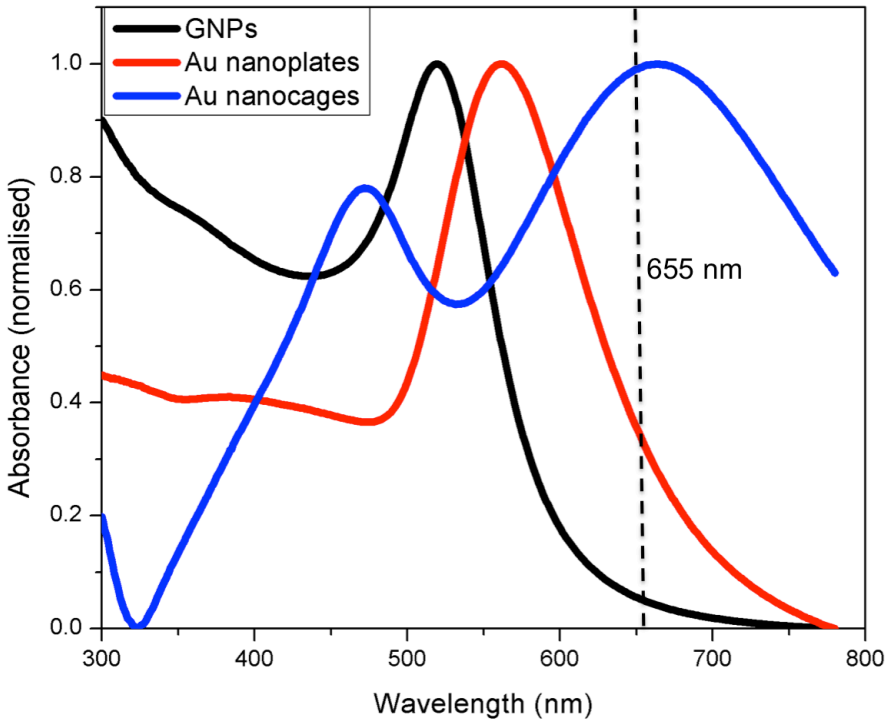

Figure 4-38 The absorption band of GNPs, Au plates and Au nanocages

In this case, Au nanomaterials can absorb light and convert it to heat, thus the understanding of the effects of various Au nanomaterial on the photothermal conversion efficiency is very important. The temperature of the gold nanoparticle can be assumed to be the same as the temperature of surrounding fluid, which is measured by the optical fiber. The photothermal conversion efficiency (η) can be calculated by:

$$\eta = \frac{(c_w m_w + c_n m_n)\Delta T}{IA\Delta t} \qquad (4\text{-}13)$$

where c_w and c_n are the specific heat of water and gold respectively, m_w and m_n are the mass of water and gold respectively, ΔT is the temperature increase in a Δt time interval,

I is the laser intensity, and A is the illumination area of fluid in the experiment. When the particle concentration is very small, i.e, $\frac{c_n m_n}{c_w m_w} \sim 0$, the photothermal conversion efficiency can be simplified as:

$$\eta \approx \frac{c_w m_w}{IA} \cdot \frac{\Delta T}{\Delta t} \qquad (4\text{-}14)$$

The photothermal conversion efficiency is proportional to the temperature increase rate. The photothermal conversion efficiencies of 3 different Au nanomaterials at the same concentration of 1.6 ppm are calculated, shown in Figure 4-39. The initial temperature rise rate during the first 300-seconds was taken as an example as the heat leak was negligible. The conversion efficiency of Au nanocages achieves 85%, which is more than twice of the efficiency of GNPs.

The enhancement ratios of the photothermal conversion efficiency of gold nanomaterials at 1.6 ppm comparing to the base fluid are presented in Figure 4-40. Significant enhancement was observed for gold nanocages and this enhancement ratio reached 120%. Remarkable heat can be generated through the surface Plasmon resonance process (SPR), where the absorption from the nanoparticle could be greatly enhanced via the coupling of the incident light with the collective oscillation of electrons in metal. Similar results were obtained in Au nanorods with different absorption peak under 808nm laser done by Chen et al. As the absorption peak was shifted away from the laser wavelength, the extinction value and the light absorption at the laser wavelength became smaller, resulting in the reduction of temperature rise (Chen et al., 2010).

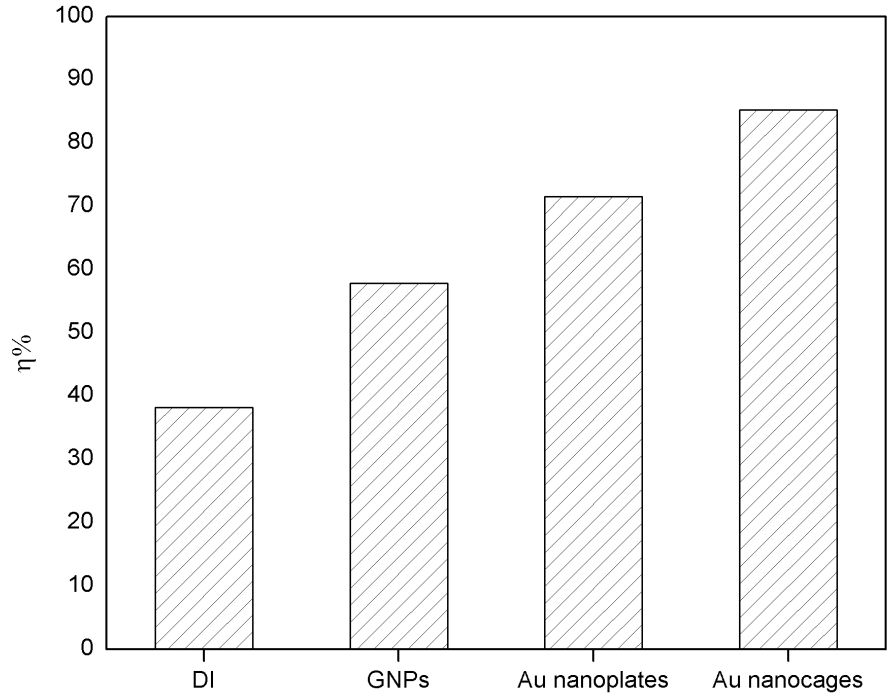

Figure 4-39 Photothermal conversion efficiency of gold nanomaterials at1.6 ppm under 655nm laser

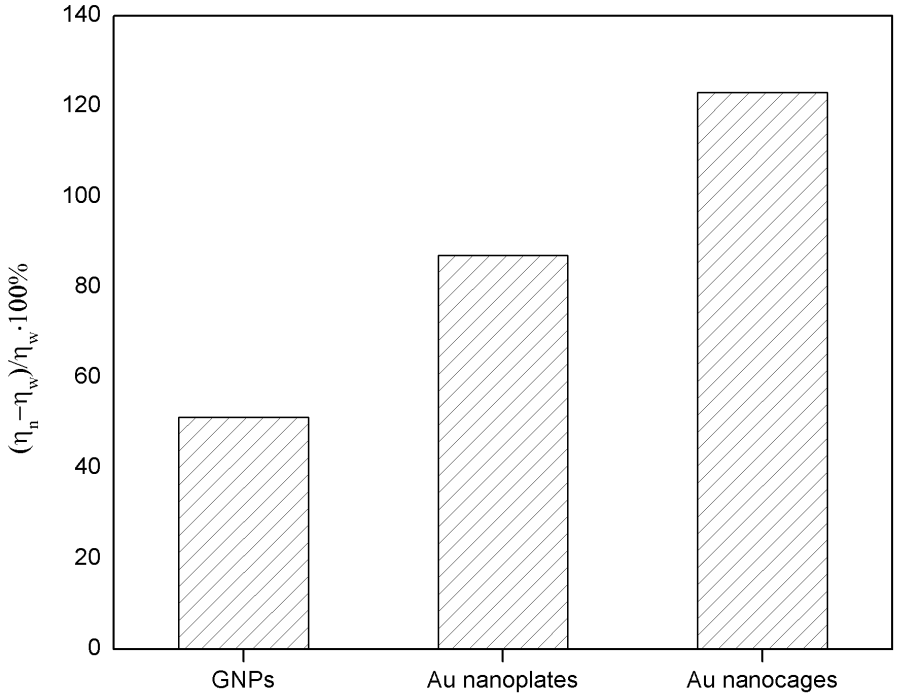

Figure 4-40 Enhancement ratio of the photothermal conversion efficiency of Au nanomaterials comparing to the base fluid

The difference of the temperature increase versus the plasmon wavelength can be attributed to the change in the extinction coefficient at the laser wavelength. The extinction of metal nanoparticles is donated by both the absorption and scattering. Only the absorbed light can be converted into heat.

Gold dispersions could obtain the highest temperature increase as the plasmon resonance wavelength was equivalent to the illumination laser wavelength. The conversion efficiency is related to the effect of the fluid thickness on the volumetric absorption from gold nanomaterials. The absorption efficiency of each particle shall be different at different fluid depth. Moreover, the radiation heat transfer between nanoparticles should be considered carefully. It should be pointed out that the concentrations of used GNP dispersions are very low in the experiment and the gold nanomaterials are uniformly dispersed in the base fluid. A simple estimation presents that the l/d value, the ratio of the particle-particle distance to the particle diameter, is in the range of 10~100. It is reasonable to consider that the particle–particle interaction should not be important. Since the l/d ratio is very large within the whole experimental range, the radiation among particles is the main mechanism for particle-particle interaction. The interactions may be reinforced when the particle concentration is over a certain value, which may lead to higher nanoparticle temperature, and increase the heat loss to the environment by particle radiation. Clearly further fundamental study is required on the particle-particle interaction to understand the mechanisms.

4.7 Chapter summary

The heating responses of gold nanoparticle dispersions under different forms of energy, including ultrasonic field, electromagnetic field at radiofrequency (200 kHz, 400 kHz, 13.56 MHz, and 2.45 GHz), and electromagnetic field at the visible range are studied for potential non-invasive thermal therapy applications.

1. The heating experiments under the ultrasonic field showed that GNPs can increase the heating rate significantly. This opens a promising window for nanoparticles, especially GNPs, for ultrasonic medical applications.

2. Under EM field at low frequency of 200 kHz and 400 kHz, the purified GNP dispersions can generate an appreciable bulk heating effect, with a non-linear relation between the temperature increase and GNP concentrations; while the heating effect of impurity has been discovered to be negligible. The heating response of gold nanoparticle dispersions under low frequency EM is suitable for potential non-invasive thermal therapy applications.

3. Under EM field at a frequency of 13.56 MHz, the impurities contribute much more to the heating effects than GNPs do. An increase of only 0.3 K was observed for pure GNP dispersions with our in-house built system, while a temperature increase of 4.5K was obtained for pure GNP dispersions with the Kanzius RF system. The application of nanoparticle-assisted hyperthermia under 13.56 MHz needs to be further investigated.

4. Under EM field of high frequency of 2.45 GHz, the heating effect of GNP dispersions cannot be identified because the water as the base fluid has too strong

absorption at this frequency. This frequency range might not be appropriate for use in the hyperthermia.

5. Under EM field at the wavelength of 655 nm, gold nanocages are found to have remarkable performance in improving the photothermal conversion efficiency and in microcapsule deformation. The result illustrates the possibility of the Au nanomaterials being used for local hyperthermia and drug release applications.

6. Many mechanisms have been proposed to explain the heating effects of nanoparticle dispersions under different EM fields. At the region from radiofrequency to microwave (kHz to GHz), the heating mechanism can be relatively well interpreted by the electrophoretic oscillation of charged GNPs in response to a time-varying low-frequency electromagnetic field. The dielectric loss (ε″) calculated from this electrophoretic theory shows higher value (more energy loss and thus higher temperature increase) at lower frequency. At high frequency from visible to near infra-red region, the heating effect can be explained by the surface plasma resonance mechanism.

Chapter 5 Cells and Cellular Uptake

GNPs have received many attentions for their potential uses in biomedical fields such as drug or gene delivery, diagnostic imaging, and thermal therapies due to their excellent biocompatibility and easy conjugation to various biological molecules. The GNP –mediated thermal therapy heated by noninvasive irradiation would be a future prospective strategy for targeted hyperthermia to cancer. Many investigations have been carried out for non-invasive GNP –mediated thermal therapy in numerous scientific fields, such as chemistry, engineering, physics, biology and medical. Various GNPs have been designed for different thermal therapy and shown varied efficiency. For example, gold nanocages have been used for NIR-laser treatment and have caused effective destruction of breast cancer cells (Au et al., 2010). GNPs have been employed in noninvasive radiofrequency hyperthermia to induce cell death (Raoof et al., 2012). Functionalized gold nanorods have been used for laser therapy to damage cancer cells (Cabada et al., 2012; Huang et al., 2011). Thermal injury was caused in different cancer cells through various thermal treatments. However, prior to their application in the clinical practice, careful consideration should be given to the possible influencing parameters, such as power and treatment duration.

In this chapter, both *in vitro* (B50 cell) and *in vivo* (fruit fly) biocompatibilities of the GNPs have been studied. The GNP-mediated photothermal treatment of B50 cells has been investigated and aiming to understand the effect of GNPs mediated photothermal treatment *in vitro*.

5.1 Experimental Method

B50 cells, derived from the rat neuronal cells with neuronal morphology, were purchased from European Collection of Animal Cell Cultures (ECACC, Porton Down, UK). These cells were isolated from the rat central nervous system that maintains morphological and chemical characteristics of the neural cells. Some researches have employed these cells as the subject for understanding cytotoxic effects (Bottone et al., 2008; Santin et al., 2012) and cellular uptake (Pavlov et al., 2011). B50 cells were cultured in the Dulbecco's minimum essential media (DMEM, Sigma-51435C) supplemented with fetal bovine serum (FBS, 10% v/v, Sigma-F2442), L-glutamine (0.1% v/v, Sigma) and penicillin- streptomyosin (1% v/v, Sigma) in a 5% CO2/95% air humidified atmosphere at 37 °C (Mayne et al., 2000).

In order to examine the biocompatibility of GNPs, B50 cells were incubated with DMEM containing 1.6 ppm GNPs. GNP suspensions were centrifuged at 13500 rpm to remove surfactant and re-suspended in the DMEM. Before the incubation, DMEM contained GNPs were characterized by UV-vis absorption spectrometer. B50 cells were cultured with GNPs suspended in DMEM for 48 hours. After that, the samples were washed from the incubation medium for cell count assay. After uptaking, UV-vis absorption was again measured for the cells. B50 cells without GNPs were used as the reference group in this test.

The cells used for confocal fluorescent observation were incubated with GNPs at 1.6 ppm for 24 hours instead of 48 hours, and corresponding images were captured by CLSM. The fluorescent GNPs were prepared by adding aqueous solution of TRITC-dextran to GNP suspensions at 1.6 ppm to reach a final concentration at 50 μM of

TRITC-dextran for CLSM studies. The fluorescent GNP suspension was kept in dark at 4 °C for 12 hours to avoid TRITC-dextran deactivation caused by light and heat. The fluorescent GNP solutions were washed twice by centrifugation at 6000 rpm for 20 minutes to remove free TRITC-dextran molecules. The TRITC-dextran-bound GNPs were re-suspended in DMEM and then cultured with cells for next 12 hours. Before CLSM studies cells were washed out the incubation medium and stained with the green dye DiOC18(3).

The cells used for GNPs mediated laser treatment were cultured in DMEM containing 1.6 ppm unmodified GNPs for 24 hours. Cells were then separated from the incubated DMEM and rinsed by fresh DMEM, which allowed the removal of the excessive GNPs that were not taken up by the cells. Cells were then exposed to CW laser light at various laser durations. The laser spot at 655 nm was focused by a lens (fZ8 cm) to reduce the spot size to 0.5 mm^2， as shown in Figure 5-1. After the laser irradiation, samples were examined by the optical microscopy.

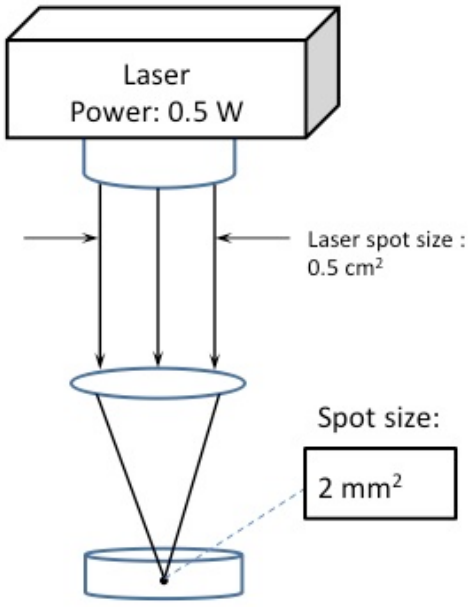

Figure 5-1 Schematic diagram of the laser treatment system

To examine the *in-vivo* biocompatibility, fruit flies were used in this study and raised in cages with overlapping generations on a cycle of 12-hour light/dark at 25 ℃ and 65% humidity. Fruit juice agar plates were prepared as a standard sugar/yeast food (6% sucrose, 10% yeast, 1.5% agar) with or without GNPs. GNPs at a concentration of 1.6 ppm were added and mixed with the food before the congealment. Living flies count assay was performed on days 1, 7, 14 on both experimental and control groups.

5.2 Results and discussion

The UV-vis spectra of GNPs in DI water (red curve) and in the DMEM (black curve) are presented in Figure 5-2. A strong absorption peaks in red curves in 520 nm is assigned to the excitation of surface plasmon vibrations in GNPs. A strong peak of GNPs in DMEM is red-shifted by 10 nm to 530 nm because of the alteration in refractive index for the DMEM. The absorption peak of GNPs in DMEM is located at 530 nm remains a sharp peak revealing that the GNPs are well suspended in the DMEM. Similar results have been reported by the Xia's Group when the anti-EGFR Au nanocages were transferred into a culture medium (Au et al. 2011).

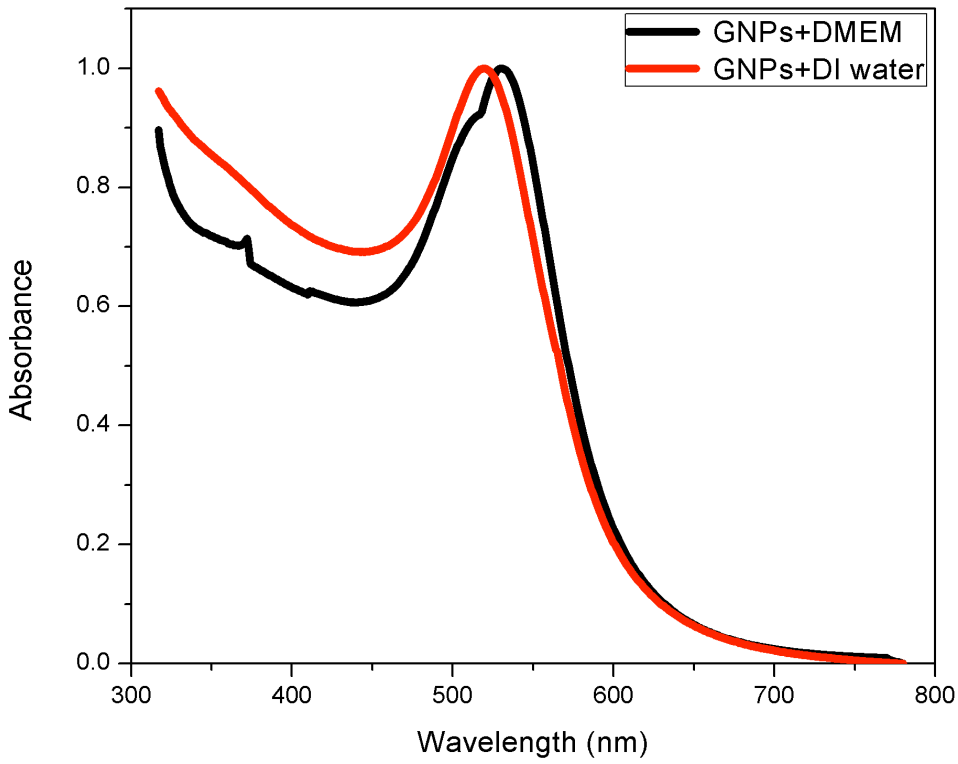

Figure 5-2 UV-vis spectra of GNP dispersion and GNPs suspended in DEME solution

Figure 5-3 shows the UV-vis test result of B50 cells incubated with GNPs for 48 hours. The cells were separated from the culture medium by the centrifugation at 1500 rpm for 5 minutes. Low speed of centrifugation at 1500 rpm cannot damage cells and was sufficient to separate GNPs that are remained in the culture medium. The absorption spectrum shows a broad distribution with a red shift when GNPs were taken by cells, indicating some aggregation of GNPs in cells.

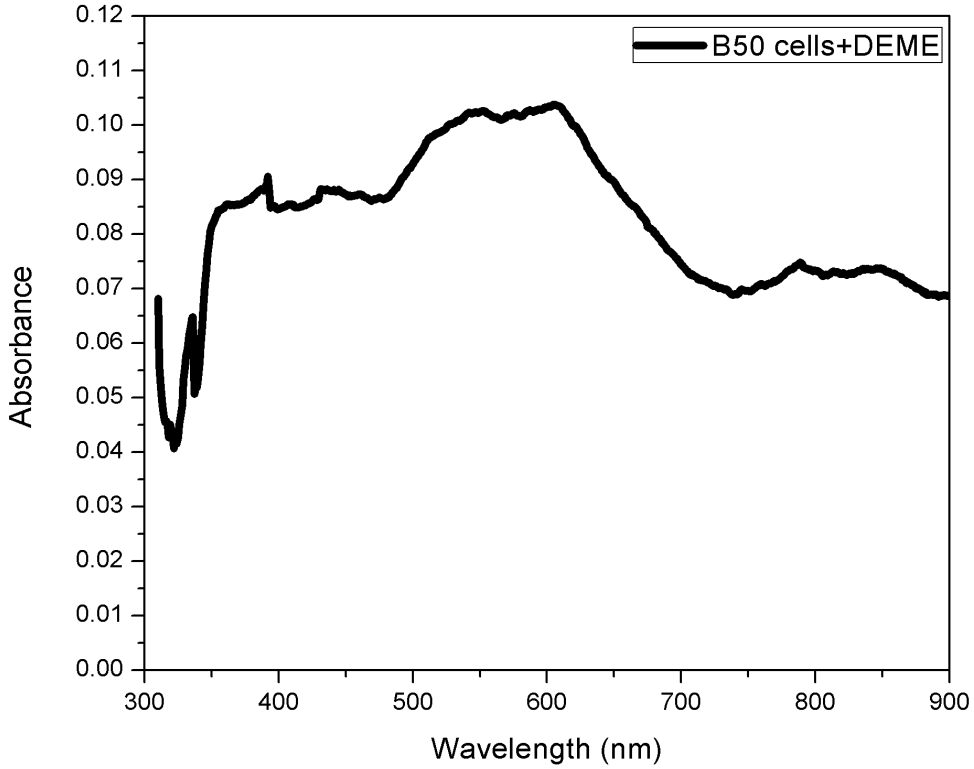

Figure 5-3 UV-vis spectra of B50 cells incubated with GNPs for 48 hours

The size of aggregated GNPs (red spot) is about 300 nm in the confocal image shown in Figure 5-4. The confocal image of the B50 cells after the incubation for 24h with GNPs shows that GNPs that the cells internalize GNPs. It can be seen from Figure 5-4a that the fluorescent-labeled B50 cell is in green colour while in Figure 5-4b, dye-labeled GNPs are in red colour. In this way, we can distinguish GNPs and cells to investigate the distribution of GNPs in B50 cells by using different fluorescence dyes. Figure 5-4a shows FTIC channel from B50 cells (FTIC-dextran) and Figure 5-4b shows TRITC channel from GNPs (TRITC-dextran), whereas Figure 5-4c is the transmission image taken from the respective region. Figure 5-4d is the overlapping of the green, red channels and transmission images, which shows the location of GNPs.

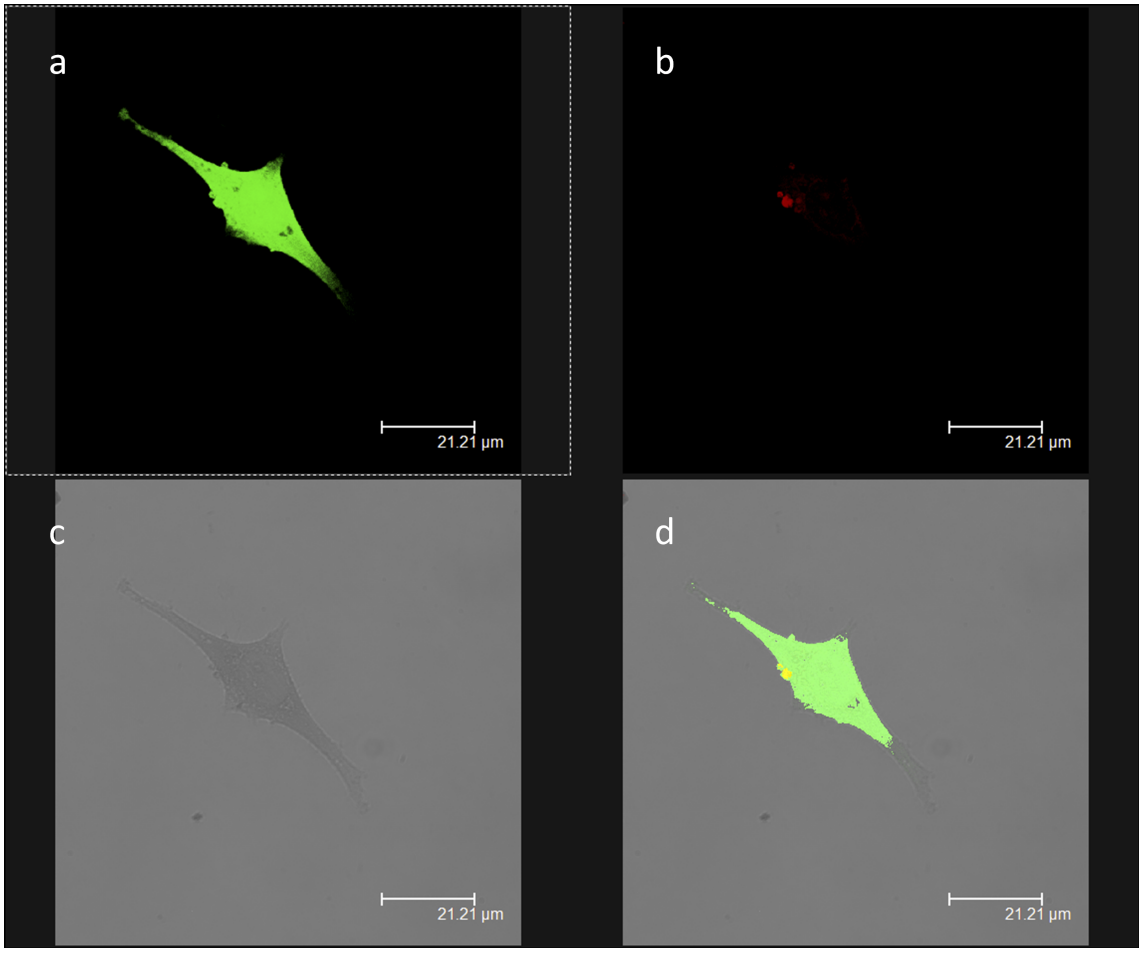

Figure 5-4 confocal images of B50 cells cultured with GNPs for 24 hourse

Figure 5-5 is the control group, which presents B50 cell incubated with the DMEM (without GNPs) for 48 hours. . Compared with the images in Figure 5-4, there is no red signal observed as the TRITC channel is used to detect the sample in Figure 5-5b. Figure 5-5d presents the overlapped cells images.

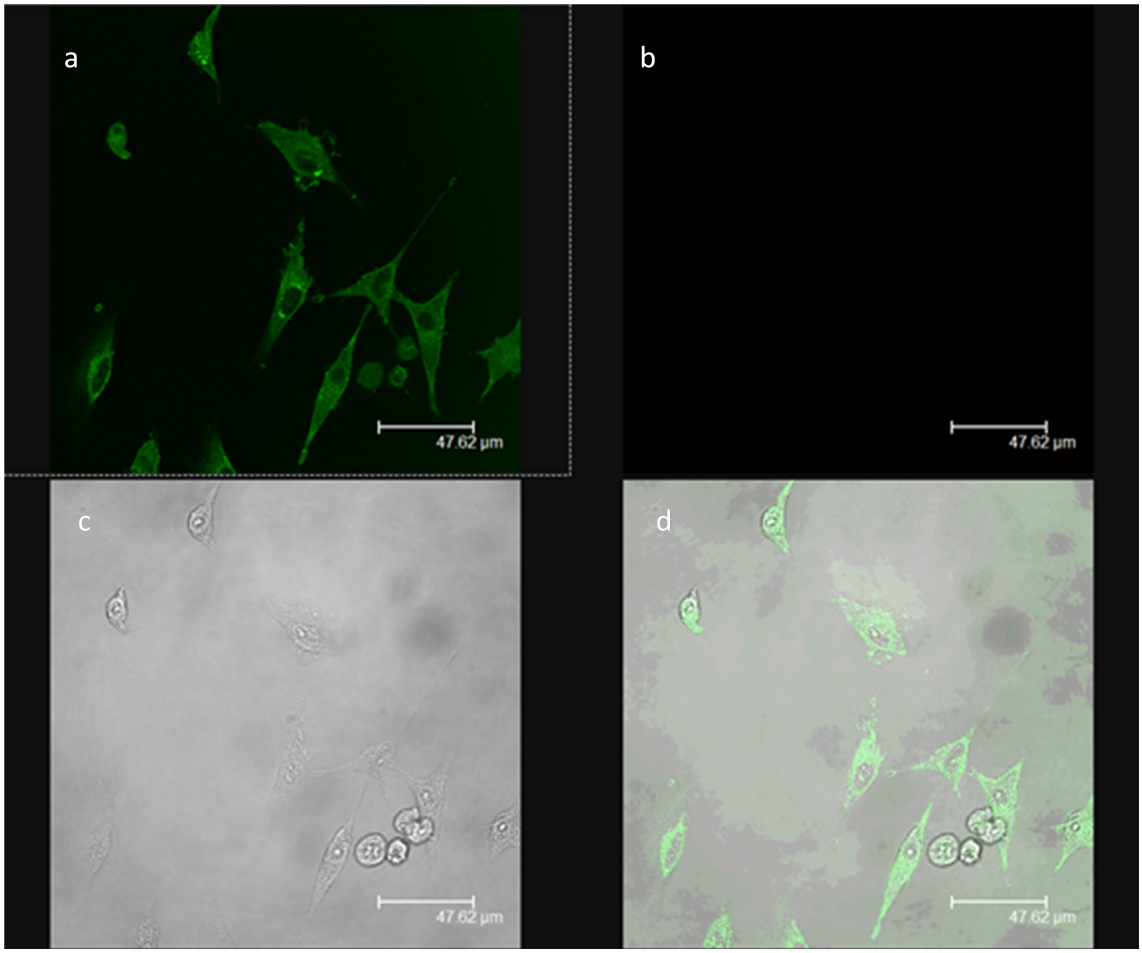

Figure 5-5 confocal images of B50 cells alone

Similar studies associated with the cellular uptake have been done by Pernodet's, Shah's, Lund's and Tasi's groups, and GNP aggregation inside cells has been observed in their results (Pernodet et al., 2006; Shah et al., 2010; Tasi et al., 2008). During the incubation process particles entered cells after few hours and appeared accumulation after 24 hours. In this study, freshly prepared GNPs without surface coating were untaken by cells via the phagocytosis process, which is based on nonreceptor-mediated endocytosis. A research has been done by Zhang's group suggesting that cells' uptake nanoparticles through the nonreceptor-mediated endocytosis is slower than through receptor-mediated endocytosis (Zhang et al., 2002). On the contrary, some other studies used PEG or folic acid as a receptor media to modify the surface of nanoparticles in

order to improve the cell internalization (Zhang et al., 2002; Au et al., 2011; Pernodet et al., 2006; Shah et al., 2010; Lund et al., 2011). Lund et al. have investigated the uptake of various hydrophilic mono- and dual-ligand GNPs in colorectal cancer cells in *vitro.* The results showed the uptake rate is related to the structural organization of the ligands on the particle surface rather than their charge or chemical properties (Lund et al., 2011). However, possible surface modification might interfere the real cell uptake effect of pure GNP. Thus, in this study GNPs without any surface conjugation modification have been used. The incubation time was increased to 24 hours for cells taking enough GNPs.

The GNPs taken up by cells via the phagocytosis process would cause aggregation since cell membrane was activated to create a vesicle, surrounding these GNPs gradually when they were attached to membrane. Thus, the GNPs were clustered in the vesicle as they were internalized. An analogous research related to the celluar uptake of GNPs without surface modification also showed GNPs were aggregated in the vesicles in the cytoplasm and the diameter distribution of these vesicles is around 200-300 nm (Nativo et al., 2008; Raoof et al., 2012), which is similar with our results shown in Figure 5-4. The author also proposed that GNPs were not selective for the endocytosis of different cells because GNPs did not have any surface functionalization thus did not undergo a process of specific antireceptor link with specific receptor (Tsai et al., 2008). For example, the uptake speeds of GNPs by the normal breast cells and breast cancer cells are almost the same. Some studies investigate antibody-conjugated GNPs uptake and showed that antibody-conjugated GNPs targeted to cell surface receptors were mainly internalized by receptor-mediated endocytosis and this process is faster than the nonreceptor-mediated endocytosis. The uptake process takes about 4 hours and intracellular GNP aggregates were observed from TEM images. These aggregates were

consistently localized in membrane-bound endolysosomal compartments. The results indicated that intracellular GNP aggregation is a universal phenomenon, observed across multiple cell lines after receptor-mediated endocytosis (Raoof et al., 2012). There results of GNP uptake have a good agreement with ours that GNP aggregation after nonreceptor-mediated or receptor-mediated endocytosis.

To investigate the biocompatibility of GNPs *in vitro* and *in vivo*, B50 cells and fruit flies were used as the subjects incubated with GNPs at 1.6 ppm for 2 days and 14 days to test their survival rates, respectively. Figure 5-6 shows the number of live cells incubated with and without GNPs after 48 hours. The cell number of both groups are very similar after 2-day incubation. At the beginning of the trial, about 265000 cells per ml were found for both the control and GNP groups. During this 2-day trial B50 cells incubated with GNPs continued to division to around 2650000 cells per ml and a large number of cell death was not observed. Moreover, the biocompatibility and cytotoxity of GNPs *in vivo* were examined by using drosophila (fruit fly) as a model because drosophila has similar metabolic functions to that of vertebrates (Wang et al., 2012). The fruit flies were kept feeding their food with and without GNPs for 14 days. Figure 5-7 presents the number of living fruit flies incubated with and without GNPs at 1.6 ppm after 1 day, 7 days and 14 days. The number of living fruit flies are maintained the same in both groups. The results *in vitro* and *in vivo* indicate that GNPs with the concentration of 1.6 ppm have good biocompatibility in both B50 cells and drosophila.

There were no short-term adverse effects on the B50 cell survival and proliferation, as well as on survival rate of Drosophila. Although no comprehensive investigations assessment for the long - term (years) toxicity of our GNPs, many other investigations

have been conducted in terms of the long term toxicity issue of GNPs. For example, Smilowitz et al. applied GNPs （AuroVist ^{TM}) in radiation treatment and the results showed that prolong survival in tumour- bearing mice. The concentrations of GNPs at 1.35g/kg and 2.7g/kg were used in combination with X-ray radiation to reduce the tumor growth. In this investigation, subjected mice were alive for 1 year after the radio treatment and no obvious long-term toxicities were observed (Hainfeld et al., 2004). In addition, gold-based pharmaceuticals have already got FDA approval and used in clinical practice. An investigation is presently in phase I clinical trials for the laser treatment of refractory and recurrent head and neck cancer using GNPs. Nanospectra Biosciences has established the AuroLase® treatment that is based on utilizing GNPs (AuroShell®) currently for Near-infrared laser. This clinical trial in patients suffering refractory and/or recurrent tumors of the head and neck is operating (Clinicaltrials.gov. 2010). Early stage clinical study using GNPs as the transducer for cancer therapy has given early signals of safety and efficacy. However, the long-term effects still need to be studied.

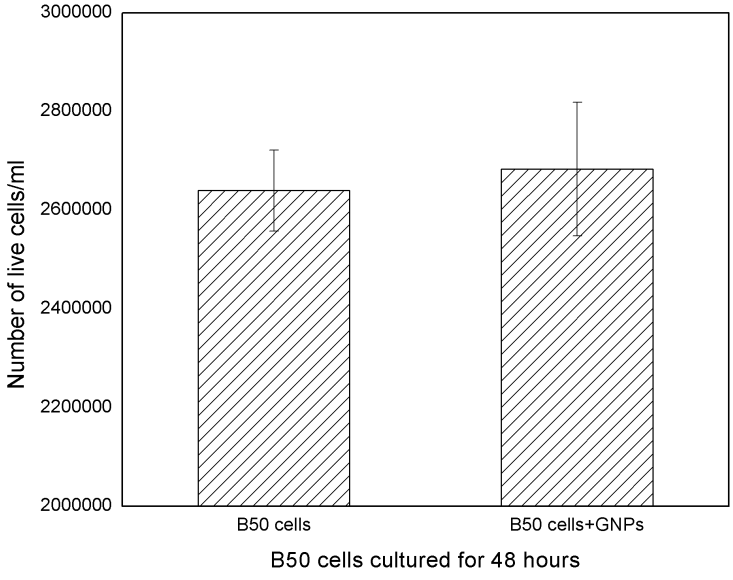

Figure 5-6 cell number of living cells with and without GNPs

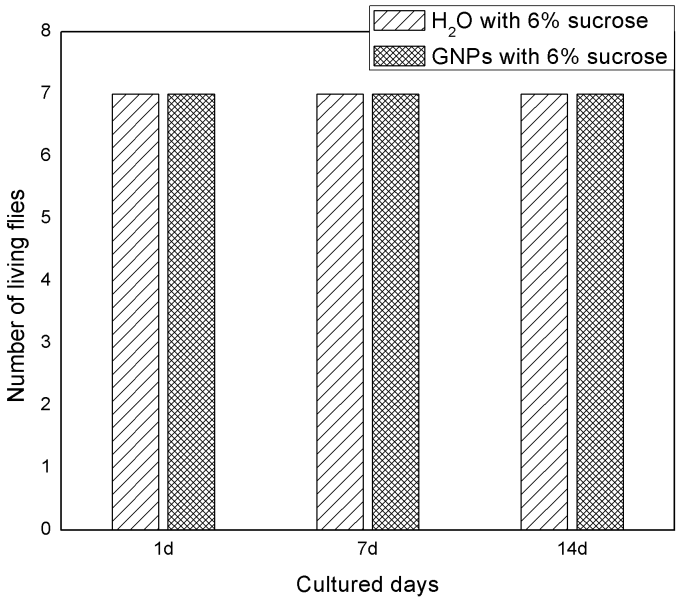

Figure 5-7 Fruit flies number with and without GNPs after 2 weeks

The images of B50 cells without GNPs after the laser treatment, where the laser power density was 25 W/cm^2 for 0, 5, 10 and 15 minutes, are presented in Figure 5-8a - 5-8d, respectively. No obvious death of cells was observed after 5-minute laser treatment. The B50 cells still adhere and remain with the neuronal morphology, shown in Figure 5-8b. After 10-minute laser exposure, slight aggregation of cells is observed (Figure 5-8c). The most of cells aggregate after the laser irradiation for 15 minutes, as shown in Figure 5-8d. It is obvious that B50 cells without GNPs addition do not show substantial cell death until 10 minutes' laser treatment. Prolonged laser treatment is therefore required to achieve a fatal effect for B50 cells without GNPs

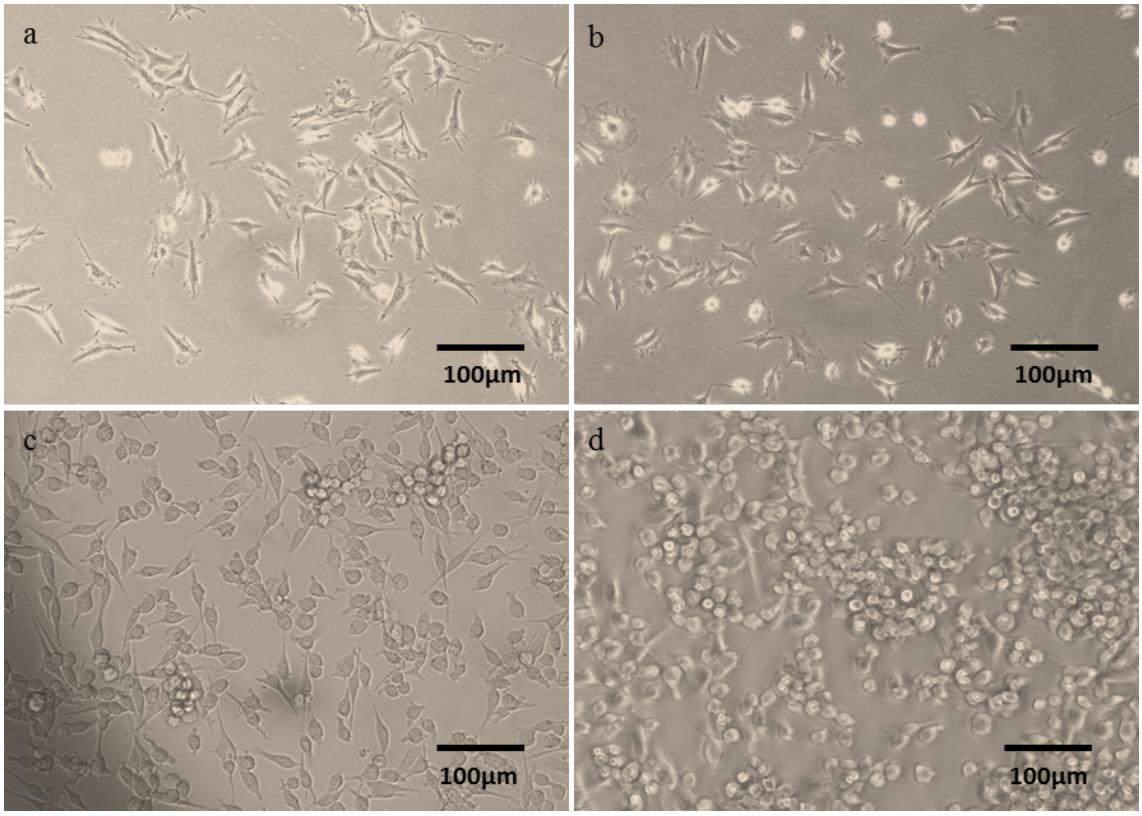

Figure 5-8 The images of B50 cells without GNPs after laser treatment for 0 (a), 5(b), 10 (c) and 15(d) minutes

After incubation with GNPs，B50 cells were exposed to laser power at the density of 25 W/cm^2 for 0, 5, 10 and 15 minutes, respectively. The morphology of the B50 cells under the laser spot changes after laser exposure to laser irradiation for 5 minutes, as shown in Figure 5-9b. As can be seen from Figure 5-9c, dead cells lose the ability to adhere on the bottom of petri dish and become round shapes, and finally aggregate after the laser irradiation for 10 minutes. Figure 5-9 d presents a significant change in the morphology of cells after a 15-minute of laser treatment. Most of the cells aggregated and suspended in the domain of the laser spot after 10- and 15-minute laser treatments comparing to B50 cells with GNPs without laser exposure, shown in figure 5-9a. The cells without laser treatment adhere on the bottom of the petri dish, where the cells are flat and the morphology can be seen clearly, as shown in Figure 5-9a. The cells become

detached from the bottom of the petri dish, aggregate and suspend in the culture, when the cells are injured by laser irradiation. It is clear from Figure 5-9b to 5-9d that round dark parts are aggregated death cells and the cells outside the laser spot still adhered on the bottom wall. Figure 5-9b to 5-9d focus on aggregated cells thus adherent cells cannot be observed clearly because they are not in the same focus. It was observed that the B50 cells with GNPs suffered significant photothermal destruction as the laser power density was at or higher than 25 W/cm^2 for 5 minutes.

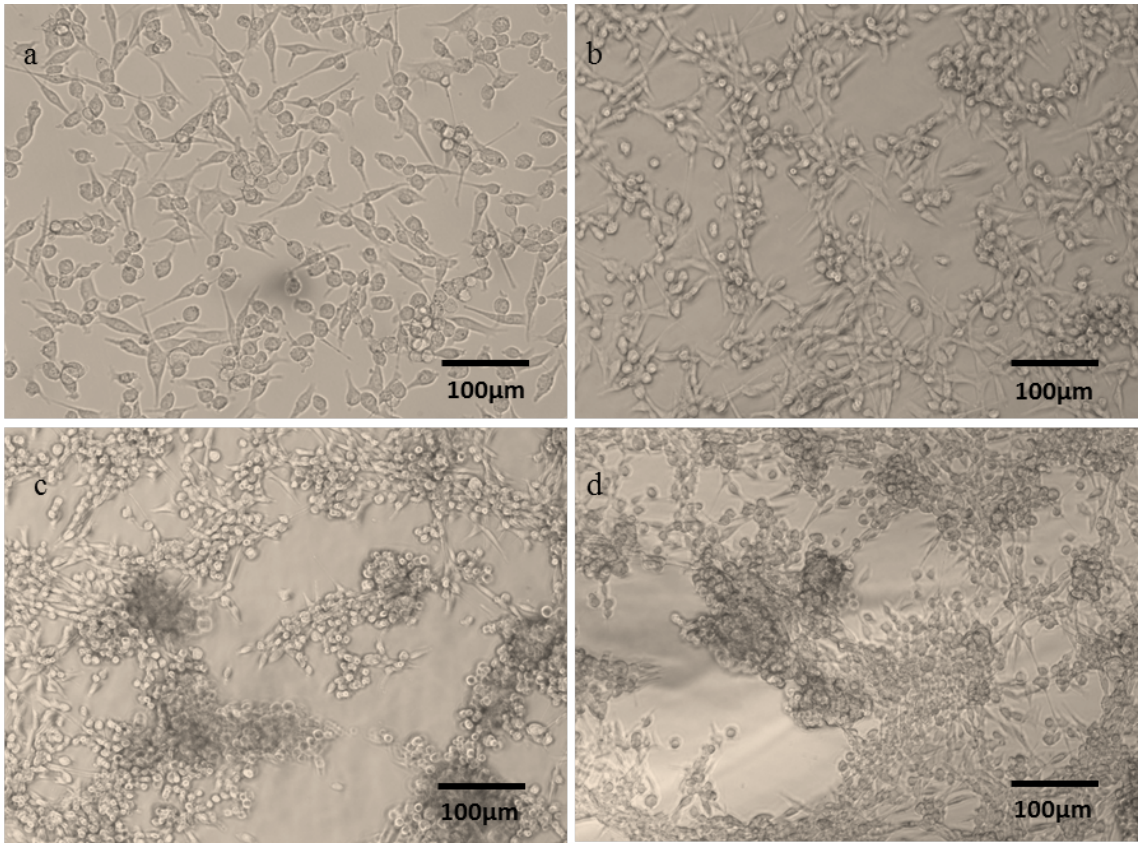

Figure 5-9 The images of B50 cells with GNPs after laser treatment for 0 (a), 5(b), 10 (c) and 15(d) minutes

This experiment demonstrates that GNPs can induce significant cell injury and death via converting light into thermal energy. It was studied that cancer cells with GNPs were damaged by laser radiation at 514 nm. The cell death increased significantly compared

to that without GNPs after exposed to laser irradiation (El-Sayed et al., 2005). However, El-Sayed's study did not consider that the absorption band of GNPs were red shifted after cellular uptake. In our study cautions have been taken to measure the absorption band of GNPs after cellular uptake. It is more precise to choose the right laser to induce the effect photothermal treatments when the absorption band of GNPs is detected. For example, in this study laser energy at 25 W/cm^2 for 5 minutes was taken to cause thermal damage in B50 cells with GNPs whereas 25 W/cm^2 for 10 minutes was used to cause thermal injury in B50 cells without GNPs. The duration to cause thermal injury would be reduced in the target site by matching the laser wavelength with the abortion band of GNPs after uptake. Later, a similar research related to 800 nm laser therapy using Au nanorods as an agent to adopt laser irradiation. The absorption band of Au nanorads after cellular uptake was measured to overlap laser wavelength at 800 nm in this research. Photothermal injury was caused in HSC and HOC after exposure to the laser at 10 W/cm^2 for 4 minutes (Huang et al., 2006). Recently, a laser ablation investigation showed that SKOV3 cells with the antibody targeted GNPs were destroyed by a continuous wave laser at 38 W/cm^2 for 5 minutes (Broek et al., 2012). The threshold energy to damage the B50 cells with GNPs in our study is found to be 25 W/cm^2 for 5 minutes. In this point cells with GNPs were damaged meanwhile cells without GNPs were not harmed at 5-minutes of laser treatment. The energy threshold for cell death reported by Huang's group is lower than that of ours. Some reasons might cause this difference: 1) different cell type required different energy threshold to cause thermal injury; 2) different morphology of nanoparticles have different photothermal conversion efficiency (Chen et al., 2010); 3) Huang and Broek modify the surface of the gold nanoparticles with the antibody to target specific molecule on the cell surface

resulting in higher amount of nanoparticles uptake. In our study, we present a pure GNP laser ablation in B50 cells.

Photothermally caused cell death can occur via either apoptosis or necrosis, relying on the applied laser mode, dosage and irradiation duration as well as the subcellular location of the nanoparticles. Thermal injury induced by pulsed laser irradiation has been studied by Zharov et al. (2008) and shows that GNPs mediated laser treatment could produce cell injury via photothermal and accompanied phenomena, such as cell cavitation, cellular structure rupturing and evaporation of cellular liquid as well as bubble formation by shock waves. Because GNPs exposed under pulse laser irradiation would cause particle thermal expansion, evaporation, and plasma generation (Zharov et al., 2008). For continuous wave laser, Tong et al. (2007) have studied the photothermolys is mechanism of CW laser treatment and Au nanorods. Their study has presented that cell death is caused by the disruption of the plasma membrane according to staining of cell membrane integrity, cell viability and actin filaments. They also observed that subsequent influx of calcium ions induced membrane blebbing and damage of actin filaments. Thus, they suggests that apoptosis is the route of cell death by the laser heating of gold nanoparticles (Tong et al., 2007). Very recently, however, Cabada et al. (2012) suggests that cell death is necrotic rather than apoptotic because photothermal injury triggers a notable loss of cell membrane integrity. They also indicated apoptotosis is induced by the toxic effect of the CTAB coated gold nanorods (Cabada et al., 2012). In our case, we consider that cell death should be necrotic. On one hand, our GNPs are purified and free of any toxic surfactant. On the other hand, the uptake GNP clusters are close enough to the cell membrane, which will be destroyed by

the generated heat. The mechanism of cell death induced by the GNPs mediated laser treatment deserves further investigation.

Chapter summary

This study reveals that GNPs have high biocompatibility with B50 cells and easy to be taken by B50 cells and Drosophilas. Fatal death either in *vitro* and in *vivo* after uptake of GNPs was not observed in the experiments. Moreover, the applied laser wavelength should be chosen to match the absorption band of GNPs after uptake, to generate effective thermal injury effect. Lower energy is preferred to cause thermal damage in B50 cells with GNPs than the cells without GNPs in this laser treatment. GNPs present as a biocompatible optical energy absorber and that may potentially be used in photothermal therapy.

Chapter 6 Conclusions

This project is focused on the interaction between electromagnetic/ultrasound field and nanoparticle dispersions. Different gold nanofluids were produced from the one-step approach based on the citrate reduction (CR) method with the aid of ultrasonication for particle morphology control. This produced GNPs with smaller size and near spherical shape compared with the conventional citrate reduction method. The ultrasonication plays an important role in the formation and controlling the morphology of gold nanomaterials. The size of spherical GNPs can be controlled in the range of 10-20 nm, and the average size of gold nanoplates can be controlled between 50 and 150 nm, with more uniform and regular shapes. Gold nanocages can be synthesized by a galvanic replacement reaction in the presence of ultrasonication. The FTIR-ATR result showed negligible residue reactants remaining in the gold dispersions after the purification process.

The use of direct current to control GNP morphology was studied. GNPs became larger when the applied DC voltages were increased. Loose structures were formed at low voltages while large solid structures were formed at high voltages. The colour change of GNP dispersions was an indication of the size change or aggregation as the DC voltage was applied. The CIE1931 colour space can be used to quantitatively describe this colour change based on the transmission data of GNP dispersions measured by the UV-Vis spectrometer.

The interaction of the EM fields with GNPs was studied in a broad range of frequency bands, involving 200 kHz, 400 kHz, 13.56 MHz, the microwave range at 2.45 GHz and the NIR light. The bulk heating effects of GNP dispersion were investigated by

ultrasonic irradiation, microwave and radiofrequency irradiation as well as laser at the visible spectrum.

The ultrasonic heating study showed that GNP is an excellent agent to focus ultrasound irradiation. Up to four-fold increase in the temperature rise rate was observed for the GNP dispersion at a concentration of 1.6 ppm. The heating effect of GNPs was much higher than that of alumina and nickel nanoparticles. A much lower concentration of GNPs, 0.13 ppm, had similar heating effect as that of 250 ppm by alumina and 2.5 ppm by nickel nanoparticles. This opens a promising window for nanoparticles, especially GNPs, for ultrasonic medical applications. The discussion shows that possible reasons for the rapid temperature increase shall be related to the enhanced cavitation effect and modified thermal-physical properties of the base fluid.

Furthermore, the heating response of gold nanoparticle dispersions under the EM frequency of 200 kHz and 400 kHz, a spectrum that magnetic nanoparticle based hyperthermia is typically used was studied. The results showed that the effect of impurity heating at 200 kHz and 400 kHz was negligible and GNPs alone contributed to an appreciable bulk temperature increase, which increased with GNP concentrations in a non-linear fashion. The specific absorption rate of GNP was surprisingly as high as that of magnetic nanoparticles. .

The heating effect investigation at 13.56 MHz showed that the temperature increase in GNP dispersions without purification process was due to the presence of impurities. The purified GNP dispersions did not show persuasive temperature increase in the

experiments. Hence, the impact of GNPs in the heating process was unable to be recognized because large filed strength may be needed to induce sufficient temperature increase to distinguish the effect from GNPs. In addition, it also showed that the heating effect was mainly contributed by the non-GNP residuals in the Kanzius system.

The laser heating experiments showed that Au nanomaterials are efficient photothermal agents. Engineering the GNP morphology to match the irradiation wavelength is required to achieve an optimized thermal effect. Moreover, these results illustrated fundamental evidence of the possibility of using Au nanomaterials for laser-driven heating for local hyperthermia and drug release applications. It was observed that the laser induced heat to effectively rupture microcapsules embedded gold nanocages because the surface Plasmon resonance of nanocage overlapped with the wavelength of the laser.

Under the ultrasonic field, the temperature increase was originated from the enhanced cavitation effect by the nanoparticles acting as the bubble 'nuclei'. At the high frequency, i.e., from visible to near infrared region, the heating effect can be explained by the surface plasma resonance mechanism. Under the EM field at lower frequency, the bulk temperature increases at 200 kHz and 400 kHz were higher than that at 13.56 MHz and 2.45 GHz. At the region from radiofrequency to microwave (kHz to GHz), the heating mechanism could be interpreted by the electrophoretic oscillation of charged GNPs in response to a time-varying low-frequency electromagnetic field. The dielectric loss (ε'') calculated from this electrophoretic theory showed more energy loss and thus higher temperature increased at lower frequency.

The cellular uptake and cytotoxicity test revealed that GNPs have high biocompatibility with B50 cells and easy to be taken by B50 cells and Drosophilas. Fatal death *in vitro* and *in vivo* after the uptake of GNPs was not observed in the experiments. Lower energy was required to cause thermal damage in B50 cells with GNPs in this laser treatment. GNPs presented as good biocompatible optical energy absorber, which can be potentially used in photothermal therapy.

Key contributions

The key contributions from this project include:

1) An ultrasonic-aided one-step method for the synthesis of nanoparticles has successfully applied for controlled synthesis morphology of GNPs and Fe_3O_4 nanoparticles in this study. Both spherical- and plate-shaped GNPs in the size range of 10-300 nm were synthesized. The size distribution of Fe_3O_4 nanoparticles can be controlled in the range from 20nm to 40nm and well disperses in the based fluid.

2) DC voltage induced GNP aggregation has been investigated and loose structures were formed at low voltages while large solid structures were formed at high voltages. Moreover, the colour of GNP dispersions has also been changed after applying the DC voltages. The CIE1931 standard can be used to quantitatively describe the colour of GNP dispersions from the transmission data of GNP dispersions measured by UV-Vis spectrometer.

3) Heating effect of GNP dispersions has been studied under the EM field in a broad range of frequency bands, involving 200 kHz, 400 kHz, 13.56 MHz, the microwave range at 2.45 GHz and the visible spectrum at 655 nm. The effect of impurity heating at 200 kHz and 400 kHz is negligible and GNPs alone contribute to an appreciable bulk temperature increase, which increases with GNP concentrations in a non-linear fashion. By contrast, the temperature increase of GNP samples without purification was contributed mainly by the non- GNP residuals rather than GNPs alone at 13.56 MHz.

4) Engineering the GNP morphology to match the irradiation wavelength is required to achieve an optimized thermal effect at visible spectrum. The laser heating also demonstrated on effectively rupture microcapsules embedded gold nanocages because the surface plasma resonance of nanocage overlaps with a 655 nm laser.

5) GNPs is an excellent agent to focus ultrasound irradiation and the reasons for the rapid temperature increase shall be related to the enhanced cavitation effect and modified thermal-physical properties of the base fluid.

6) Cellular uptake and cytotoxicity test reveals that GNPs have high biocompatibility with B50 cells and easy to be taken by B50 cells and Drosophilas. Lower energy was required to cause thermal damage in B50 cells with GNPs in this laser treatment.

Future work

The study in this project focuses on controlled synthesis of nanoparticles and the interaction of electromagnetic fields with GNPs. However, there are many areas deserve further study. Future work may contain the following areas:

- Extended absorption band of nanoparticles, the absorption band of GNPs synthesised in this project are mainly on visible spectrum. The absorption band of GNPs can be designed and engineered to turn to the near-infrared and infrared range. Moreover, explore and investigate the interaction of GNPs and EM wavelengths at the near-infrared and infrared range as well as Terahertz. The optical properties of GNPs can be exploited for both the near infrared laser therapies and imaging applications.

- Regarding the heating effect of non-invasive RFA, it is worthy to investigate different shapes and shape of nanomaterials or composite nanomaterials. For example, GNPs size smaller than 10nm, gold nanocages, sliver micro/nanotube, hollow gold micro/nanotube and hollow gold tube well mixed with GNPs. Here, hollow gold micro/nanotube can be considered as microcontainer loaded/filled GNPs (3-5nm).

- Further investigate the release of microcapsules embedded with gold nanocages as these capsules can be deformed by the 655 nm laser. The gold cages and microcapsules have different size of cavity and can load some substance. Biodegradable polymer can be used as the shell. When the capsule deform the substance in the capsules will have first release meanwhile the substance in the cage will release into biodegradable shell and then release constantly and slowly as shell decompose. Thus, it can achieve for long-term drug release.

- This study reveals that GNPs have high biocompatibility and low cytotocity with B50 cells and easy to be taken by B50 cells and Drosophilas. There are no short-term adverse effects on the B50 cell survival and proliferation, as well as on survival rate of Drosophila. Although no comprehensive investigations assessment for the long - term (years) toxicity of our GNPs.

Reference

AL-KATTAN, A., DUFOUR, P. & DROUET, C. 2011. Purification of biomimetic apatite-based hybrid colloids intended for biomedical applications: A dialysis study. *Colloids and Surfaces B-Biointerfaces,* 82, 378-384.

ARIF, A. F. M. & YILBAS, B. S. 2008. Thermal stress developed during the laser cutting process: consideration of different materials. *International Journal of Advanced Manufacturing Technology,* 37, 698-704.

ATHEY, T. W., STUCHLY, M. A. & STUCHLY, S. S. 1982. MEASUREMENT OF RADIO-FREQUENCY PERMITTIVITY OF BIOLOGICAL TISSUES WITH AN OPEN-ENDED COAXIAL LINE .1. *Ieee Transactions on Microwave Theory and Techniques,* 30, 82-86.

AU, L., ZHANG, Q., COBLEY, C. M., GIDDING, M., SCHWARTZ, A. G., CHEN, J. & XIA, Y. 2009. Quantifying the cellular uptake of antibody-conjugated Au nanocages by two-photon microscopy and inductively coupled plasma mass spectrometry. *ACS nano,* 4, 35-42.

BALASUBRAMANIAN, S. K., YANG, L., YUNG, L.-Y. L., ONG, C.-N., ONG, W.-Y. & YU, L. E. 2010. Characterization, purification, and stability of GNPs. *Biomaterials,* 31, 9023-9030.

BALOGH L, NIGAVEKAR S. S., NAIR B. M., LESNIAK W., ZHANG C., SUNG L. Y., KARIAPPER M. S., EL-JAWAHRI A., LLANES M., BOLTON B., MAMOU F., TAN W., HUTSON A., MINC L., KHAN M. K. 2007. Significant effect of size on the in vivo biodistribution of gold composite nanodevices in mouse tumor models. *Nanomedicine*, 3(4), 281-96.

BAPTISTA, P., PEREIRA, E., EATON, P., DORIA, G., MIRANDA, A., GOMES, I., QUARESMA, P. & FRANCO, R. 2008. GNPs for the development of clinical diagnosis methods. *Analytical and Bioanalytical Chemistry,* 391, 943-950.

BEDARD, M. F., DE GEEST, B. G., SKIRTACH, A. G., MOEHWALD, H. & SUKHORUKOV, G. B. 2010. Polymeric microcapsules with light responsive properties for encapsulation and release. *Advances in Colloid and Interface Science,* 158, 2-14.

BRUST, M., FINK, J., BETHELL, D., SCHIFFRIN, D. & KIELY, C. 1995. Synthesis and reactions of functionalised GNPs. *J. Chem. Soc., Chem. Commun.*, 1655-1656.

BUONGIORNO, J., VENERUS, D. C., PRABHAT, N., MCKRELL, T., TOWNSEND, J., CHRISTIANSON, R., TOLMACHEV, Y. V., KEBLINSKI, P., HU, L.-W. & ALVARADO, J. L. 2009. A benchmark study on the thermal conductivity of nanofluids. *Journal of Applied Physics,* 106, 094312-094312-14.

BÉDARD, M. F., DE GEEST, B. G., SKIRTACH, A. G., MÖHWALD, H. & SUKHORUKOV, G. B. 2010. Polymeric microcapsules with light responsive properties for encapsulation and release. *Advances in colloid and interface science,* 158, 2-14.

CARDINAL, J., KLUNE, J. R., CHORY, E., JEYABALAN, G., KANZIUS, J. S., NALESNIK, M. & GELLER, D. A. 2008. Noninvasive radiofrequency ablation of cancer targeted by GNPs. *Surgery,* 144, 125-132.

CARUSO, R. A., ASHOKKUMAR, M. & GRIESER, F. 2002. Sonochemical formation of gold sols. *Langmuir,* 18, 7831-7836.

CHEN, H., SHAO, L., MING, T., SUN, Z., ZHAO, C., YANG, B. & WANG, J. 2010. Understanding the photothermal conversion efficiency of gold nanocrystals. *Small,* 6, 2272-2280.

CHEN, H.-J.,& WEN D., 2011. Nanoparticle-mediated ultrasonic heating for biomedical applications, *Thermal and Materials Nanoscience and Nanotechnology*

CHEN, H.-J. & WEN, D. 2011. Ultrasonic-aided fabrication of gold nanofluids. *Nanoscale Research Letters,* 6, 198.

CHEN, H.-J. & WEN, D. 2013. Experimental study of electromagnetic heating of gold nanopartide dispersions at 200 kHz. *Nanomedicine,* 8, 215-222.

CHEN, J., WANG, D., XI, J., AU, L., SIEKKINEN, A., WARSEN, A., LI, Z.-Y., ZHANG, H., XIA, Y. & LI, X. 2007. Immuno gold nanocages with tailored optical properties for targeted photothermal destruction of cancer cells. *Nano Letters,* 7, 1318-1322.

CHEN, J. Y., WILEY, B., LI, Z. Y., CAMPBELL, D., SAEKI, F., CANG, H., AU, L., LEE, J., LI, X. D. & XIA, Y. N. 2005. Gold nanocages: Engineering their structure for biomedical applications. *Advanced Materials,* 17, 2255-2261.

CLINICALTRIALS, gov. 2010. Pilot study of AuroLase(tm) therapy in refractory and/or recurrent tumors of the head and neck. (cited 2013,March19), Available from: http://clinicaltrials.gov/ct2/show/NCT00848042.

COBLEY, C. M., AU, L., CHEN, J. & XIA, Y. 2010. Targeting gold nanocages to cancer cells for photothermal destruction and drug delivery. *Expert opinion on drug delivery,* 7, 577-587.

CONNOR, E. E., MWAMUKA, J., GOLE, A., MURPHY, C. J. & WYATT, M. D. 2005. GNPs are taken up by human cells but do not cause acute cytotoxicity. *Small,* 1, 325-327.

COOK, J. R., KIM S., PEARCE J. A. & EMELIANOV, S. Y. 2010. Targeted microwave hyperthermia monitored with ultrasound thermography. *2010 IEEE International Ultrasonics Symposium Proceedings*, 2262-2265,

CORR, S. J., RAOOF, M., MACKEYEV, Y., PHOUNSAVATH, S., CHENEY, M. A., CISNEROS, B. T., SHUR, M., GOZIN, M., MCNALLY, P. J. & WILSON, L. J. 2012. Citrate-Capped Gold Nanoparticle Electrophoretic Heat Production in Response to a Time-Varying Radio-Frequency Electric Field. *The Journal of Physical Chemistry C,* 116, 24380-24389.

DANIEL, M.-C. & ASTRUC, D. 2004. GNPs: assembly, supramolecular chemistry, quantum-size-related properties, and applications toward biology, catalysis, and nanotechnology. *Chemical Reviews-Columbus,* 104, 293.

DEJUGNAT, C., KOEHLER, K., DUBOIS, M., SUKHORUKOV, G. B., MOEHWALD, H., ZEMB, T. & GUTTMANN, P. 2007. Membrane densification of heated polyelectrolyte multilayer capsules characterized by soft X-ray microscopy. *Advanced Materials,* 19, 1331-+.

DEL MERCATO, L. L., GONZALEZ, E., ABBASI, A. Z., PARAK, W. J. & PUNTES, V. 2011. Synthesis and evaluation of gold nanoparticle-modified polyelectrolyte capsules under microwave irradiation for remotely controlled release for cargo. *Journal of Materials Chemistry,* 21, 11468-11471.

DICKERSON, E. B., DREADEN, E. C., HUANG, X., EL-SAYED, I. H., CHU, H., PUSHPANKETH, S., MCDONALD, J. F. & EL-SAYED, M. A. 2008. Gold

nanorod assisted near-infrared plasmonic photothermal therapy (PPTT) of squamous cell carcinoma in mice. *Cancer Letters,* 269, 57-66.

EL-SAYED, I. H., HUANG, X. & EL-SAYED, M. A. 2006. Selective laser photo-thermal therapy of epithelial carcinoma using anti-EGFR antibody conjugated GNPs. *Cancer Letters,* 239, 129-135.

EMERICH, D. F. & THANOS, C. G. 2006. The pinpoint promise of nanoparticle-based drug delivery and molecular diagnosis. *Biomolecular engineering,* 23, 171-184.

ENSMINGER, D. & STULEN, F. B. 2010. *Ultrasonics: Data, Equations and Their Practical Uses*, CRC Press.

FARNY, C. H., WU, T., HOLT, R. G., MURRAY, T. W. & ROY, R. A. 2005. Nucleating cavitation from laser-illuminated nano-particles. *Acoustics Research Letters Online,* 6, 138.

FERNANDEZ CABADA, T., SANCHEZ LOPEZ DE PABLO, C., MARTINEZ SERRANO, A., DEL POZO GUERRERO, F., SERRANO OLMEDO, J. J. & RAMOS GOMEZ, M. 2012. Induction of cell death in a glioblastoma line by hyperthermic therapy based on gold nanorods. *International Journal of Nanomedicine,* 7, 1511-1523.

FRENS, G. 1973. Controlled nucleation for the regulation of the particle size in monodisperse gold suspensions. *Nature,* 241, 20-22.

GABRIEL, S., LAU, R. W. & GABRIEL, C. 1996. The dielectric properties of biological tissues .3. Parametric models for the dielectric spectrum of tissues. *Physics in Medicine and Biology,* 41, 2271-2293.

GANGULY, S., SIKDAR, S. & BASU, S. 2009. Experimental investigation of the effective electrical conductivity of aluminum oxide nanofluids. *Powder Technology,* 196, 326-330.

GANNON C. J., CHERUKURI P., YAKOBSON B. I., COGNET L., KANZIUS J. S., KITTRELL C., WEISMAN R. B., PASQUALI M., SCHMIDT H. K., SMALLEY R. E., Curley S. A. 2007. Carbon Nanotube-enhanced Thermal Destruction of Cancer Cells in a Noninvasive Radiofrequency Field. *CANCER*, 110, 12

GANNON, C. J., PATRA, C. R., BHATTACHARYA, R., MUKHERJEE, P. & CURLEY, S. A. 2008. Intracellular GNPs enhance non-invasive radiofrequency thermal destruction of human gastrointestinal cancer cells. *J Nanobiotechnol,* 6.

GHAHREMANI, F. H., SAZGARNIA, A., BAHREYNI-TOOSI, M. H., RAJABI, O. & ALEDAVOOD, A. 2011. Efficacy of microwave hyperthermia and chemotherapy in the presence of GNPs: An in vitro study on osteosarcoma. *International Journal of Hyperthermia,* 27, 625-636.

GHOSH, R., PRADHAN, L., DEVI, Y. P., MEENA, S., TEWARI, R., KUMAR, A., SHARMA, S., GAJBHIYE, N., VATSA, R. & PANDEY, B. N. 2011. Induction heating studies of Fe3O4 magnetic nanoparticles capped with oleic acid and polyethylene glycol for hyperthermia. *Journal of Materials Chemistry,* 21, 13388-13398.

GHOSH, S. K. & PAL, T. 2007. Interparticle coupling effect on the surface plasmon resonance of GNPs: From theory to applications. *Chemical Reviews,* 107, 4797-4862.

GLAZER, E. S., ZHU, C., MASSEY, K. L., THOMPSON, C. S., KALUARACHCHI, W. D., HAMIR, A. N. & CURLEY, S. A. 2010. Noninvasive Radiofrequency Field Destruction of Pancreatic Adenocarcinoma Xenografts Treated with Targeted GNPs. *Clinical Cancer Research,* 16, 5712-5721.

GLAZER E. S., CURLEY S. A. 2011. Non-invasive radiofrequency ablation of malignancies mediated by quantum dots, gold nanoparticles and carbon nanotubes. *Ther Deliv,* 2(10),1325-30.

GLAZER E. S., ZHU C., HAMIR A. N., BORNE A., THOMPSON C. S., CURLEY S. A. 2011. Biodistribution and acute toxicity of naked gold nanoparticles in a rabbit hepatic tumor model. *Nanotoxicology*, 5(4):459-68.

GOBIN, A. M., LEE, M. H., HALAS, N. J., JAMES, W. D., DREZEK, R. A. & WEST, J. L. 2007. Near-infrared resonant nanoshells for combined optical imaging and photothermal cancer therapy. *Nano Letters,* 7, 1929-1934.

GUO, C., WANG, J. & DAI, Z. 2011. Selective content release from light-responsive microcapsules by tuning the surface plasmon resonance of gold nanorods. *Microchimica Acta,* 173, 375-382.

HABERZETTL, C. 2002. Nanomedicine: destination or journey? *Nanotechnology,* 13, R9.

HAMILTON R. L. &CROSSER O. K. 1962, Thermal conductivity of heterogeneous two- component systems. *I&EC Fundam*, 1, 187-191.

HAINFELD, J. F., SLATKIN, D. N. & SMILOWITZ, H. M. 2005. The use of GNPs to enhance radiotherapy in mice. *Proceedings of the American Association for Cancer Research Annual Meeting,* 46, 287-287.

HERGT R, DUTZ S, RO¨DER M. 2008. Effects of size distribution on hysteresis losses of magnetic nanoparticles for hyperthermia. *Journal of Physics: Condensed Matter* 20: 385214.

HIRSCH, L. R., STAFFORD, R. J., BANKSON, J. A., SERSHEN, S. R., RIVERA, B., PRICE, R. E., HAZLE, J. D., HALAS, N. J. & WEST, J. L. 2003. Nanoshell-

mediated near-infrared thermal therapy of tumors under magnetic resonance guidance. *Proceedings of the National Academy of Sciences of the United States of America,* 100, 13549-13554.

HO, V. H., SMITH, M. J. & SLATER, N. K. 2011. Effect of magnetite nanoparticle agglomerates on the destruction of tumor spheroids using high intensity focused ultrasound. *Ultrasound in medicine & biology,* 37, 169-175.

HU, S.-H., TSAI, C.-H., LIAO, C.-F., LIU, D.-M. & CHEN, S.-Y. 2008. Controlled rupture of magnetic polyelectrolyte microcapsules for drug delivery. *Langmuir,* 24, 11811-11818.

HU Y., MENG L., NIU L., LU Q. 2013. Highly Cross-Linked and Biocompatible Polyphosphazene-Coated. *Langmuir*, 29, 9156−9163

HUANG, L., GUO, Z. R., WANG, M. & GU, N. 2006a. Facile synthesis of gold nanoplates by citrate reduction of AuCl~ 4^-at room temperature. *Chinese Chemical Letters,* 17, 1405.

HUANG, M., QIAO, Z., MIAO, F., JIA, N. & SHEN, H. 2009. Biofunctional magnetic nanoparticles as contrast agents for magnetic resonance imaging of pancreas cancer. *Microchimica Acta,* 167, 27-34.

HUANG, X., EL-SAYED, I. H., QIAN, W. & EL-SAYED, M. A. 2006b. Cancer cell imaging and photothermal therapy in the near-infrared region by using gold nanorods. *Journal of the American Chemical Society,* 128, 2115-2120.

JUN, Y. W., HUH, Y. M., CHOI, J. S., LEE, J. H., SONG, H. T., KIM, S., YOON, S., KIM, K. S., SHIN, J. S., SUH, J. S. & CHEON, J. 2005. Nanoscale size effect of magnetic nanocrystals and their utilization for cancer diagnosis via magnetic resonance imaging. *Journal of the American Chemical Society,* 127, 5732-5733.

JACKSON, J. D. 1975. Classical Electrodynamics, John Wiley & Sons, Inc.,New York.

KERKER, M. 1969. The scattering of light, and other electromagnetic radiation.

KHANDHAR A. P., FERGUSON R. M., SIMON J. A., KRISHNAN K. M. 2012. Tailored magnetic nanoparticles for optimizing magnetic fluid hyperthermia. J Biomed Mater Res Part A 100A:728–737.

KIM, B. H., &PETERSON G. P. 2007. Effect of morphology of carbon nanotubes on thermal conductivity enhancement of nanofluids. *J Thermophys Heat Transf*, 21,451-459.

KIMLING, J., MAIER, M., OKENVE, B., KOTAIDIS, V., BALLOT, H. & PLECH, A. 2006. Turkevich method for gold nanoparticle synthesis revisited. *The Journal of Physical Chemistry B,* 110, 15700-15707.

KOEHLER, K., MOEHWALD, H. & SUKHORUKOV, G. B. 2006. Thermal behavior of polyelectrolyte multilayer microcapsules: 2. Insight into molecular mechanisms for the PDADMAC/PSS system. *Journal of Physical Chemistry B,* 110, 24002-24010.

KOEHNE, J. E., CHEN, H., CASSELL, A. M., YE, Q., HAN, J., MEYYAPPAN, M. & LI, J. 2004. Miniaturized multiplex label-free electronic chip for rapid nucleic acid analysis based on carbon nanotube nanoelectrode arrays. *Clinical chemistry,* 50, 1886-1893.

KRUSE, D. E., STEPHENS, D. N., LINDFORS, H. A., INGHAM, E. S., PAOLI, E. E. & FERRARA, K. W. 2011. A radio-frequency coupling network for heating of citrate-coated GNPs for cancer therapy: design and analysis. *Biomedical Engineering, IEEE Transactions on,* 58, 2002-2012.

LEE, Y.-H., KIM, G., JOE, M., JANG, J.-H., KIM, J., LEE, K.-R. & KWON, Y.-U. 2010. Enhancement of electrocatalytic activity of GNPs by sonochemical treatment. *Chem. Commun.,* 46, 5656-5658.

LI, C., CAI, W., LI, Y., HU, J. & LIU, P. 2006a. Ultrasonically induced Au nanoprisms and their size manipulation based on aging. *The Journal of Physical Chemistry B,* 110, 1546-1552.

LI, C. C., CAI, W. P., LI, Y., HU, J. L. & LIU, P. S. 2006b. Ultrasonically induced Au nanoprisms and their size manipulation based on aging. *Journal of Physical Chemistry B,* 110, 1546-1552.

LI, D., JUNG, Y. S., TAN, S., KIM, H. K., CHORY, E. & GELLER, D. A. 2011. Negligible absorption of radiofrequency radiation by colloidal GNPs. *Journal of colloid and interface science,* 358, 47-53.

LIN, C.-Y., HUANG, Y.-L., LI, J.-R., CHANG, F.-H. & LIN, W.-L. 2010. Effects of focused ultrasound and microbubbles on the vascular permeability of nanoparticles delivered into mouse tumors. *Ultrasound in medicine & biology,* 36, 1460-1469.

LOO, C., LIN, A., HIRSCH, L., LEE, M. H., BARTON, J., HALAS, N. J., WEST, J. & DREZEK, R. 2004. Nanoshell-enabled photonics-based imaging and therapy of cancer. *Technology in Cancer Research & Treatment,* 3, 33-40.

MANTHE, R. L., FOY, S. P., KRISHNAMURTHY, N., SHARMA, B. & LABHASETWAR, V. 2010. Tumor ablation and nanotechnology. *Molecular pharmaceutics,* 7, 1880-1898.

MASHAL, A., SITHARAMAN, B., LI, X., AVTI, P. K., SAHAKIAN, A. V., BOOSKE, J. H. & HAGNESS, S. C. 2010. Toward carbon-nanotube-based theranostic agents for microwave detection and treatment of breast cancer: Enhanced dielectric and heating response of tissue-mimicking materials. *Biomedical Engineering, IEEE Transactions on,* 57, 1831-1834.

MAYNE, A., BAYLISS, S., BARR, P., TOBIN, M. & BUCKBERRY, L. 2000. Biologically interfaced porous silicon devices. *physica status solidi (a),* 182, 505-513.

MORAN, C. H., WAINERDI, S. M., CHERUKURI, T. K., KITTRELL, C., WILEY, B. J., NICHOLAS, N. W., CURLEY, S. A., KANZIUS, J. S. & CHERUKURI, P. 2009. Size-Dependent Joule Heating of GNPs Using Capacitively Coupled Radiofrequency Fields. *Nano Research,* 2, 400-405.

MOTOYAMA, J., HAKATA, T., KATO, R., YAMASHITA, N., MORINO, T., KOBAYASHI, T. & HONDA, H. 2010. Size Dependent Heat Generation of Magnetic Nanoparticles Under AC Magnetic Field for Cancer Therapy. *Animal Cell Technology: Basic & Applied Aspects.* Springer.

NAM, J., WON, N., JIN, H., CHUNG, H. & KIM, S. 2009. pH-Induced Aggregation of GNPs for Photothermal Cancer Therapy. *Journal of the American Chemical Society,* 131, 13639-13645.

NARDUCCI, D. 2007. An Introduction to Nanotechnologies: What's in it for Us? *Veterinary research communications,* 31, 131-137.

NAVEENRAJ, S., ANANDAN, S., KATHIRAVAN, A., RENGANATHAN, R. & ASHOKKUMAR, M. 2010. The interaction of sonochemically synthesized GNPs with serum albumins. *Journal of pharmaceutical and biomedical analysis,* 53, 804-810.

OGI, T., SAITOH, N., NOMURA, T. & KONISHI, Y. 2010. Room-temperature synthesis of GNPs and nanoplates using Shewanella algae cell extract. *Journal of Nanoparticle Research,* 12, 2531-2539.

OKITSU, K., ASHOKKUMAR, M. & GRIESER, F. 2005. Sonochemical synthesis of GNPs: Effects of ultrasound frequency. *Journal of Physical Chemistry B,* 109, 20673-20675.

ORENDORFF, C. J., SAU, T. K. & MURPHY, C. J. 2006. Shape-dependent plasmon-resonant GNPs. *Small,* 2, 636-639.

PATRA, H. K., BANERJEE, S., CHAUDHURI, U., LAHIRI, P. & DASGUPTA, A. K. 2007. Cell selective response to GNPs. *Nanomedicine: Nanotechnology, Biology and Medicine,* 3, 111-119.

PATUNGWASA, W. & HODAK, J. H. 2008. pH tunable morphology of the GNPs produced by citrate reduction. *Materials Chemistry and Physics,* 108, 45-54.

PAVLOV, A. M., SAEZ, V., COBLEY, A., GRAVES, J., SUKHORUKOV, G. B. & MASON, T. J. 2011a. Controlled protein release from microcapsules with composite shells using high frequency ultrasound—potential for in vivo medical use. *Soft Matter,* 7, 4341-4347.

PAVLOV, A. M., SAPELKIN, A. V., HUANG, X., P'NG, K. M., BUSHBY, A. J., SUKHORUKOV, G. B. & SKIRTACH, A. G. 2011b. Neuron cells uptake of polymeric microcapsules and subsequent intracellular release. *Macromolecular bioscience,* 11, 848-854.

PELAZ, B., GRAZU, V., IBARRA, A., MAGEN, C., DEL PINO, P. & DE LA FUENTE, J. M. 2012. Tailoring the Synthesis and Heating Ability of Gold Nanoprisms for Bioapplications. *Langmuir,* 28, 8965-8970.

PERNODET, N., FANG, X., SUN, Y., BAKHTINA, A., RAMAKRISHNAN, A., SOKOLOV, J., ULMAN, A. & RAFAILOVICH, M. 2006. Adverse effects of citrate/GNPs on human dermal fibroblasts. *Small,* 2, 766-773.

PUSTOVALOV, V. K., SMETANNIKOV, A. S. & ZHAROV, V. P. 2008. Photothermal and accompanied phenomena of selective nanophotothermolysis with GNPs and laser pulses. *Laser Physics Letters,* 5, 775-792.

RADZIUK, D., GRIGORIEV, D., ZHANG, W., SU, D., MÖHWALD, H. & SHCHUKIN, D. 2010. Ultrasound-assisted fusion of preformed GNPs. *The Journal of Physical Chemistry C,* 114, 1835-1843.

RANG, M., JONES, A. C., ZHOU, F., LI, Z.-Y., WILEY, B. J., XIA, Y. & RASCHKE, M. B. 2008. Optical Near-Field Mapping of Plasmonic Nanoprisms. *Nano Letters,* 8, 3357-3363.

RAOOF, M., CORR, S. J., KALUARACHCHI, W. D., MASSEY, K. L., BRIGGS, K., ZHU, C., CHENEY, M. A., WILSON, L. J. & CURLEY, S. A. 2012. Stability of antibody-conjugated GNPs in the endolysosomal nanoenvironment: implications for noninvasive radiofrequency-based cancer therapy. *Nanomedicine: Nanotechnology, Biology and Medicine,* 8, 1096-1105.

RAU, R. 2005. Have traditional DMARDs had their day? *Clinical rheumatology,* 24, 189-202.

ROSENSWEIG R. E. 2002. Heating magnetic fluid with alternating magnetic field. J Magnetism Mag Mats 252: 370–374.

SADAUSKAS E., DANSCHER G., STOLTENBERG M., VOGEL U., LARSEN A., WALLIN H. 2009. Protracted elimination of gold nanoparticles from mouse liver. *Nanomedicine*, 5(2):162-9

SAN, B. H., MOH, S. H. & KIM, K. K. 2013. Investigation of the heating properties of platinum nanoparticles under a radiofrequency current. *International Journal of Hyperthermia*, 1-7.

SASSAROLI, E., LI, K. & O'NEILL, B. 2012. Radio frequency absorption in gold nanoparticle suspensions: a phenomenological study. *Journal of Physics D: Applied Physics,* 45, 075303.

SHAH, N. B., DONG, J. & BISCHOF, J. C. 2010. Cellular uptake and nanoscale localization of GNPs in cancer using label-free confocal Raman microscopy. *Molecular pharmaceutics,* 8, 176-184.

SHENOI, M. M., ANDERSON, J. K. & BISCHOF, J. C. Nanoparticle enhanced thermal therapies. Engineering in Medicine and Biology Society, 2009. EMBC 2009. Annual International Conference of the IEEE, 2009. IEEE, 1979-1982.

SHEPAROVYCH, R., SAHOO, Y., MOTORNOV, M., WANG, S. M., LUO, H., PRASAD, P. N., SOKOLOV, I. & MINKO, S. 2006. Polyelectrolyte stabilized nanowires from Fe3O4 nanoparticles via magnetic field induced self-assembly. *Chemistry of Materials,* 18, 591-593.

SHI, J., VOTRUBA, A. R., FAROKHZAD, O. C. & LANGER, R. 2010. Nanotechnology in drug delivery and tissue engineering: from discovery to applications. *Nano Letters,* 10, 3223-3230.

SINGH, A. K. 2008. Thermal conductivity of nanofluids. *Defence Science Journal,* 58, 600-607.

SKIRTACH, A. G., MUÑOZ JAVIER, A., KREFT, O., KÖHLER, K., PIERA ALBEROLA, A., MÖHWALD, H., PARAK, W. J. & SUKHORUKOV, G. B. 2006. Laser-Induced Release of Encapsulated Materials inside Living Cells. *Angewandte Chemie International Edition,* 45, 4612-4617.

SKRABALAK, S. E., AU, L., LI, X. & XIA, Y. 2007a. Facile synthesis of Ag nanocubes and Au nanocages. *Nature Protocols,* 2, 2182-2190.

SKRABALAK, S. E., CHEN, J., AU, L., LU, X., LI, X. & XIA, Y. 2007b. Gold nanocages for biomedical applications. *Advanced Materials,* 19, 3177-3184.

SMITH, M. J., HO, V. H., DARTON, N. J. & SLATER, N. K. 2009. Effect of magnetite nanoparticle agglomerates on ultrasound induced inertial cavitation. *Ultrasound in medicine & biology,* 35, 1010-1014.

SONG, J. Y., JANG, H.-K. & KIM, B. S. 2009. Biological synthesis of GNPs using< i> Magnolia kobus</i> and< i> Diopyros kaki</i> leaf extracts. *Process Biochemistry,* 44, 1133-1138.

STEED, J. W. & ATWOOD, J. L. 2009. *Supramolecular chemistry*, Wiley.

SU W, WANG H, WANG S, LIAO Z., KANG S., PENG Y., HAN L. 2013. CHANG J., PEG/RGD-modifiedmagneticpolymeric liposomes for controlled drug release and tumor cell targeting. *International journal of pharmaceutics*, 426(1–2):170–181.

SUN, Y. & XIA, Y. 2003. Alloying and dealloying processes involved in the preparation of metal nanoshells through a galvanic replacement reaction. *Nano Letters,* 3, 1569-1572.

SUN, Y. & XIA, Y. 2004. Mechanistic study on the replacement reaction between silver nanostructures and chloroauric acid in aqueous medium. *Journal of the American Chemical Society,* 126, 3892-3901.

TONG, L., ZHAO, Y., HUFF, T. B., HANSEN, M. N., WEI, A. & CHENG, J.-X. 2007. Gold nanorods mediate tumor cell death by compromising membrane integrity. *Advanced Materials,* 19, 3136-+.

TSAI, S.-W., CHEN, Y.-Y. & LIAW, J.-W. 2008. Compound cellular imaging of laser scanning confocal microscopy by using GNPs and dyes. *Sensors,* 8, 2306-2316.

TSUJI, M., HASHIMOTO, M., NISHIZAWA, Y., KUBOKAWA, M. & TSUJI, T. 2005. Microwave-Assisted Synthesis of Metallic Nanostructures in Solution. *Chemistry-A European Journal,* 11, 440-452.

TSUJI, M., HASHIMOTO, M., NISHIZAWA, Y. & TSUJI, T. 2003. Preparation of gold nanoplates by a microwave-polyol method. *Chemistry Letters,* 32, 1114-1115.

UBOLDI, C., BONACCHI, D., LORENZI, G., HERMANNS, M. I., POHL, C., BALDI, G., UNGER, R. E. & KIRKPATRICK, C. J. 2009. GNPs induce cytotoxicity in the alveolar type-II cell lines A549 and NCIH441. *Particle and Fibre Toxicology,* 6.

URATA, C., AOYAMA, Y., TONEGAWA, A., YAMAUCHI, Y. & KURODA, K. 2009. Dialysis process for the removal of surfactants to form colloidal mesoporous silica nanoparticles. *Chemical Communications*, 5094-5096.

VAN DE BROEK, B., DEVOOGDT, N., D'HOLLANDER, A., GIJS, H.-L., JANS, K., LAGAE, L., MUYLDERMANS, S., MAES, G. & BORGHS, G. 2011. Specific Cell Targeting with Nanobody Conjugated Branched GNPs for Photothermal Therapy. *Acs Nano,* 5, 4319-4328.

VARGAS-HERNANDEZ, C., MARISCAL, M., ESPARZA, R. & YACAMAN, M. 2010. A synthesis route of GNPs without using a reducing agent. *Applied Physics Letters,* 96, 213115-213115-3.

WANG, B., CHEN, N., WEI, Y., LI, J., SUN, L., WU, J., HUANG, Q., LIU, C., FAN, C. & SONG, H. 2012. Akt signaling-associated metabolic effects of dietary GNPs in Drosophila. *Scientific Reports,* 2.

WANG, J. & WANG, Z. 2007. Rapid synthesis of hexagon-shaped gold nanoplates by microwave assistant method. *Materials Letters,* 61, 4149-4151.

WEISSLEDER, R. 2001. A clearer vision for in vivo imaging. *Nature Biotechnology,* 19, 316-317.

WEN, D., LIN, G., VAFAEI, S. & ZHANG, K. 2009. Review of nanofluids for heat transfer applications. *Particuology,* 7, 141-150.

WYSZECKI G., STILES W. S. 1982. *Color Science: concepts and methods, quantitative data and formulae*. New York: Wiley

XIA, Y., LI, W., COBLEY, C. M., CHEN, J., XIA, X., ZHANG, Q., YANG, M., CHO, E. C. & BROWN, P. K. 2011. Gold Nanocages: From Synthesis to Theranostic Applications. *Accounts of Chemical Research,* 44, 914-924.

YAVUZ, M. S., CHENG, Y., CHEN, J., COBLEY, C. M., ZHANG, Q., RYCENGA, M., XIE, J., KIM, C., SONG, K. H., SCHWARTZ, A. G., WANG, L. V. & XIA, Y. 2009. Gold nanocages covered by smart polymers for controlled release with near-infrared light. *Nature Materials,* 8, 935-939.

YONEZAWA, T. & KUNITAKE, T. 1999. Practical preparation of anionic mercapto ligand-stabilized GNPs and their immobilization. *Colloids and Surfaces a-Physicochemical and Engineering Aspects,* 149, 193-199.

ZHANG, Y., KOHLER, N. & ZHANG, M. Q. 2002. Surface modification of superparamagnetic magnetite nanoparticles and their intracellular uptake. *Biomaterials,* 23, 1553-1561.

ZHU, J., KAN, C., ZHU, X., WAN, J.-G., HAN, M., ZHAO, Y., WANG, B. & WANG, G. 2007. Synthesis of perfect silver nanocubes by a simple polyol process. *Journal of Materials Research,* 22, 1479-1485.

Appendix

Polarization of a metallic particle its field distribution in a uniform electric field

A particle in small size that put in an electric field with its boundary size much littler than the wavelength, can be regarded as a dipole. The amplitude of this dipole can be written as (Kittel et al., 1996)

$$p = 4\pi r_0^3 \varepsilon_0 \vec{E}, \quad \text{A1}$$

where r_0 is the radius of the particle. The polarization contains two parts; one made by water and the other one because of polarized nanoparticles, and can be written as

$$\begin{aligned} \vec{P} &= \varepsilon_0 \left[\left(1 - \frac{4\pi r_0^3}{3d^3} \right) \chi_{water} \right] \vec{E} + 3 \frac{4\pi r_0^3}{3d^3} \varepsilon_0 \vec{E} \\ &= \varepsilon_0 \vec{E} \left[\left(1 - \frac{4\pi r_0^3}{3d^3} \right) \chi_{water} + 3 \frac{4\pi r_0^3}{3d^3} \right], \end{aligned} \quad \text{A2}$$

where d is the distance among two adjacent particles. As $\frac{4\pi r_0^3}{3d^3}$ can be regarded as the volume fraction of GNPs, q, the effective permittivity can be derived as

$$\varepsilon_r = 1 + \left[(1-q)(\varepsilon_{water} - 1) + 3q \right] = \varepsilon_{water} + q(4 - \varepsilon_{water}), \quad \text{A3}$$

where $\varepsilon_r = 1 + \chi = 1 + \frac{\vec{P}}{\varepsilon_0 \vec{E}}$, has been applied.

Based on Drude Model, the finite conductivity of an imperfect metal can be derived as (Jackson J.D., 1975)

$$\sigma(\omega) = \frac{\sigma_0}{1 + j\omega\tau}, \quad \text{A4}$$

where, τ is the relaxation time, and σ_0 is the DC conductivity. The complex permittivity then can be written as

$$\varepsilon_r(\omega) = 1 - \frac{j\sigma_0}{\omega\varepsilon_0(1 + j\omega\tau)}. \quad \text{A5}$$

Inside the nanoparticle, the field strength can be written as

$$\vec{E} = \frac{3}{\varepsilon_r + 2}\vec{E}_0, \text{A6}$$

where, $\vec{E}_0$ is the electrical field in water in our study (Jason 1975) Au owns extremely high value of conductivity at 4.55×10^7 S/m (Kittel C., 1996) and a very small value of relaxation time at 1.73×10^{-14} s (Pustovit et al., 2001), resulting in that the electrical field inside the particle is more than 10 scales of magnitude lesser than the one in the host water.

List of publications

CHEN, H.-J., & WEN D., 2011. Nanoparticle-mediated ultrasonic heating for biomedical applications, *Thermal and Materials Nanoscience and Nanotechnology* ,Turkey

CHEN, H.-J.& WEN, D. 2011. Ultrasonic-aided fabrication of gold nanofluids. *Nanoscale Research Letters,* 6,198

CHEN, H.-J.& WEN, D. 2013. Experimental study of electromagnetic heating of gold nanopartide dispersions at 200 kHz. *Nanomedicine,* 8, 215-222.

LIU, X. **Chen, H.-J.,**CHEN, X., PARINI, C., WEN, D.,2012.Low frequency heating of gold nanoparticle dispersions for non-invasive thermal therapies, *Nanoscale, 4, 3945-3953*

LIU, X. **Chen, H.-J.,** CHEN, X., PARINI, C., WEN, D.,2012.High power calibration and measurement method for bio-electromagnetic study, *Science, Measurement & Technology, IET*, 6:420-426

LIU, X., **CHEN H.-J.,** ALFADHL, Y., CHEN, X., PARINI, C., WEN, D., 2013. Conductivity and Frequency Dependent Specific Absorption Rate, *Journal of Applied Physics*, 113, 074902

LIU, X., **CHEN, H.-J.,** YANG, B., LI, D., CHEN, X., WEN, D., DONNAN, R., PARINI, C. 2011. Experimental characterization of Gold Nanoparticle suspensions at W band using a quasi-optical bench, *Irmmw-Thz 2011 - 36th International Conference On Infrared, Millimeter, and Terahertz Waves*

Liu X, **CHEN, H.-J.,** YANG, B., LI, D., CHEN, X., WEN, D.,2011. Dielectric Property Measurement of Gold Nanoparticle Suspensions in the Millimetre Wave Range Using a Quasi-optical Bench, The 4th UK/China workshop on Millimetre wave and THz technology, 1-3, Sep, 2011, Glasgow, UK.

ZHANG, H., **CHEN, H.-J.,** DU, X., WEN, D., Photothermal conversion characteristics of gold nanoparticle dispersions, Submitted to *Applied Energy*.